

Innovative XUV and X-ray Plasma Spectroscopy to explore Warm Dense Matter

Dissertation

zur Erlangung des akademischen Grades
doctor rerum naturalium (Dr. rer. nat.)



vorgelegt dem
Rat der Physikalisch-Astronomischen Fakultät
der Friedrich-Schiller-Universität Jena

von Dipl.-Phys. **Ulf Zastra**
geboren am 17. September 1980 in Essen, Deutschland

Gutachter

1. Prof. Dr. Eckhart Förster

Institut für Optik und Quantenelektronik
Friedrich-Schiller-Universität Jena

2. Prof. Dr. Georg Pretzler

Institut für Laser- und Plasmaphysik
Heinrich Heine Universität Düsseldorf

3. Prof. Dr. Dr. h.c./RUS Dieter H. H. Hoffmann

Institut für Kernphysik
Technische Universität Darmstadt

Tag der Disputation: 15. April 2010

Frequently used abbreviations

CCD	charge-coupled device
DOS	density of states
EOS	equation of state
EUV	extreme ultra-violet
FEL	free-electron laser
FLASH	Free-electron LASer in Hamburg
FWHM	full width at half maximum
GMD	gas monitor detector
LULI	Laboratoire pour l'Utilisation des Lasers Intenses
NIST	National Institute of Standards and Technology
SASE	self-amplified spontaneous emission
WDM	warm dense matter
XUV	x-ray ultra-violet, or soft x-rays

a_0	normalized vector potential
\vec{B}, B	magnetic field
c	speed of light in vacuum
c_S	speed of sound
d_{hkl}	crystal lattice spacing
e	charge of the electron
\vec{E}	electric field
E	energy
E_F	Fermi energy
fs	a femtosecond, 10^{-15} s
\hbar	Planck's constant
I	laser energy density or intensity, in W/cm^2
j	current or emissivity
k_B	Boltzmann's constant
m	electron rest mass, $511 \text{ keV}/c^2$
n_e, n_i	electron or ion density
T_e	electron temperature

β	relativistic Lorentz factor
η	resistivity or efficiency
Γ	degeneracy parameter
γ	Lorentz factor
λ	wavelength of electromagnetic radiation
ω	angular frequency, or rocking curve width
ω_P	plasma frequency
σ	conductivity or cross-section
Θ_B	Bragg angle between ray and surface
ρ	a general density

Contents

Frequently used abbreviations	i
1 Motivation	1
2 Introduction to Warm Dense Matter	3
2.1 High-energy density physics and fast ignitor scheme	4
2.2 Short-pulse x-ray sources	5
2.3 Astrophysical objects	6
3 Relativistic optical-laser interaction with a solid metal	7
3.1 Introduction	7
3.2 Plasma generation	7
3.2.1 Ionization and electron acceleration	8
3.2.2 Collisionless absorption	9
3.3 Electron transport	12
3.4 Strongly-coupled Plasmas	14
3.4.1 K-shell ionization cross-sections	14
3.4.2 Ti $K\alpha$ doublet and satellite lines	15
3.5 X-ray spectroscopy of solid-density plasmas	17
3.5.1 Diagnostics for solid-density plasma	17
3.5.2 Crystal x-ray diffraction	18
3.5.3 Properties of two-dimensional bent crystals	19
3.5.4 A spectrometer for the Ti- $K\alpha$ doublet	20
3.5.5 Absolutely calibrated film detector	22
3.6 The LULI 100TW laser facility	23
3.6.1 Layout of the laser amplifier system	23
3.6.2 Temporal pulse shape - contrast and preplasma formation	24
3.7 Radial bulk temperature and $K\alpha$ profiles	25
3.7.1 Experimental setup	25
3.7.2 Radial profiles	29
3.7.3 Temperatures and spot sizes	31
3.8 Summary	37

4 Intense soft x-ray matter interaction	39
4.1 Introduction	39
4.1.1 The FLASH-facility	40
4.2 XUV photo-absorption by Aluminum	41
4.2.1 XUV photo-absorption mechanisms	42
4.2.2 Conduction band of aluminum	43
4.2.3 Electron equilibration dynamics	43
4.2.4 Monte-Carlo simulations	44
4.3 Principles of XUV spectrometers	46
4.3.1 Challenges using XUV radiation	46
4.3.2 Focusing transmission-grating spectrograph after Jasny et al.	49
4.3.3 <i>HiTRaX</i> - a focusing reflection-grating spectrometer	52
4.3.4 Comparing different spectrometer designs	58
4.4 Bremsstrahlung and line spectroscopy	60
4.4.1 Experimental setup	60
4.4.2 Data analysis	62
4.5 Mapping the heated conduction band of aluminum	67
4.5.1 Radiative decay from the conduction band	67
4.5.2 Experimental setup	68
4.5.3 Integrated emission yield	68
4.5.4 Shape of the spectra	69
4.5.5 Results - Conduction band temperature	70
4.6 Turning solid aluminum transparent	71
4.6.1 Saturable absorption	71
4.6.2 Depletion of the L-shell	71
4.6.3 Experimental setup	72
4.6.4 Transmission data analysis	74
4.7 Summary	76
5 General Summary and Outlook	79
6 Zusammenfassung	83
Bibliography	85
Ehrenwörtliche Erklärung	95
Acknowledgments	97
Curriculum vitae	99

1 Motivation

ἔτεῃμι δ' ἄτομα καὶ κενόν .

In reality, there is only atoms and emptiness.

– Demokrit (460 - 371 B.C.)

Warm Dense Matter is an exotic state not commonly found in our usual environment; while the density is comparable to that of solid matter, temperatures of several 10,000 °C and enormous pressures are present. Anyhow, the relevance of warm dense matter research arises from its wide occurrence in the universe: it is a subject in planetary science, stellar physics, and fusion research.

In a laboratory on earth, the generation of this **high-energy-density** state can only be realized within an extremely short moment: a huge amount of energy has to be stored in a sample almost instantaneously. Now, the system is still dense, but has both high temperature and pressure. At this stage, information on this **exotic state** has to be inferred, since, within a less than a nanosecond, the energy will be transferred to the ions. They will start to move fast in all directions - the sample vaporizes. This general process is happening in all plasma-production devices where the plasma generation starts from cold condensed matter - e.g. laser-solid interaction, heavy-ion beam driven plasmas, exploding wires, or pinch plasmas.

Until the early 1980s, generation of warm dense matter was commonly achieved by **shock-compression** using nuclear explosions. Needless to say that this was not the type of experiment most physicists dreamed of. But with the implementation of **short-pulse laser** with pulse durations in the order of a hundred femtoseconds, the deposition of energy into a sample became possible in a time shorter than hydrodynamic motion. Due to tight focusing which is necessary to reach highest intensities, the excited volumes are limited a few μm^3 . In the last 30 years, these lasers became well-established technology and reach petawatt peak power.

The physical mechanism of coupling optical light into solid-density matter is highly non-linear and complex. First, the photon energy is not sufficient to ionize the bound electrons. Second, most of the material is not transparent or even reflecting. Third, in order to achieve these high intensities, the laser is focused down to a few micrometers in diameter. Hence, these lasers produce a hot plasma only in a tiny spot at the sample surface. Subsequently, the escaping **fast electrons** collide with the cold solid and heat it to warm dense conditions.

The first part of this thesis deals with the creation of warm dense matter by irradiating thin foils by an intense short-pulse optical laser pulse. Using x-ray spectroscopy, the properties of the plasma at solid density can be studied. We determine the radial plasma temperature and x-ray yield with a spatial resolution comparable to the laser focal size. Further, the influence of the target foil thickness and preplasma formation is investigated. The properties of the laser-generated hot electrons and their interaction with the target are derived.

The technological concept of short-pulse lasers is presently restricted to optical and infrared wavelengths. Scientists have dreamed of a short-pulse laser operating in the XUV or even x-ray regime. Here, the photons directly photo-ionize bound electrons. Further, by choosing a proper wavelength, one could tune the penetration depth, allowing for very homogeneous heating of comparably large volumes.

Since 2005, the soft x-ray laser FLASH in Hamburg (Germany), based on the **free-electron laser** concept, is delivering **intense monochromatic XUV pulses**. Connected to the emerge of this outstanding device, the creation and characterization of plasma in the XUV regime became important. With **FLASH**, for the first time, intensities are reached in the XUV that were only accessible by optical lasers before.

The second part of this thesis deals with the exciting story of plasma creation and characterization at FLASH. Pioneering methods of plasma spectroscopy such as bremsstrahlung fits, ion line-ratios and radiative decay from the conduction band of a metal sample are presented. It further deals with the development of a suitable **XUV spectrometer** and the discovery of **saturable absorption** in the soft x-ray regime at record intensities up to 10^{16} W/cm².

2 Introduction to Warm Dense Matter

The term **Warm Dense Matter** (WDM) describes materials at temperatures of several eV at solid-like densities. Its physics [1] gains increasing interest because of its location in the transition region from cold condensed materials to hot dense plasmas. These states are of paramount importance to model astrophysical objects. They further occur as a transient non-equilibrium state in novel experiments to generate high energy densities in materials, most notably the realization of inertial confinement fusion.

The creation and investigation of WDM under controlled conditions in the laboratory is a difficult task. Using common optical short-pulse lasers, non-linear absorption leads to rapid temporal variations, steep spatial gradients, and a broad spectrum of plasma physical processes, like non-uniform heating [2], transient changes of the dielectric function [3], optical properties [4], conductivity [5], and shock compression [6]. Pioneering techniques such as shock heating [6, 7], x-ray heating [8, 9, 10], ion heating techniques [11, 12], and XUV free electron laser irradiation [13, 14] have been developed in order to improve the plasma heating mechanism.

In WDM the electron temperature is comparable to the Fermi energy. Furthermore, the interparticle Coulomb correlation energy is equal or exceeds the thermal energy. Thus, electrons as well as ions exhibit temporal and spatial correlations which depend strongly on the plasma parameters, temperature and density. Both the theory for ideal plasmas and condensed matter fail in this regime. The plasma is too hot to be considered as condensed matter.

Finally, knowledge on such strongly coupled plasmas also enables the perpetual improvement of key applications including laser-driven sources of X-rays [15], e.g. to serve as backlighters [16, 17] or particle accelerators [18, 19, 20], providing alternative radiation sources for both scientific and medical applications.

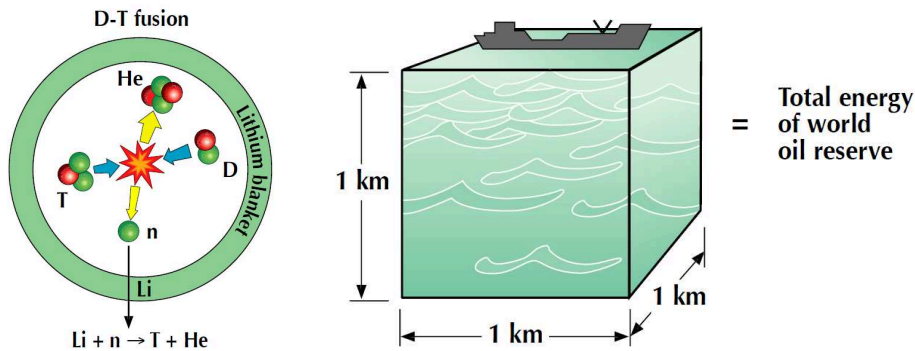


Figure 2.1: Left: Scheme of thermonuclear DT fusion. Right: Fusion energy from all the deuterium in 1 km^3 sea water is equivalent to the world oil reserve [21].

2.1 High-energy density physics and fast ignitor scheme

With the advent of current generation of high-power lasers, a high-energy-density (HED) environment, similar to the core of stars, can be achieved in laboratory. Typically, pressures exceeding 1 Gbar are referred to as HED, and the central process under investigation is thermonuclear fusion [22, 23] in a fuel such as a mixture of deuterium and tritium (DT). A neutron and 17.6 MeV of energy are released as a by-product of each fusion reaction. The thermonuclear fuel with the lowest ignition threshold is a 50-50 mixture of deuterium and tritium. Deuterium can be found in sea water, while tritium can be produced by bombarding lithium with neutrons. There is one atom of deuterium for every 6500 atoms of hydrogen in sea water. Since each $D + T$ reaction produces a neutron, it is possible to breed tritium by surrounding the DT fuel with a lithium blanket where the reaction $Li + n \rightarrow T + He$ takes place. Nuclear fusion from all the deuterium extracted from one cubic kilometer of sea water can generate the same energy as the combustion of the entire world oil reserve, as shown in Fig. 2.1.

High-energy nanosecond-pulse laser systems, the largest being the National Ignition facility (NIF) in Livermore (California) and Laser Mégajoule (LMJ) near Bordeaux (France), are built to demonstrate inertial confinement fusion by compressing a DT fuel capsule to HED conditions as shown in Fig. 2.2. Anyhow, instead of compressing the capsule all the way with the driving lasers down to self-ignition, a concept called *fast ignition* [24] uses an intense short-pulse laser to ignite the pre-compressed fuel. This process is often compared to a gasoline engine, where the fuel is ignited by a spark plug. Diesel engines, on the contrary, compress the fuel up to self-ignition. The spark plug is a beam of laser-accelerated electrons. An advantage is that this process works already

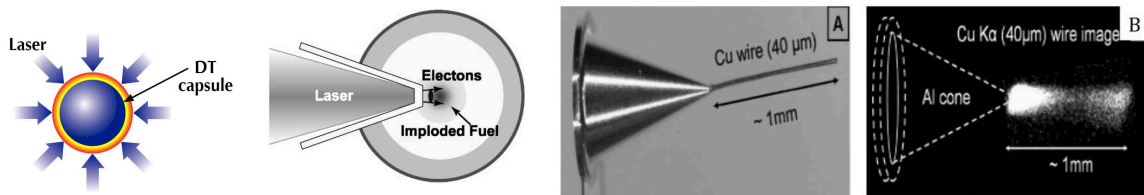


Figure 2.2: Left: Direct-drive laser fusion by compressing a DT capsule. Middle: Cone-guided fast ignitor scheme [26]. Right: (A) Experimental setup and (B) $K\alpha$ imaging of laser-generated electrons coupling from a Al cone into a Cu wire [25].

at lower fuel density, i.e. more mass of the capsule can be ignited, which leads in turn to higher gain of the process.

As will be discussed later in detail, the energy of laser-generated electrons depends both on the laser's intensity I and its wavelength squared, λ^2 . With a proper combination of both, the irradiance $I\lambda^2$ can be chosen in a way that the electrons deposit their energy within few tens of micrometers at the center of the fuel capsule. To generate the electrons as close as possible to the center of compression, a metal cone can be mounted at one side of the fuel capsule as shown in Fig. 2.2. Research in this particular problem is focusing on how the electrons are efficiently generated, how these electrons couple from the cone to an attached structure (as shown in Fig. 2.2 [25]), and, finally, how electrons heat solid-density matter. Chapter 3.7 is particularly dedicated to the latter point.

2.2 Short-pulse x-ray sources

A possible way to create WDM is focusing an optical laser onto a solid sample, generating a relativistic electron beam. This beam then heats a cold solid to typical WDM conditions. The process is accompanied by x-ray line emission from K-shell vacancies created by the electron impact. Hence these plasmas are bright and tiny sources of short x-ray bursts. A highly efficient x-ray plasma source can be operated at moderate laser intensities [15, 27, 28]. E.g., using a few-mJ short-pulse laser at kHz repetition rates and a continuous target design provides a sub-picosecond x-ray source with high repetition rate with table-top scale, suitable for university labs interested in time-resolved x-ray diffraction [29, 30]. Using high-energy lasers of the multi-TW class, one can create much brighter, single-shot x-ray sources. Chapter 3.7 is dedicated to the detailed exploration of the properties of such a plasma. Furthermore, short-pulse x-ray sources are suitable for scattering experiments at solid-density. In order to penetrate high density, one

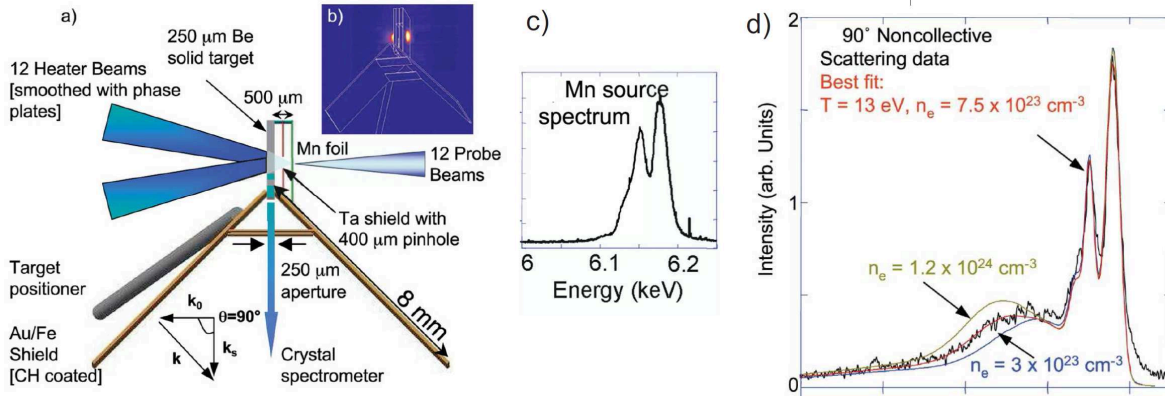


Figure 2.3: Thomson scattering on shock-compressed beryllium: (a) Experimental setup (b) x-ray image (c) spectrum of the Mn backlighter (d) scattering data from 90° [32].

has to use short enough wavelengths. The important plasma parameters, temperature and electron density, are accessible via Thomson scattering [31]: Incoming radiation penetrates the plasma and is scattered off by both the electrons and the ions. From the scattered signal the desired values are derived, as shown in Fig. 2.3 in the case of shock-compressed beryllium [32].

The advent of the first XUV free electron laser FLASH (in Hamburg, Germany - see chapter 4.1.1), accessible for users since 2005, provides bright monochromatic pulses in the XUV with femtosecond duration. Therefore, it is suitable to penetrate much higher densities than it is possible using optical lasers. This source is also used as a probe beam in scattering experiments on hydrogen at astrophysically relevant states [33].

2.3 Astrophysical objects

Obviously, thermonuclear fusion as mentioned in chapter 2.1 is strongly connected with the physics of star interiors. Further interest from the astrophysical point of view is even stronger connected with warm dense matter: it is the main constituent of brown dwarfs [34] and giant planets [35]. The latter are located in our neighborhood (e.g. Jupiter, Saturn), but also in the latest discoveries of extra-solar planets. Since their mass, radius, and density distribution have to be derived from observations, precise knowledge of the equation of state (EOS) of hydrogen, helium and further light elements is essential. Using the free-electron laser FLASH, a novel way of generating warm dense aluminum [13, 14] was demonstrated the first time. These experiments are presented in chapter 4.

3 Relativistic optical-laser interaction with a solid metal

3.1 Introduction

There are few physical and technological advances which can lay claim to such a great number and variety of new research fields as the arrival of the femtosecond (10^{-15} s) laser. This type of laser can be focused to $1000 \times$ greater intensity than it was possible in the mid-1980s. Nowadays fluxes of 10^{18} W/cm² are routinely achieved with *Table-Top Terawatt* lasers, and systems capable of reaching 10^{22} W/cm² with petawatt pulse energy are already under construction in several laboratories around the world. For the description of a particular laser system, refer to chapter 3.6.

With regard to solid-density plasma physics, these lasers are capable to deposit several Joules of energy into a μm^3 volume. This happens within a time well before significant hydrodynamic expansion can take place, since typical plasma expansion velocities are ~ 0.1 nm/fs [36]. Further, electrons and ions can be accelerated in the strong electric fields up to several MeV energies within a few micrometers length.

3.2 Plasma generation

In particular, let us consider a metallic sample, and discuss the phenomena which take place when the laser is focused onto the sample surface.

Free conduction band electrons have characteristic energies up to the Fermi energy E_F , around a few electron volts. The electric field strength in the leading wing of an intense laser pulse is still orders of magnitude higher than the field binding electrons to atoms. That means any target placed at the laser focus undergoes rapid ionization before the peak pulse arrives. All types of non-linear ionization (multi-photon absorption, tunnel and over-the-barrier ionization) take place within the skin depth of the target. The plasma formed in this manner comprises the usual fluid-like mixture of electrons and

ions, but many of its basic properties are essentially controlled by the laser field, rather than by its own density and temperature.

Also, optical energy is transferred to the free electrons which gain kinetic energy. On a femtosecond timescale, mass transport is negligible, but energy transport by fast electrons already plays a role. The electrons have a resonance oscillation at their plasma frequency $\omega_P = 5.64 \times 10^4 \sqrt{n_e [\text{cm}^{-3}]} \text{ s}^{-1}$, depending only on the free-electron density n_e . Note that at relativistic electron velocities the relativistic mass increase leads to a decreasing plasma frequency. The ions do not follow the oscillations of electrons because of inertia. While plasma at lower electron density is transparent for the laser radiation, it will turn into a mirror when $\omega_{\text{laser}} = \omega_P$, which is called the critical electron density $n_c = 1.1 \times 10^{21} \lambda^{-2} [\mu\text{m}] \text{ cm}^{-3}$. At the surface of critical density, the resonance between a p-polarized laser electric fields and plasma frequency may lead to efficient plasma wave generation, called resonance absorption [37].

3.2.1 Ionization and electron acceleration

Let us now derive the process of electron acceleration in intense laser fields.

In the electric field $E(\vec{r}, t)$ of the laser pulse, an electron with charge e experiences a force $F = -eE(\vec{r}, t)$. Its average kinetic energy is therefore given by $\bar{E}_{\text{kin}} \approx U_p(\vec{r})$, the so-called ponderomotive potential:

$$U_p(\vec{r}) = \frac{e^2 |E_0(\vec{r})|^2}{4m\omega^2} \propto I\lambda^2 .$$

Here, m is the electrons rest mass, I is the laser intensity, and λ its wavelength. At moderate intensities of $I \sim 10^{13..14} \text{ W/cm}^2$ and a typical laser wavelength of $\lambda = 1 \mu\text{m}$, U_p has values of about a few eV. Single electrons will be ionized and accelerated. Anyhow, at higher intensities $I > 10^{15} \text{ W/cm}^2$, electrons are accelerated to relativistic velocities v_{os} . Therefore, the laser magnetic force starts to play a role by $\vec{F} = -e\vec{v} \times \vec{B}$. The quantity a_0 is introduced¹, which is the amplitude of the normalized vector potential. It equals unity at an intensity of 10^{18} W/cm^2 and though defines the transition to the relativistic regime. If $a_0 \geq 1$, a fully relativistic description is necessary. The following tables gives an impression of values of a_0 and U_p at $\lambda = 1 \mu\text{m}$:

¹in practical units, $a_0 = 8.53 \times 10^{-10} (I\lambda^2)^{1/2}$, the latter quantity in $\text{W/cm}^2 \mu\text{m}^2$.

Intensity [W/cm ²]	a_0	U_p [MeV]
10^{18}	1	0.16
10^{19}	3	0.96
10^{20}	10	3.87
10^{21}	31	13.2

The relativistically correct electron kinetic energy (and therefore U_p) is $E_{\text{kin}} = E_{\text{total}} - E_{\text{rest}} = (\gamma - 1)E_{\text{rest}}$, where the relativistic factor can be written as

$$\gamma = \left[\frac{I\lambda^2}{1.37 \times 10^{18} \text{ W/cm}^2 \mu\text{m}^2} \right]^{1/2}.$$

3.2.2 Collisionless absorption

In order to distinguish different interaction regimes at the critical density surface, the plasma scale length D is used. It is defined as the gradient of the free electron density n_e in direction of the laser propagation z , at the critical density surface,

$$D = \left. \frac{\partial n_e}{\partial z} \right|_{n_e=n_c}.$$

We compare it to the Debye screening length² λ_D . In case of a rather smooth plasma boundary, $D > \lambda_D$, we have to consider hydrodynamics and the underdense ($n_e < n_c$) portion of the plasma. If the laser is p-polarized, the electric field enters the target and resonance absorption [37] is dominating. Plasma waves are driven by the laser and the plasma is heated by collisions. On the other hand, when the plasma gradient is steep, $D < \lambda_D$, and the laser pulse is short and intense ($a_0 > 1$), it reaches easily the overdense ($n_e > n_c$) plasma.

Now, the so-called collisionless absorption mechanisms [38, 39, 40, 41] come into play:

1. Brunel heating: if the laser is p-polarized, the electric field may accelerate free electrons away from the target. When the laser electric field changes its sign, these electrons are injected into the target material with high kinetic energy. Hence, their mean free path³ is comparatively long. Inside the target, the laser electric field is screened, and the electrons propagate further.

² $\lambda_D = 743 \sqrt{T_e[\text{eV}]/n_e[\text{cm}^{-3}]} \text{ cm}$ is the scale over which mobile electrons screen out electric fields.

For a solid-density target and $T_e \sim 10 \text{ eV}$, $\lambda_D \sim 0.02 \text{ nm}$.

³The mean free path $\text{mfp} = 10^4 Z^{-1} n^{-1} [10^{23} \text{ cm}^{-3}] (I\lambda^2 [10^{18} \text{ W/cm}^2 \mu\text{m}^2])^{2/3}$.

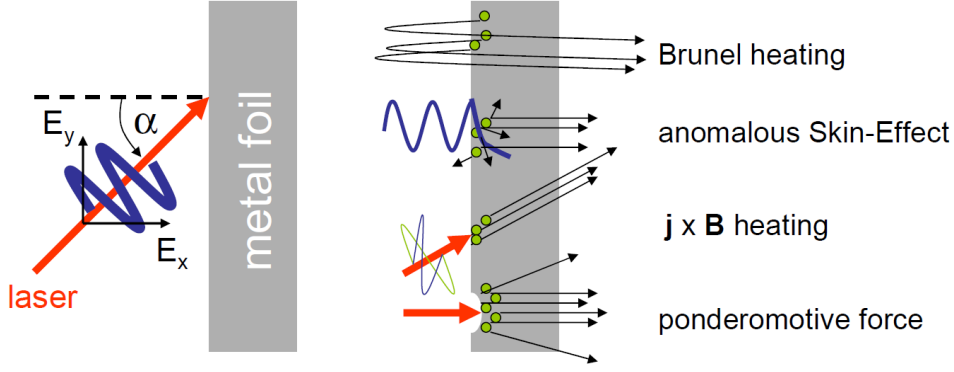


Figure 3.1: Physics of femtosecond laser absorption at intensities $> 10^{18}\text{W}/\text{cm}^2$ and a sharp vacuum-target boundary.

2. Anomalous skin effect: The free electrons within the skin depth $l = c/\omega_p$ get kinetic energy from the penetrating laser electric field. If their mean free path exceeds significantly the skin depth, these electrons will diffuse into the target and deliver their energy to a larger volume.
3. The magnetic term of the Lorentz force ($e\vec{v}\times\vec{B}$) becomes comparable to the electric force ($e\vec{E}$). In this case, the so-called $\vec{j}\times\vec{B}$ heating [42] accelerates bunches of electrons into the target in the direction of the laser pulse at twice the laser frequency [43].
4. The light pressure⁴ strongly exceeds the thermal pressure⁵. In the focal spot, the plasma will therefore be pushed in laser direction. Second, a radial ponderomotive force $F_r \sim -\nabla_r I$ due to the transverse intensity gradient pushes electrons radially away from the center of the beam, creating a charge separation which pulls also the ions out of the focus.

The latter process is also possible to happen in forward direction. In particular, if not only the vacuum intensity distribution of the laser is treated, but also the formation of an intensity gradient e.g. by the critical density. In this case, a steep intensity gradient arises which leads to a strong ponderomotive acceleration.

Many of these effects actually depend upon the laser irradiance $I\lambda^2$, which means that the ‘threshold’ intensity for a given phenomenon can vary depending upon the laser wavelength. Further, it should be mentioned that at relativistic intensities the

⁴ $P_L = 2I/c \simeq 600I[10^{18}\text{W}/\text{cm}^2]$ Mbar [39]

⁵ $P_e = 160N[10^{23}\text{cm}^{-3}]T_e$ Mbar [39]

plasma frequency $\omega_p^{\text{rel}} = \sqrt{(4\pi e^2 n_e)/(m_e \gamma)}$ decreases according to the average γ factor. This modulates the index of reflection and induces relativistic non-linear optics. In an experiment, all these processes contribute to the absorption of laser energy into the plasma.

The question which process is the dominating one depends on the experimental conditions, such as the plasma scale length, the intensity, the laser wavelength, its temporal profile, the initial free electron concentration, and others. Experimental results for the conversion of laser energy E_{laser} into energy carried by the hot electron show a significant scatter around 50 % [44], resembling the diversity of possible absorption mechanisms in the individual experiments.

After a fraction of the laser pulse is absorbed, the electrons have a Maxwell-like temperature distribution. It is most often assumed as one or several Maxwell-Boltzmann distributions with temperature T_{hot} (Eq. 3.1), that is, the number of electrons ΔN in an energy interval ΔE :

$$f(E) = \frac{\Delta N}{\Delta E} \sim \exp \left[-\frac{E}{k_B T_{\text{hot}}} \right].$$

If relativistic corrections are considered to play a role (for electron energies exceeding several MeV), a Maxwell-Jüttner distribution function for a relativistic electron gas can be taken instead:

$$f(\gamma) = \frac{\gamma^2 \beta}{\Theta K_2(1/\Theta)} \exp \left[-\frac{\gamma}{\Theta} \right]$$

where $\Theta = k_B T_{\text{hot}}/mc^2$, and K_2 is the modified Bessel function of the second kind.

As mentioned earlier, at $a_0 > 1$ the temperature of the electron distribution T_{hot} is found to scale with the ponderomotive potential [45, 43, 46]. Several experiments measured the electron energy distribution in laser-solid interaction either directly by means of electron spectrometers or, earlier, indirectly via bremsstrahlung or other methods, a empirical scaling $T_{\text{hot}} \simeq (I\lambda^2)^{1/3}$ was found [47].

Note that the assignment of a single temperature is only valid to describe the falling wing of the electron distribution at energies well above 100 keV. There is no claim that the electrons at lower energies follow the same distribution function. Although the fast MeV electrons leave at the foil backside [48], the electrons with lower energy deposit their energy inside the foil.

Experiments observing the characteristic x-ray emission from layered targets are ap-

plied to study the depth-dependent distribution of the hot electrons. Zamponi et al. [49] use a pair of x-ray pinhole cameras to study the spatial properties of the emission from layered targets and find a diverging electron distribution along the target surface normal.

3.3 Electron transport

While an electron distribution with $T \sim 1$ MeV propagates into a solid metal, a space-charge electric field is set up to which the plasma reacts with a return current almost immediately, i.e., on the timescale of $\omega_p^{-1} \leq 10^{15}$ s [50].

This return current can be estimated to $j_h \approx (0.1 - 0.3)en_c c$, where $n_c \approx 10^{21}\text{cm}^{-3}$ is the critical electron density for reflection of the laser pulse ($\lambda = 1\mu\text{m}$). The current will thermalize after a time $\tau = \nu_{ei}^{-1} \sim (10^{-12} - 10^{-15})$ s, which is defined by the cold electron-ion collision frequency ν_{ei} . It generates a resistive electric field $E = j_h/\sigma$, where σ is the cold plasma conductivity. A typical fast electron at ~ 1 MeV has mean free paths of hundreds of micrometers and a collisional energy loss time of typically a few picoseconds [51] in a solid. Consequently, fast electrons can transport the absorbed energy to parts of the target well away from the laser spot over time scales comparable to the laser pulse length.

The so-called Spitzer [52] resistivity, calculated as the rate of momentum transfer from electrons to ions through collisions,

$$\eta = 1.03 \times 10^{-4} T_e^{-3/2} [\text{eV}] Z \ln \Lambda [\Omega\text{m}]$$

for high temperatures is a decreasing function of the electron temperature T_e . The factor $\ln \Lambda$ is the Coulomb logarithm⁶. E.g., at solid density and above ≈ 10 eV, the electrons are no longer scattered more from the ionic lattice, and only Coulomb collisions take place. The Coulomb cross-section decays with increasing temperature. Therefore, only the cold electrons in the target experience the low-temperature resistivity (which increases with temperature) and couple to the material efficiently, while the hot electrons couple weakly.

Per 1 J laser energy, the average current $I = eN/\Delta t$ carried by N keV electrons over the laser pulse duration Δt amounts to several ten MA [53]. The question whether a net current of this order of magnitude can flow is strongly connected with the arise of self-induced magnetic fields. There are basically two main arguments against it:

⁶Coulomb logarithm $\ln \Lambda = \ln(T_e^{3/2}/\sqrt{\pi}Ze^3n^{1/2})$.

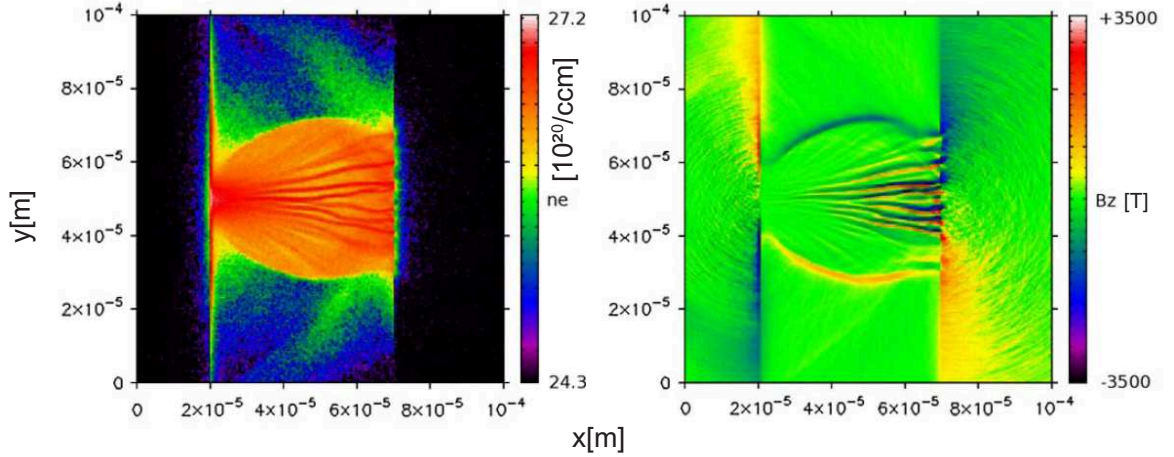


Figure 3.2: Computational results from a hybrid PIC/fluid code are shown [56]. On the left, the free electron density is shown, while the right panel shows the magnetic field. Coming from the left, a laser at 10^{19} W/cm² irradiates a 50 μ m CH foil. 500 fs after irradiation, the electrons form filaments that are slightly refocused by the magnetic field B_Z .

First, assuming a parallel beam of electrons, the self-induced magnetic field force points inwards the beam. If the beam current reaches the Alfvén-limit [54]⁷, $I_A = 17\gamma\beta$ kA, the electrons are bent back and stop⁸. Note that the concept of the Alfvén-limit is derived for a constant current, but in our particular situation we deal with a transient short pulse current.

Anyhow, the second argument for a limited net current is the fact that the energy content of a self-induced magnetic field from a laser-induced electron pulse is about three orders of magnitude larger than the initial laser energy⁹. From these arguments it becomes clear that a return current (or local return currents) must flow. The net current is limited to negligible values.

According to computational models (see Fig. 3.2), the self-induced magnetic fields possibly exceed several 10^2 T [56, 57]. They cause a strong electron beam to break up into filaments and can lead to refocusing inside the target. The return currents on the other hand couple to the material, and an electric field $E = \eta\vec{j}$ is set up. The result is ohmic inhibition of the electron flow. To couple electrons into matter efficiently, one has to ensure that the return current flow free, hence the ohmic inhibition has to be small.

⁷the quantity $\beta\gamma$ is the dimensionless electron momentum, and $\beta\gamma = 2$ at $I = 10^{19}$ W/cm².

⁸ $\beta = v/c$.

⁹described by Bell [55]: assuming a 1 ps, ~ 30 μ m laser pulse at 10^{18} W/cm² and 7 J pulse energy. It induces a magnetic field with $B = 3.2$ GGauss, resulting in a magnetic field energy of 5 kJ.

3.4 Strongly-coupled Plasmas

The highly non-linear electron creation and acceleration process leads to the presence of an electron distribution with energies ranging by several orders of magnitude [58]. Solid targets heated by collisions with these electrons are far from being homogeneous, resulting rather in an essentially non-equilibrium state with steep spatial gradients [59]. The transfer of energy between these “hot” electrons and the target is important for many potential applications, as, for example, isochoric heating of solid targets to high temperatures or the fast ignition [2, 24]. Thus, it is of primary importance to achieve precise knowledge of the physical properties like plasma temperature at solid density with high spatial resolution [2].

The initial plasma state created by relativistic laser-solid interaction is still at solid density, and bulk-electron temperatures are in the order of a few tens of eV, which is comparable to the Fermi energy¹⁰. For metallic titanium, $E_F = 14$ eV. This means that in such a plasma the bulk electrons are still dominantly degenerate, $\Theta = k_B T_e / E_F \sim 1$. Further, the ion coupling parameter¹¹ Γ is greater or equal to unity, i.e., the interparticle Coulomb correlation energy is equal or exceeds the thermal energy. Thus, electrons and ions exhibit strong temporal and spatial correlations.

3.4.1 K-shell ionization cross-sections

The electrons, both from the beam and the return currents, are in principle capable of impact-ionizing the atomic shells when they carry sufficient energy. In particular, the cross-section σ_K for the production of a vacancy in the atomic K shell, which we call simply K-shell ionization cross section, has been investigated by means of both theoretical and experimental methods.

Amongst others, Casnati *et al.* [60] developed an empirical model that allows fitting experimental data with immediate availability of σ_K -values for any combination of electron kinetic energy T and target material. The authors critically analyzed available experimental data. The fitting parameters depend on both the electronic structure of the element and the transition considered. This means that when the transition of a K electron in the continuum is concerned the first-order variable is the K-shell ionization energy I_K for such a transition. Moreover, the overvoltage-dependence is derived from the Bethe asymptotic formula, which shapes the σ_K trend at high U values. The results

¹⁰in practical units, $E_F = 36.4 \text{ eV} \times n_e^{2/3} [10^{24} \text{ cm}^{-3}]$.

¹¹ion coupling parameter $\Gamma = Z^2 / 4\pi\epsilon_0 k_B T_i (4\pi n_i / 3)^{1/3}$. Here Z is the nuclear charge.

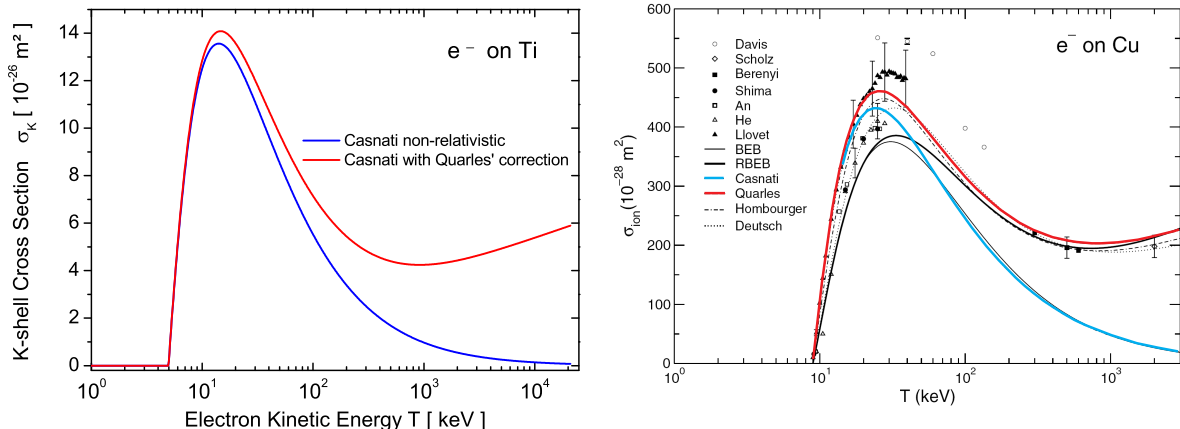


Figure 3.3: Left: K-shell ionization cross section for titanium. Right: Comparison of experimental data (symbols) and several models (lines) for copper. For details, refer to [62]. The non-relativistic model after Casnati *et al.* [60] is indicated by the blue curves, and the relativistic correction [61] was applied by the red curves.

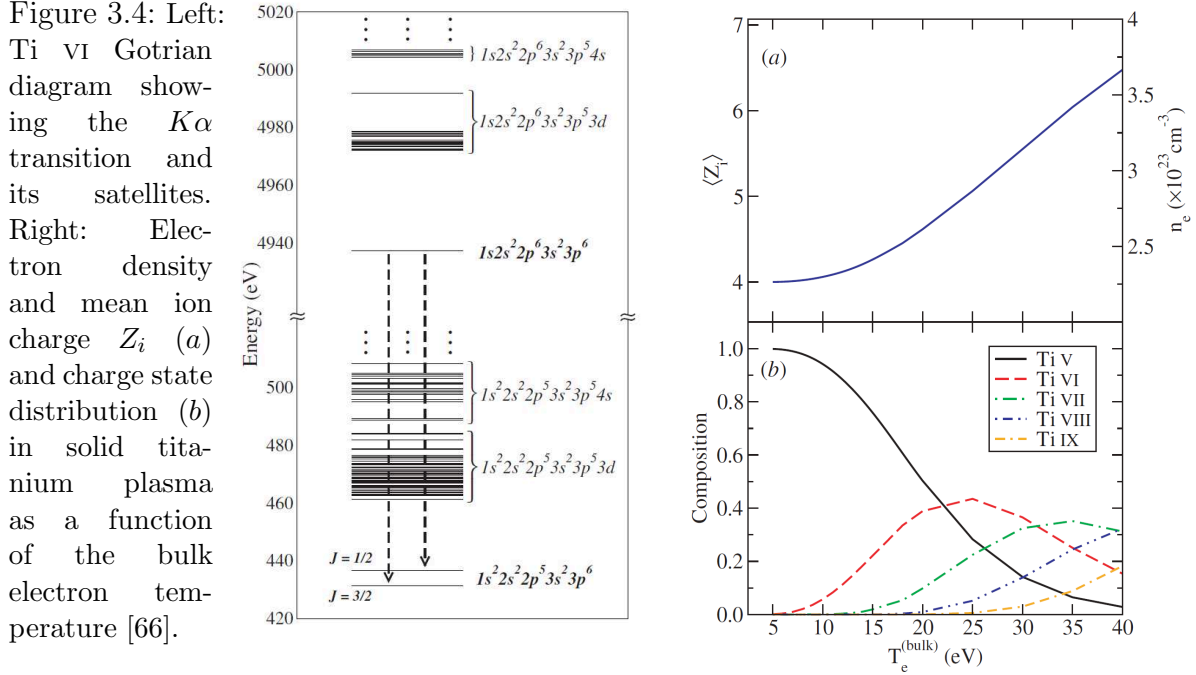
are shown in Fig. 3.3 by blue curves. Obviously the monotonic decrease for relativistic electron energies is in contrast to the experimental data. Therefore, inclusion of non-negligible relativistic effects was taken into account by inserting a first-order correction following Quarles *et al.* [60, 61].

In 2003, Santos *et al.* performed an extensive review of different models and their comparison to available experimental data. The results are shown in Fig. 3.3 in the red curves. It can be seen that the approach by Casnati, together with the relativistic correction factor, is in good agreement with the experimental data within the error bars. For details about the other models as well as the experimental data, refer to their publication [62].

3.4.2 Ti $K\alpha$ doublet and satellite lines

The electron configuration of atomic titanium ($Z=22$) is $[\text{Ar}]3d^24s^2$. In bulk state, delocalized quasi-free electrons have to be taken into account. The four outer electrons (in the 3d and 4s orbitals) form the conduction band. Hence, the lowest charge state is argon-like Ti v with the electron density in the low-temperature limit $n_e \approx 4n_i$. Here $n_i \approx 5.66 \times 10^{22} \text{ cm}^{-3}$ is the ion particle density in solid-state titanium. For details see also Fig. 3.4.

A so-called *non-diagram line* is a line not emitted by a cold solid material, but by an excited state. These lines are often close to strong diagram lines and hence are frequently



called satellites. Their origin, briefly, is recombination, while a vacancy in a higher shell is present. In the particular case of titanium, blue $K\alpha$ satellites show up when a vacancy in the M-shell is present. The line shift amounts to 2–3 eV per vacancy [63, 64] towards higher photon energies. Since the M-shell is the first bound shell in the metallic state, its electrons are ionized thermally as a function of bulk temperature.

In case of L-shell vacancies in titanium, the shift is much larger, about 25 eV per missing electron [65].

Recent progress in line-shape modeling of Ti inner-shell emission lines has been achieved by two different approaches. A thorough, self-consistent modeling requires calculations that should comprise many different processes and effects, such as satellite formation and blend-in, plasma polarization, Stark broadening, solid-density quantum effects, and self-absorption.

In the first approach [67], a perturbative ansatz is chosen to calculate line profiles emitted from WDM. A chemical ab-initio code using a simplified atomic structure with respect to the fine structure components yields unperturbed emission energies and orbitals of various ionization stages. The perturbing plasma potential is calculated within a self-consistent ion sphere model. According to that potential, first order perturbation theory yields shifted line positions and continuum lowering. The line width is treated as a free parameter in this approach. Further, modeling of the complete emission profiles is

based on a self-consistent calculation of the plasma composition under LTE conditions. For this coupled Saha-equations are solved applying a Planck-Larkin renormalization to the partition function.

In the second approach [66], collisional-radiative (CR) calculations treating thousands of atomic transitions from the Flexible Atomic Code (FAC) [68] were performed. The presence of the two electron distributions (the bulk and the hot ones), differing in energies by several orders of magnitude, results in an essentially non-equilibrium state. In practical terms these two very different electron distributions complicate the collisional-radiative calculations significantly, since all atomic processes involving free electrons need to be tabulated over a very wide range of the electron energies. In the calculation, a hot electron ($E = 150$ keV) concentration of 0.1% was assumed.

Spectra of the titanium $K\alpha$ doublet can be modeled using both approaches, that yield approximately the same results. The bulk-electron-temperature is the only free parameter in the modeling of the $K\alpha$ shape, assuming that the fast electrons represent a small fraction of the total electron density [66]. Thus, by varying $T_e^{(bulk)}$, the total electron density, the charge-state distribution, and populations of different levels are calculated self-consistently.

3.5 X-ray spectroscopy of solid-density plasmas

3.5.1 Diagnostics for solid-density plasma

Measurements of the characteristic $K\alpha$ emission have proven to be reliable diagnostics for solid-state-density plasmas [69]. First, the plasma parameters strongly affect the structure of the emitted lines. In particular, the emerge of the blue satellites due to the formation of M-shell holes is an indicator for the bulk-electron temperature [70], as described in chapter 3.4.2. Second, solid-density plasma is transparent to the emitted x-rays, which, therefore, yield unique information on the target interior. This is a large advantage over measurements of XUV or visible radiation. Moreover, the x-ray emission occurs within a few picoseconds, well below the typical hydrodynamic expansion time [27, 71, 72].

Processes such as ionization, Doppler and pressure broadening, opacity and electric fields in the plasma may modify the shape of individual emission lines. Examination of emission line profiles therefore reveal detailed information on plasma conditions. High-resolution x-ray spectroscopy has therefore made significant contributions to the diag-

nostics of solid-density plasmas.

In the case of mid-atomic number elements, K-shell emission spectra occur in the x-ray region and a spectrometer that can resolve wavelengths to mÅ-levels is required.

3.5.2 Crystal x-ray diffraction

The scattering of x-rays of wavelength λ on crystal planes with a spacing d_{hkl} is described by the Bragg reflection condition for lattice indices hkl :

$$\lambda = 2d_{hkl} \times \sin \Theta_B \quad (3.1)$$

with the Bragg reflection angle Θ_B . Differentiation immediately leads to an expression for the local change of the wavelength with the Bragg angle :

$$\frac{\Delta\lambda}{\lambda} = \Delta\Theta_B \times \cot \Theta_B . \quad (3.2)$$

From this equation we note the high dispersion of a setup with large Bragg angle Θ_B .

Let us consider a planar electromagnetic wave incident onto a crystal at the Bragg angle and the reflected x-ray beam recorded by a detector. Initially, the incident and reflected beam shall have the same angle with respect to the lattice planes. Now, if we rock the crystal slightly by the angle ω , the detector will measure the reflected intensity $I(\omega)$, called the rocking curve of the crystal. The FWHM of this curve is called the rocking curve width, which is a function of the Bragg angle, since its gets more narrow at smaller Bragg angles Θ_B . However, values of ~ 50 arcsec at $\Theta_B = 76^\circ$ are typical for the crystals used in our experiments, and yields to $\Delta\lambda/\lambda \approx 6 \times 10^{-5}$ from Eq. 3.2, or a resolving power of 15,000.

The use of one- and two-dimensional curved crystals is common in state-of-the-art x-ray spectrometers [49, 73]. The great advantage of any geometry that uses the Johann-setup [74] is that no slit is needed for high resolutions. This way, the full divergence of the source (i.e., a plasma) can be used to illuminate the spectrometer crystal. This is the key advantage of large-aperture bent crystals. Their much higher luminosity compared to other x-ray optics like total external reflection at grazing incidence or zone plates primarily arises because of their much larger collection solid angle.

Bending the crystal with radius $2R$ (R being the Rowland radius) as proposed by H. H. Johann [74] leads to monochromatic focusing of the source S to the point F . Due to the deviation between the Rowland circle and the crystal surface, a geometrical

aberration, called 'Johann error', is present that grows with crystal extent ξ in dispersion direction:

$$\frac{\Delta\lambda}{\lambda} = \frac{\xi^2}{8 R^2 \tan^2 \Theta_B}$$

On the other hand, the Johann error is negligible at large bending radius R , large Bragg angle Θ_B and reflection close to the crystal center. In particular, in this thesis the practical values are $\xi \leq 10$ mm, $R = 450$ mm and $\Theta_B = 76.6^\circ$, yielding $\Delta\lambda/\lambda \leq 3 \times 10^{-6}$, which is nearly an order of magnitude smaller than the resolution limited by the rocking curve width.

3.5.3 Properties of two-dimensional bent crystals

Additional focusing of the sagittal rays, and therefore one-dimensional imaging of the plasma, can be obtained with two-dimensional bent crystals.

A toroidally bent crystal forms a surface that has both horizontal (meridional) and vertical (sagittal) radii of curvature; the lattice planes are assumed to be parallel to the crystal surface [75]. The use of perfect single crystals from quartz, silicon, germanium, gallium-arsenide, or comparable materials yields to high achievable resolution of several 10^3 due to their narrow rocking curves with widths of some tens of arcseconds. These allow much higher resolution than the use of mosaic HOPG¹² crystals, which, in turn, provide higher luminosity.

The crystal bending radii in the horizontal, R_h , and vertical, R_v , directions determine focal distances in each plane. These foci are given by the following Eq. 3.3.

$$f_h = (R_h \sin \Theta_B) / 2 \quad f_v = R_v / (2 \sin \Theta_B) . \quad (3.3)$$

If $f_h = f_v$ then monochromatic imaging of the source is achieved with a high two-dimensional spatial resolution and a spectral range of a few mÅ [76]. If f_h and f_v differ, the crystal works as a one-dimensional spatially resolving spectrometer [77, 78].

As shown in Fig. 3.5, the plasma source S is positioned at the vertical focal point l_a , so that spatial resolution occurs in the y -direction. The spatial magnification factor, M , is given by the ratio of the crystal-detector distance l_b to plasma-crystal distance l_a . It also connects y to y' on the detectors plane by $y' = -My$. The spectrometer

¹²HOPG - highly orientated pyrolytic graphite.

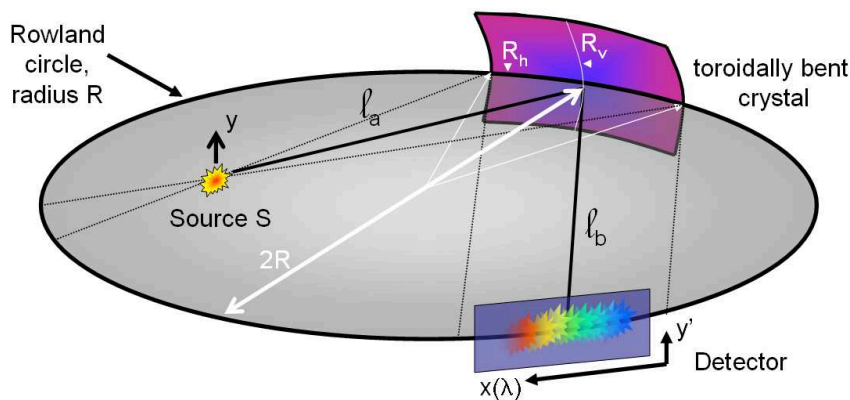


Figure 3.5: Scheme of a toroidally bent crystal spectrometer. The source is located inside the Rowland circle.

geometry in Fig. 3.5 has $M > 1$. This results in the vertical extent of the source being magnified at the detector plane, which lies on the Rowland circle with $l_b = R_h \sin \Theta_B$. Accurate detector alignment is required to avoid the effects of defocussing, maintaining high spatial resolution.

Note that for fixed crystal bending radii, l_a and M vary with wavelength. Over small wavelength ranges these variations are negligible. It is important that the bending radii R_h and R_v of the crystals well as the Bragg angle Θ_B determine the spectrometer geometry as well as its performance.

3.5.4 A spectrometer for the Ti- $K\alpha$ doublet

However, limitations are given by width of the rocking curve, the wavelength of the photons of interest, and of suitable crystals. For this particular work, we investigated K-shell emission of titanium at $\lambda = 2.75 \text{ \AA}$. A GaAs crystal was chosen in (400) reflection with a Bragg angle of $\Theta_B = 76.6^\circ$. The rocking curve should be as small as possible, i.e. the perfection of the crystal as high as possible. The rocking curve of the flat GaAs crystal amounts to 55 arcsec FWHM from a double-crystal setup measurement [77], which agrees with calculations¹³ that yield 53.6 arcsec FWHM. Further, the calculations show that due to the large bending radii of $R_h = 450 \text{ mm}$ and $R_v = 306 \text{ mm}$, the rocking curve FWHM increases less than 2.5 %. Figure 3.6 shows the shape of the calculated rocking curve of the toroidally bent GaAs crystal with a thickness of $80 \text{ }\mu\text{m}$.

Due to its toxicity, the raw crystal was thinned down to $(80 \pm 5) \text{ }\mu\text{m}$ by a company. It was then bonded to a negative (convex) glass former. Bonding means that two clean surfaces attract each other by atomic or molecular forces. The crystal is then glued to a positive glass former. The glue is supplied by the Zeiss company and is highly strainless. The crystal finally is detached from the negative former.

¹³rocking curve calculations were all performed with code Dixi2 by G. Hölzer.

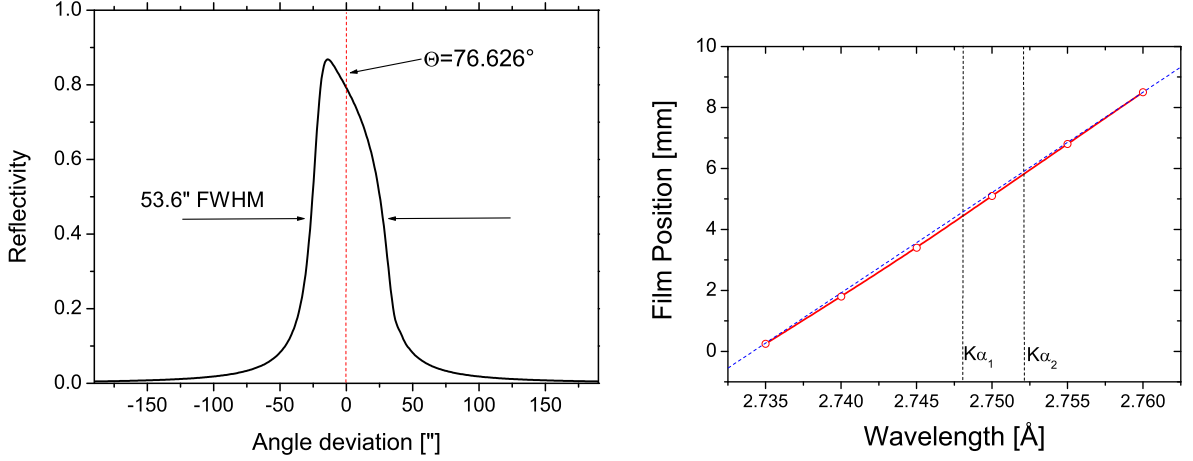


Figure 3.6: Left: Theoretical rocking curve of a toroidally bent GaAs crystal in (400) reflection for unpolarized Ti- $K\alpha$ radiation. Right: Dispersion of the particular spectrometer setup obtained by ray-tracing. The black dotted line is a guide to the eyes to stress the slight non-linearity.

The size of the effective crystal surface is 30 mm in the dispersion plane and $\Delta h = 10$ mm perpendicular to it. The geometry for this particular crystal involves a distance to the plasma of $l_a = 245$ mm and a distance to the detector (located on the Rowland circle) of $l_b = 440$ mm. In conclusion, the magnification in the spatially resolving plane is $M = 1.8$. Zamponi [49] also determined the 1D spatial resolution of the particular crystal used to be $4 \mu\text{m}$ by imaging a gold grid, which is of course only valid at perfect alignment.

The efficiency of the spectrometer setup can be calculated with high accuracy if all input parameters are known [73]:

$$N_{\text{det}} = N_0 \times T \times \frac{R_i \cdot \Delta h}{\sin \Theta_0 \cdot R_h} \times \frac{(2k)^2}{k^2 - 1}.$$

Here, T is the transmission through foils that protect the crystal from debris and the film detector from visible light. Further, $R_i = 267 \mu\text{rad}$ is the integrated reflectivity of the crystal. It can be calculated by integrating the left curve from Fig. 3.6. Then, $k \approx 8$ is the magnification in the dispersion plane. In our case, the ratio of photons on the detector N_{det} , compared to $K\alpha$ photons emitted by the plasma source N_0 , amounts to $N_{\text{det}}/N_0 = 2 \times 10^{-5}$.

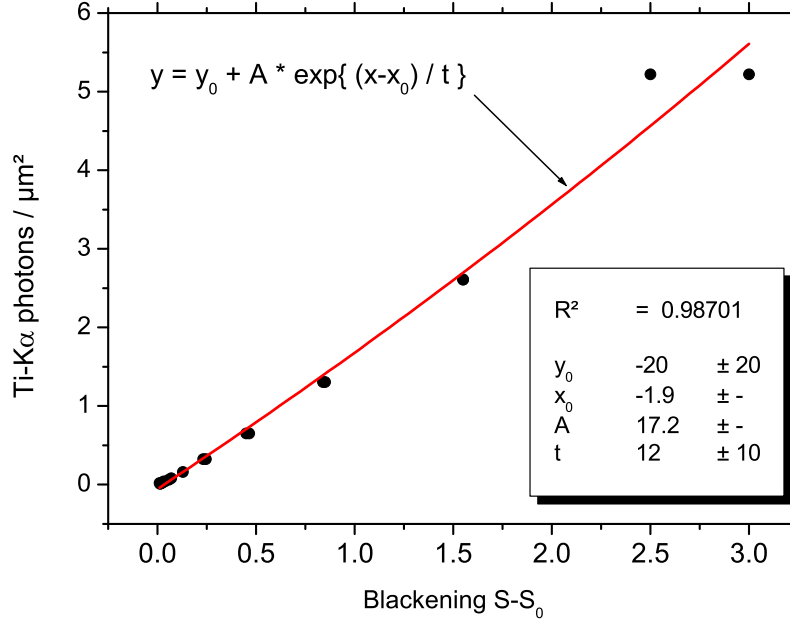


Figure 3.7: The Ti- $K\alpha$ photon area density as a function x-ray film blackening $S - S_0$ for the applied Kodak Industrex HS800 film. The inset shows the fit function presented by the red curve.

3.5.5 Absolutely calibrated film detector

The flat detector is positioned onto the Rowland circle as shown in Fig. 3.5. Ray-tracing calculations¹⁴ were performed yielding an accurate dispersion function, i.e. the dependence of the spatial axis in the dispersion plane on the x-ray wavelength, as shown in Fig. 3.6. Note that this function is slightly non-linear.

We use x-ray film because it is comparatively insensitive to the 'noise' present in typical high-energy density experiment. Electromagnetic shocks affect CCD cameras by inducing pulsed currents in electric circuits and connection cables. Also, fast electrons hit both the detector chip and any shielding (mostly high-Z such as lead) and the chamber walls (steel, aluminum). Here they produce a cascade of secondary hard x-rays.

The main drawback of film is the time needed to extract it from the target chamber and develop it using proper chemicals. Thus, venting of the chamber is necessary. Anyhow, working with glass-laser systems and single-shot targets, as in our case, these points become meaningless.

We used Kodak Industrex HS800 film. It is a fast developing film sensitive to x-rays and visible light with $\lambda < 550$ nm. The base support is $188 \mu\text{m}$ thick, covered by emulsion ($12.5 \mu\text{m}$) plus overcoat ($5 \mu\text{m}$) on both sides. From the same batch, a film was illuminated with titanium $K\alpha$ radiation from an x-ray tube ($E = 4.5$ keV) with logarithmically increasing exposure times. The photon flux from the x-ray tube was absolutely calibrated by comparison to a characterized silicon PIN x-ray diode [79].

¹⁴All ray-tracing in this thesis performed using the CODE T-Ray.

Hence, the blackening S of the film due to titanium $K\alpha$ radiation can be converted into a photon density via the function shown in Fig. 3.7.

3.6 The LULI 100TW laser facility

The experiments reported in this thesis were performed at the *LULI 100TW* laser facility [80, 81, 82] at Ecole Polytechnique, in Palaiseau, France. Operational since 1997, this facility is based on chirped pulse amplification (CPA) [83] and is capable of delivering a pulse with a power equal to 100 TW.

3.6.1 Layout of the laser amplifier system

A scheme is presented in Fig. 3.8. The laser chain starts with a Ti:Sapphire front-end: A Ti:Sa oscillator working at a wavelength of 1057 nm delivers pulses with a few nJ energy and 100 fs duration. Then the laser pulses are stretched to 1.2 ns duration in a grating stretcher before they are further amplified up to 1 mJ pulse energy in a regenerative amplifier at a repetition rate of 10 Hz.

Subsequently, the laser pulses are further amplified by a chain of multi-glass¹⁵ amplifiers doped with Nd³⁺ ions and then enter the experimental hall, containing a vacuum compressor and the vacuum experimental chamber. In between the amplification stages, the beam diameter is increased by telescopes. The last amplification chain consists of four stages, both rod and disc amplifiers, with increasing diameters of 16, 25, 45 (rods) and finally 108 mm (discs). The laser media are flashlamp-pumped several hundreds of nanosecond before the main pulse arrives. A total energy of 100 J (in 500 ps and 6 nm spectral width) can be achieved at the end of this chain. The pulse energy is measured with two independent monitors before it enters the compressor. Further, a fast Pockels cell with a rise time of about half a nanosecond shortens the ASE and prepulses to a minimum.

Since the laser amplifier glass is flashlamp-pumped, it contains thermal load after each irradiation. The optical properties change, and a subsequent shot would suffer from wave-front distortion and thermal lensing. The spatial beam profile is measured by wavefront sensors and optimized using an adaptive mirror between the two passes in the last disc amplifier. This allows a final repetition of one shot in 20 min with almost

¹⁵The use of alternating silicate and phosphate glass enables to widen the amplified spectrum, allowing the pulse to be compressed to short durations below 500 fs. Laser systems with only one type of glass are limited to pulse duration > 0.5 ps.

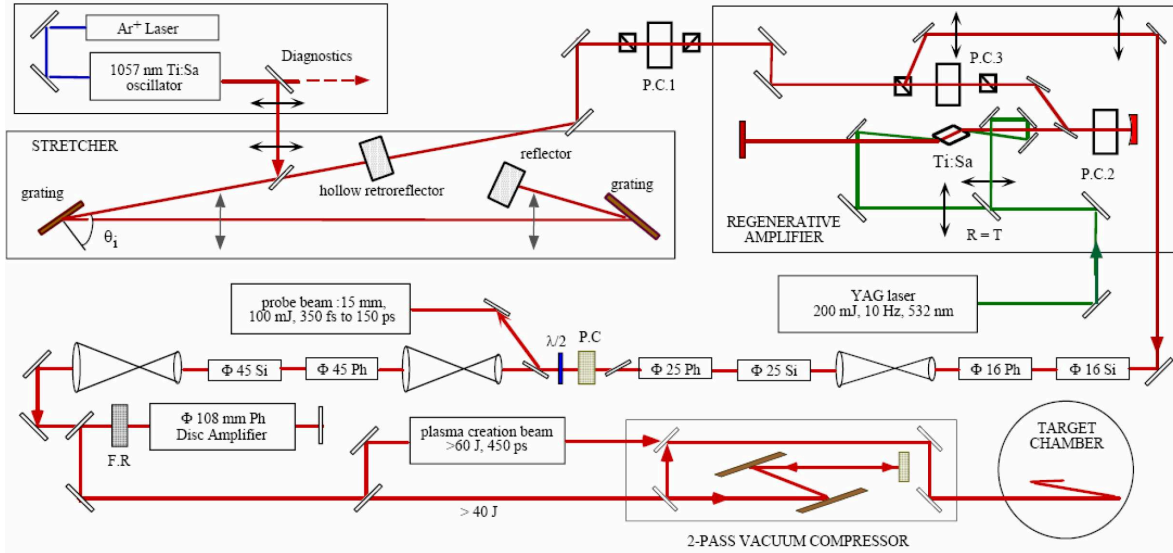


Figure 3.8: Schematic of 100TW laser system [80]. For details, refer to the text. Si: silicate LSG91-H, Ph: phosphate LHG-8, P.C.: Pockels cell, F.R.: Faraday rotator, S.F.: spacial filter.

Gaussian beam profile, although the amplifiers do not cool down to thermal equilibrium in this period and thus thermal lensing cannot be avoided but compensated.

Using the vacuum compressor, 25 – 30 J in 330 fs (10 J at 2ω) is the maximum output with a contrast ratio of about 10^{-8} in 0.5 ns. The efficiency of the compressor is in the order of 30 – 50 % due to the reflectivity of the gratings. After compression, the FWHM of the pulse is (330 ± 30) fs. The beam is then guided to the interaction chamber under vacuum without passing through any window. It is focused by a dielectric off-axis $f/3$ -parabolic mirror to a spot of about $8 \mu\text{m}$ diameter. Alignment procedures are carried out with the regenerative amplifier only, running at 10 Hz. In our experiments, the maximum energy on target was about 14 J with a pulse duration of 330 fs, yielding intensities $\lesssim (5 \pm 1) \times 10^{19} \text{ W/cm}^2$ at the fundamental wavelength $\lambda = 1057 \text{ nm}$.

3.6.2 Temporal pulse shape - contrast and preplasma formation

Amplified spontaneous emission (ASE) and prepulses within the first nanosecond before the main pulse have a contrast ratio of 10^{-8} .

To maximize the contrast of the main pulse compared to any plateau, the laser pulse can be frequency-doubled ($\lambda = 529 \text{ nm}$). Here, crystal plate is used that converts two photons of 1057 nm wavelength into one photon of 529 nm wavelength. The efficiency of this process is I^2 -dependent and small intensities are converted much less efficient

than the highest intensities. Introducing this mechanism in the compressed beam, the intensity contrast from ASE to the main pulse is better than $C_I = 10^{10}$ [84]. On the other hand, the overall energy decreases by a factor of two, and the shorter wavelength is reacting in a different way with the target, foremost regarding the $I\lambda^2$ -dependence of the ponderomotive potential. The laser pulse is p-polarized¹⁶ (horizontal) at the fundamental-frequency (ω) and s-polarized (vertical) at the frequency-doubled mode (2ω), respectively.

3.7 Radial bulk temperature and $K\alpha$ profiles

In this chapter the measurement of radially resolved plasma emission arising from laser-solid target interactions using K_α x-ray spectroscopy with high spatial, temporal (i.e. gated by the x-ray emission time [72]) and spectral resolution is reported. The results show drastic changes of the shapes of the K_α doublet in the central region of the x-ray emission spot. By using line-shape modeling, we reconstruct the temperature profiles and find steep gradients in the radial direction. The $K\alpha$ -yield dependence on the foil thickness is explained by an electron refluxing model.

3.7.1 Experimental setup

To achieve highest intensities, a laser pulse is focused to diameters of a few micrometers, where lateral gradients of the generated-plasma parameters are expected to be of a similar scale. Thus, in order to achieve precise knowledge on the physical properties, such as the plasma temperature at solid density, high spatial resolution is needed [2, 59]. For example, it was reported [70, 85] that the plasma temperature is a function of the irradiated foil thickness, however no evidence of radial variations of the plasma properties has yet been experimentally obtained at solid density.

The experiment was carried out using the 100TW laser facility (Chapter 3.6). The incidence angle to the target normal was 11° , as shown in Fig. 3.9. For the targets, 25-, 10-, and 5- μm -thick Ti foils, as well as Ti bulk, were used. The 5- μm foil was coated by 250 nm of copper, to eliminate the Ti $K\alpha$ radiation from the hot plasma at the surface of the foil.

¹⁶the laser electric field is parallel to the ground and parallel to the plane which is defined by the incident and reflected beam on the target.

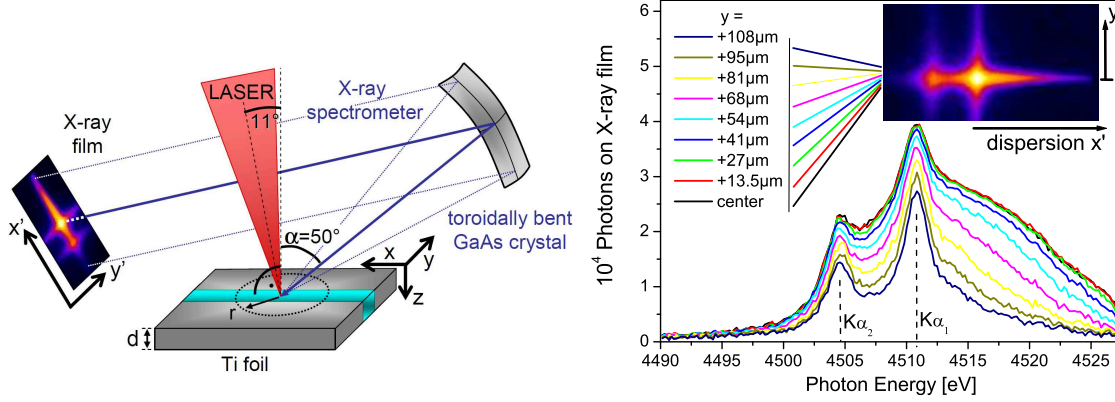


Figure 3.9: Left: Schematic of the experimental setup. The energy dispersion axis x' on the x-ray film is perpendicular to the spatial resolution in y -direction. Right: Single-pulse x-ray spectra of the laser-irradiated $10 \mu\text{m}$ thick Ti foil at laser intensity $I = 5 \times 10^{19} \text{ W/cm}^2$ and $\lambda = 1057 \text{ nm}$, shown from different target positions y . The x-ray film scan (false colors) is given in the inset.

Time-integrated single-pulse spectra of the $K\alpha$ -doublet emission ($4490 - 4530 \text{ eV}$) are detected using the spectrometer described in chapter 3.5.4, in the manner shown in Fig. 3.9.

The measured spectrum $I_M(x', y)$ as a function of the coordinates x' and y (as shown in Fig. 3.9) is the local emissivity $I(E, r, z)$ integrated along both the x -axis and the target depth z , as indicated by the highlighted slice in Fig. 3.9, where conversion from x' to E is obtained by applying a non-linear dispersion relation [73]. Thus,

$$I_M(E, y) = \int_0^d dz \int_{-\infty}^{+\infty} dx I(E, r, z) w(E, r, z),$$

where d is the target thickness and $r = (x^2 + y^2)^{1/2}$. We assume axial symmetry of the $K\alpha$ emission, with the axis perpendicular to the target surface. The term $w(E, r, z)$ is the attenuation factor due to the attenuation length ℓ inside the target:

$$w(E, r, z) = \exp \left\{ - \int_0^z \frac{dz'}{\ell(E, r, z') \cos \alpha} \right\}.$$

Here, $\alpha = 50^\circ$ is the angle between the observation direction and the normal to the target (see Fig. 3.9).

All spectra were recorded using absolutely calibrated Kodak Industrex x-ray film, as described in chapter 3.5.5. Together with the known crystal efficiency, we are able to

infer absolute photon numbers. The films were scanned along the spatially resolved axis by means of a Zeiss densitometer with steps of $y = 13.5 \mu\text{m}$, yielding an optimal signal-to-noise ratio.

The bent-crystal spectrometer yields 1D resolved spectra of the plasma emission, as shown in Fig. 3.9. In this exposure a $5 \times 10^{19} \text{ W/cm}^2$ intense laser pulse at the fundamental wavelength hit a $10 \mu\text{m}$ thin Ti foil. From the center of emission up to $y = 27 \mu\text{m}$, i.e. very close to the laser focus, we observe the same profile and emissivity. Then, a dramatic change of the profiles is observed with every further step of $13.5 \mu\text{m}$. All profiles show a significant blue wing and a rather smooth profile without additional peaks, and we observe no shifted position of the $K\alpha_1$ and $K\alpha_2$ components.

Now we assume that contribution of the resonant self-absorption in the plasma to ℓ is minor. Thus, we use $\ell = \ell_0 = 20 \mu\text{m}$ of the solid-state titanium, which is practically constant over the rather narrow spectral range of interest [86], i.e., w is solely a function of z , $w(z) = \exp(-z/(\ell_0 \cos \alpha))$. For the thin foils, we note that d is comparable to or smaller than $\ell_0 \cos \alpha$, and the attenuation is rather minor, e.g., giving $w \approx 0.5$ for photons coming from the back side of a $10 \mu\text{m}$ foil. On the other hand, spectra obtained from bulk targets represent mostly the radiation from the front-side $20\text{-}\mu\text{m}$ -thick layer.

By applying the inverse Abel transform [87] to the measured spectrum, we obtain

$$\bar{I}(E, r) = \int_0^d dz \exp\left\{-\frac{z}{\ell_0 \cos \alpha}\right\} I(E, r, z) .$$

Thus, the Abel inversion recovers the radial dependence of the plasma emission; the spectrum inferred, however, is averaged (with the proper weight $w(z)$) over the target depth d .

For each photon energy, we applied the inverse Abel-transformation using the *onion-peeling* method [88], yielding radially resolved spectra in steps of $13.5 \mu\text{m}$. In detail, the choice for the two-dimensional data sets of this article was to apply an iterative code, perfectly adapted to our requirements, based on geometry calculations of concentric emission areas A_j^i with radii $i \times 13.5 \mu\text{m}$ and j the segment index as shown in Fig. 3.10. The code starts with a spectrum $S(0)$, $100 \times 13.5 \mu\text{m}$ far away from the irradiation center. We observe no plasma emission from this area within the spectral range of the x-ray spectrometer. This spectrum $S(0)$ is normalized in intensity to an emitting unit area and called $R(0)$:

$$R(0) = \frac{S(0)}{A_0^0} . \quad (3.4)$$

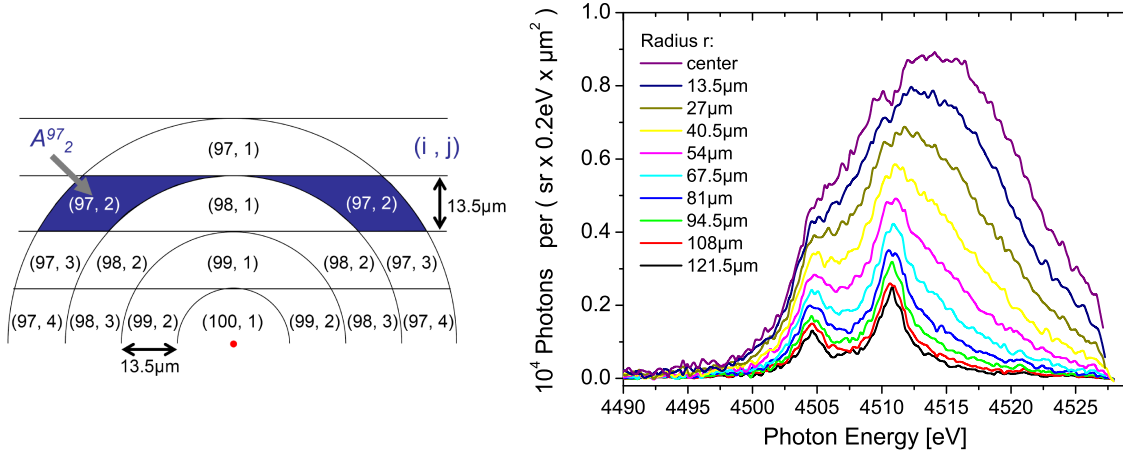


Figure 3.10: Left: Illustration of the discrete Abel inversion applied to the measured spectra. The plasma emission is assumed to be cylindrically symmetric and divided into segments with radius index i and segment index j . The emission from a lateral strip is then converted into the emission from a certain radius. Right: Radially resolved Ti-K_α spectra obtained by Abel-deconvolution from spectra of Fig. 3.9. While for regions with $\geq 120 \mu\text{m}$ distance from the emission center, we observe a narrow doublet structure, the center of emission shows a strongly broadened and blue-shifted shape and factor 4 increased peak emission.

Next, the spectrum from a lateral strip $13.5 \mu\text{m}$ closer to the center, $S(1)$ is treated as a sum of the radial spectrum at this position, called $R(1)$, and $R(0)$. The weighting ratio is calculated by the contributing geometrical areas A_j^i . The recapitulatory iteration formula is given in Eq. (3.5) for $i = 1$ to 99:

$$R(i) = \frac{S(i)}{A_0^i} - \sum_{j=1}^{i-1} \frac{A_j^i}{A_0^i} R(j). \quad (3.5)$$

A drawback of this iterative process is possible accumulation of noise, which can make a reasonable reconstruction impossible. Therefore, cautious filtering was applied to the spectroscopic data where the noise level significantly exceeded the K_α -signal.

Figure 3.11 shows radially resolved Ti-K_α spectra obtained by the Abel transformation of the data presented in Fig. 3.9. At radii $\geq 120 \mu\text{m}$ we observe a narrow doublet structure, similar to those obtained from an x-ray tube. Close to the emission center, a blue wing emerges on both lines. For radii $\leq 30 \mu\text{m}$, the fine structure is completely smeared, resulting in a broad line profile with a maximum at $\approx 4515 \text{ eV}$, a FWHM of $\approx 20 \text{ eV}$, and an integrated emission $11\times$ stronger than that at $r = 120 \mu\text{m}$.

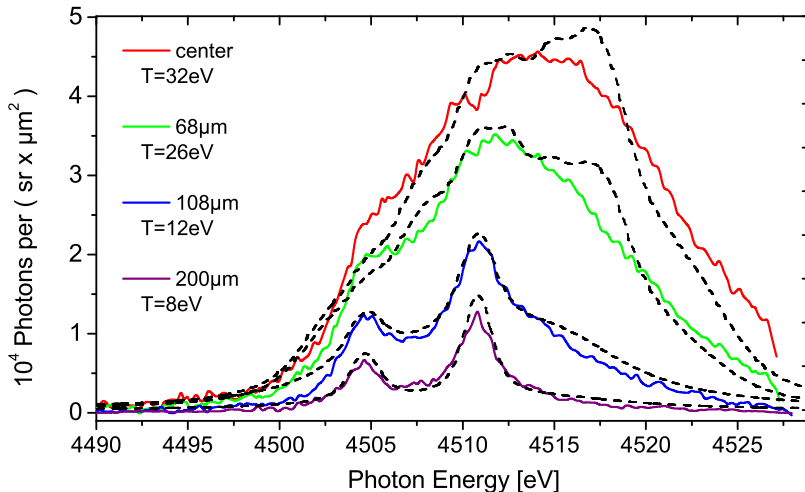


Figure 3.11: Comparison of assorted Abel-inverted experimental spectra (solid lines) from irradiation of a $10 \mu\text{m}$ Ti foil and the best-fit modeled spectra (dashed lines).

3.7.2 Radial profiles

We use the spectra from [66] to fit the deconvoluted data in order to determine the radially resolved T_e , see Fig. 3.11. For higher temperatures, significant contributions of higher ionization stages and excited-state satellites affect the line-shape, resulting in the “blue” shift and broadening of the $K\alpha$ spectrum; the Stark broadening contributes to the “smoothing” of the entire line shape. The error-bars were determined by varying T_e around the best-fit value (which gives a minimal χ^2) up to a 50% increase in χ^2 . As seen in Fig. 3.11, a good agreement was achieved for all radii. Applying this procedure for every data set, T_e is inferred with a $13.5 \mu\text{m}$ resolution. At radii $\geq 200 \mu\text{m}$ we observe the line-shape of cold titanium. The line-shapes do not change significantly below $T_e \approx 5 \text{ eV}$, resulting in relatively large error bars at large radii.

The radial temperature profiles and $K\alpha$ -yield for both lower laser contrast (ω) and high laser contrast (2ω) are presented in Fig. 3.12. The maximum temperature is constantly $\sim 30 - 40 \text{ eV}$ within the error bars. At ω , this temperature extends over $\sim 50 \mu\text{m}$ which is an order of magnitude larger than the laser focal spot. Its radius is increasing for thinner foils, especially for the $10 \mu\text{m}$ -foil. The $5\text{-}\mu\text{m}$ foil has a smaller hot area with $r \approx 50 \mu\text{m}$, however, the maximum temperature exceeds 40 eV .

For the 2ω exposures, we find a more systematic dependence: both the maximum temperature and the heated area radius rise when the foil thickness decreases. The temperatures rise from 32 eV to 37 eV , while the radii range from 30 to $60 \mu\text{m}$. Further, the $K\alpha$ -yield decreases with thinner foils. At larger radii temperature gradients of $\sim 1 \text{ eV}/\mu\text{m}$ are present.

Although some of the inferred dependences can be attributed to pulse-to-pulse laser-parameter variations, a strong correlation between the spatial distributions of $T_e^{(\text{bulk})}$ and

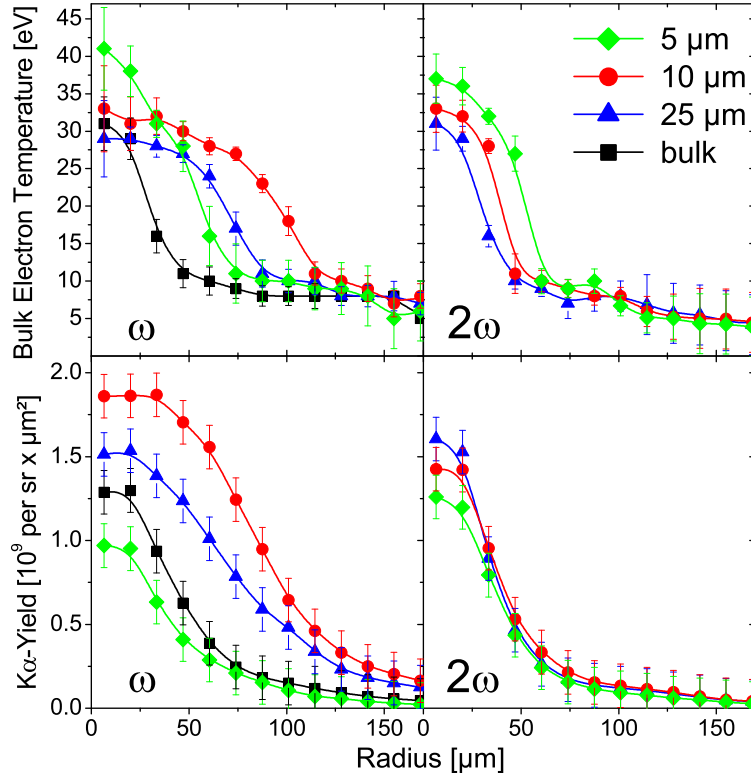


Figure 3.12: Radial temperature (top) and integrated $K\alpha$ -yield (bottom) distributions of the different targets used, irradiated with the ω and 2ω laser pulses.

$K\alpha$ -yield is observed in each single-pulse measurement, see Fig. 3.13, where the FWHM values of these distributions are shown for different target thicknesses, both for ω and 2ω pulses. These results show that there is a strong correlation between the mechanism(s) responsible for the radial distribution of the electrons with $E > 5$ keV (that give rise to the $K\alpha$ radiation), and those of the WDM bulk-heating, indicating that for the latter, the faster electrons could play an important role.

The differences of the 2ω exposures compared to the ω ones are most likely related to the significantly suppressed laser-preplasma interaction due to the higher contrast ratio. Hydrodynamics simulations [84] show that for a metal foil the surface of critical electron density $n_{\text{crit}} \approx 10^{21} \text{ cm}^{-3}$ has moved $\approx 10 \mu\text{m}$ away from the foil as a result of the prepulse. At ω , only the 5 μm -foil shows a comparatively small heated area. This may also be related to preplasma formation. As already mentioned, this foil was coated with 250 nm of copper, where the preplasma formation is likely. We note that this may also be responsible for similar radial distributions for this foil (see Fig. 3.13), contrary to the other targets.

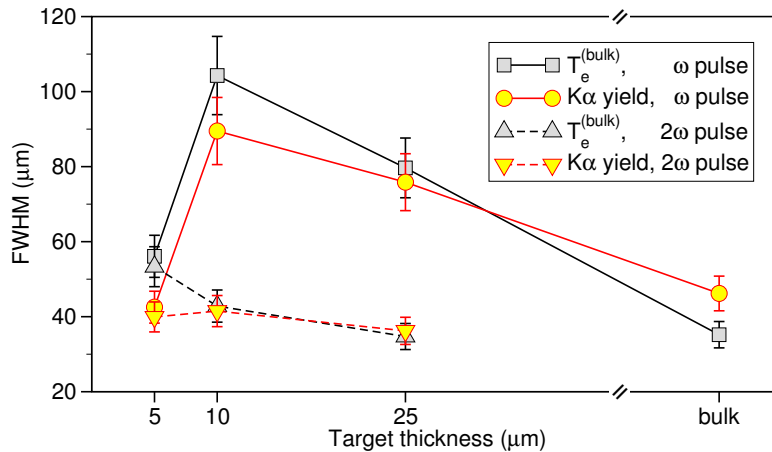


Figure 3.13: Distributions (FWHM) of the bulk-electron temperature compared to the $K\alpha$ -yield radial distributions for different targets and laser pulses. A strong correlation between the FWHM values for each individual exposure is obvious.

3.7.3 Temperatures and spot sizes

Figure 3.14 (top) illustrates the spatial properties of the plasma emission from the fundamental frequency-exposures at two different x-ray energies: The emission area (FWHM radius) of the ‘cold’ $K\alpha_1$ -emission reaches $50 \mu\text{m}$ at foil thicknesses of 25 and $10 \mu\text{m}$. These radii are more than 6 times larger than the laser focal spot. Further, the emission of the blue wing at $4516 - 4522 \text{ eV}$ is analyzed. For the $5 \mu\text{m}$ -foil, its FWHM is in the order of the laser focus diameter, while for the $10 \mu\text{m}$ -foil it is twice as large. In all cases, the emission area decreases for bulk and for the $5 \mu\text{m}$ -foil, which is accompanied by a rise in maximum temperature as shown in the bottom part of Fig. 3.14.

Hydrodynamic motion

We irradiated a $2 \mu\text{m}$ thin pure titanium foil with the fundamental laser frequency. However, we did not observe a further increase in temperature as it was reported before [70]. The prepulse at the fundamental laser frequency ω generates an energy density of $\sim 1 \text{ kJ/cm}^2$ at the focal spot within half a nanosecond. Hydrodynamics simulations using the one-dimensional HELIOS code [89] yield to the insight that the first μm of the foil volume is ablated and expands into the vacuum, while the other half of the foil is pre-heated. The density in the remaining foil volume increases temporarily by a factor of two due to a shock-wave, see Fig. 3.14. When the main pulse arrives after 0.5 ns , the foils has already turned into a complex density gradient. Since the line-shape modeling assumes solid density, our model has large error bars for thin foils $d < 5 \mu\text{m}$. Hence, the results for these foils are excluded from the temperature analysis.

Eventually, it is shown [56] that the high contrast 2ω pulse, verified to create negligible preplasma [84], will not inject a large number of hot electrons into the solid for two

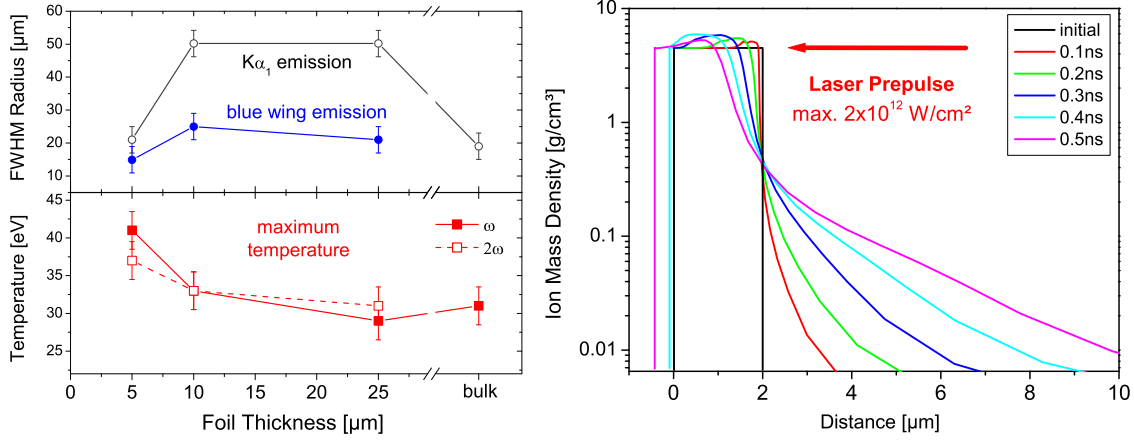


Figure 3.14: Left TOP: The emission area (FWHM radius) of emitted $K\alpha_1$ -photons (integration from 4508 – 4512 eV) and the photons emitted by the blue wing (4516 – 4522 eV), as a function of target thicknesses at ω . BOTTOM: Maximum bulk temperature as a function of target thickness for ω and 2ω . Right: Hydrodynamics simulation of the laser prepulse hitting a $2\ \mu\text{m}$ Ti foil using the 1D HELIOS code. The prepulse is assumed as a linear ramp, reaching $2.5 \times 10^{12}\ \text{W}/\text{cm}^2$ after 0.5 ns. At this time, the main pulse arrives and interacts with both a lower-density preplasma and $\sim 1.5\times$ compressed residual foil.

reasons: (1) pre-ionization is suppressed and therefore the laser pulse interacts with a steep density gradient [90], and (2) the temperature of the electron distribution scales with $T_{\text{hot}} \sim (I\lambda^2)^{0.3-0.5}$ [43, 47]. Here, I is the laser intensity which is $\sim 50\%$ lower for the frequency-doubled laser beam compared to the fundamental one, and λ is its wavelength. Thus, we get $T_{\text{hot}}^{2\omega} = (0.35 - 0.5)T_{\text{hot}}^{1\omega}$. These mechanisms are counterbalanced by the fact that more laser energy can be brought to the target, because the critical density is higher for shorter wavelengths, and preplasma formation is suppressed. At last, the achievable laser focal radius $w_0 \approx \lambda/(\Theta \cdot \pi)$ is theoretically smaller with shorter wavelength for constant beam divergence Θ .

Electron distribution

Our results contain three-dimensional information on the characteristic x-ray emission of the generated plasma, but we have no measured information on the distribution of electrons, neither in space nor energy. Anyhow, we can draw conclusions from the x-ray emission by applying the relativistic cross-section σ_K for titanium K-shell ionization [60].

This cross-section reaches a maximum at electron energies of 15 keV, and has $\sim 60\%$ lower but nearly constant value for $E > 100$ keV. A significant fraction of fast electrons

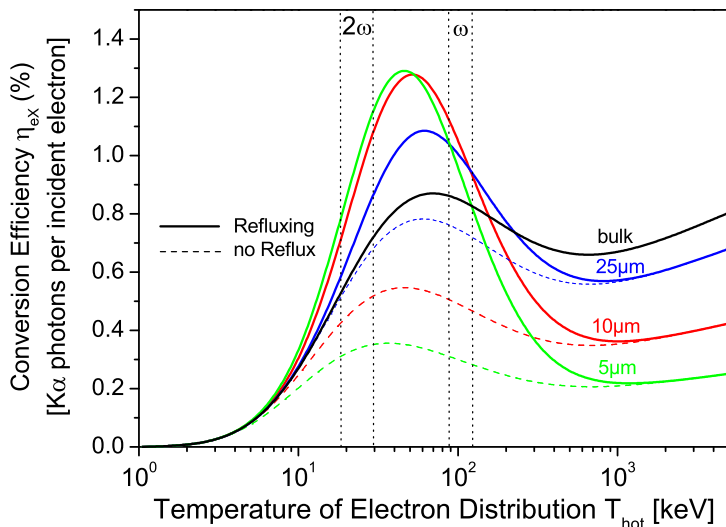


Figure 3.15: The measured x-ray yield, together with the theoretical conversion efficiency of an electron distribution of temperature T_{hot} into K_{α} photons for different Ti foil thicknesses. The solid lines account for refluxing of electrons with $E < 100$ keV, compared to the dashed lines with no refluxing. The marked areas indicate the electron temperature estimate for the ω and 2ω exposures, respectively.

with kinetic energies $E \geq 500$ keV escapes the target and can be detected [58]. This charge-separation is the source of strong electric fields up to $\text{MV}/\mu\text{m}$ [91] at the foil boundaries. Otherwise, the mean free path of electrons with $E < 100$ keV is in the order of tens of micrometers, but they are most probable confined to the target foil by the strong electric field and deposit their kinetic energy inside the foil by traversing it several times ('refluxing'). Thus, electrons with energies up to a few hundred keV are the dominant source of K-hole creation.

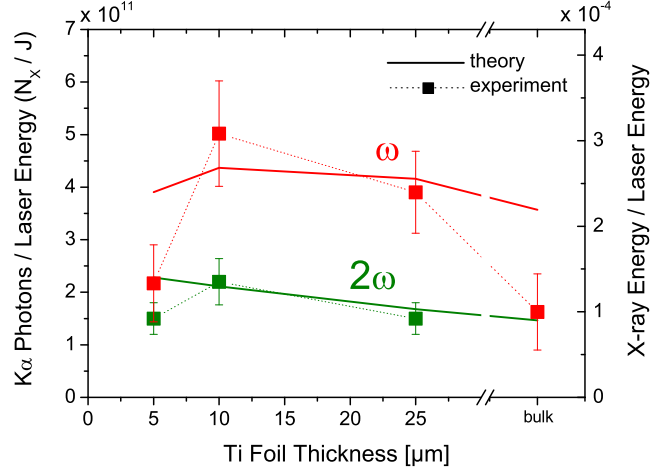
The properties of K-shell emission as discussed within this thesis are sensitive to the low-energy part of the electron distribution: while electrons with $k_B T \geq 5$ keV are capable of K-shell ionization, the creation of L-shell holes and even M-shell holes is dominated by slower electrons with ≥ 500 eV. M-shell holes affect the K_{α} line shape by blue shifting, as observed in the presented data, and serve as bulk-electron-temperature indicator. This general picture is complicated by effects like secondary electrons, radiation heating and electron-electron interaction.

X-ray yield

The conversion efficiency of optical laser energy in x-ray photons in a narrow bandwidth ΔE is a highly important value for time-resolved x-ray diffraction, backlighting applications such as shadowgraphy, or x-ray Thomson scattering [92]. For laser-driven x-ray sources with fs-pulse length, the absolute number of K_{α} photons per laser energy ($1/J$) emitted in a 4π -sphere is a meaningful quantity for comparison to other experiments, as well as the conversion efficiency of laser-energy to energy of K_{α} -photons.

Figure 3.15 shows seven individual measured yields: the data for three different foil

Figure 3.16: The yield, emitted K_α photons in a 4π -sphere in an energy range of $E = 4490 - 4530$ eV per incident laser energy as a function of target thickness. Further, the right ordinate shows the ratio of x-ray energy to laser energy. The squares represent our measurements, while the solid lines are theoretical values deduced from Fig. 3.15. To match our experimental results, a laser absorption of 50% was assumed for ω , and 10% for 2ω , respectively.



thicknesses as well as bulk were analysed for ω and 2ω laser frequency irradiation. For the ω -exposures, we find a nearly constant yield for the 10 and 25 μm -foils, and for bulk and the 5 μm -foil, respectively. The increase by a factor of 2.5 for the first ones compared to the latter is remarkable. However, the exposures at 2ω do not show this pronounced dependance on foil thickness.

In order to model the measured x-ray yield, we employ Monte-Carlo (MC) simulations [15] to calculate the conversion efficiency η_{ex} from electrons into K_α photons. As initial electron distribution, a relativistically-correct Maxwell-Juttner function is assumed. If these electrons traverse the foil only once, i.e. refluxing is neglected, thicker foils will emit more photons, only limited by reabsorption, as shown in the dashed curve in Fig. 3.15. This is in clear contrast to our observations.

Thus we extended the MC model to account for refluxing: electrons with an energy $E > E_{crit}$ are assumed to escape the target space-charge, while slower electrons are reflected inside the foil boundaries. The solid curves in Fig. 3.15 show that if $E_{crit} = 100$ keV is assumed, the overall efficiency is increased. For the 5–10 μm foils, it reaches a maximum of $\eta_{ex} = 1.3\%$ at $T_{hot} = 50$ keV, while it is only around 0.4% at $T_{hot} \geq 1$ MeV. For thicker foils, the effect of refluxing electrons is less pronounced, and it is negligible for bulk material. Qualitative agreement with the measurements regarding the target thickness dependence at ω is achieved at electron temperatures around 100 keV. Another model derived by THEOBALD ET AL. [93] accounts for total refluxing, i.e. all electrons are confined to the target foil. They predict a general increase of the yield, especially for few MeV electron distributions. Anyhow, their model cannot reproduce the observed dependence on foil thickness.

Let us therefore assume an electron distribution with $T_{\text{hot}} = 100$ keV for all exposures at ω laser frequency. From the scaling laws discussed above, the hot electron temperature for 2ω is then in the order of 35 keV. An upper limit for the number of electrons is known by assuming that 100% of the incident laser energy is converted into electrons, independent of target thickness. Then we apply the conversion efficiency from Fig. 3.15 and gain a prediction for the $K\alpha$ -yield. In order to match this result with the experimental data as shown in Fig. 3.16, we have to assume 50% and 10% conversion of laser energy into hot electrons for ω and 2ω , respectively. Within typical error bars, these numbers agree with previously published values [93, 94, 95].

At the fundamental wavelength, the large amount of free electrons in the preplasma as well as preheated foil both result in an increased luminosity, compared to the exposures at 2ω . This is probably also the reason for the larger emission area shown in Fig. 3.12. Further, the derived electron temperatures are about one order of magnitude lower than one would expect from the general scaling laws. Note that these were derived from slope of the high-energy tail of the time-integrated distribution, while the production of K-shell vacancies strongly depends on electrons at only several tens of keV within the first picosecond after irradiation. Thus our electron temperature is valid for the distribution of keV electrons, which are usually not accessible by electron spectroscopy at the target rear side.

Note that the intensity in these experiments of several 10^{19} W/cm² is about two orders of magnitude too high for efficient $K\alpha$ generation in titanium, since the peak of the hot electron distribution does not overlap with the peak of the K-shell ionization cross-section [15, 27].

Energy deposition in the depth of the target

Usually, the $K\alpha$ -yield, and deposition of energy into the target in general, are also a function of foil depth, which will lead to a depth-dependent bulk electron temperature [96]. As discussed, we have results with high lateral resolution, but averaged over the target depth, weighted by the attenuation factor for $K\alpha$ photons in titanium. However, the Monte-Carlo Code, including refluxing, yields depth-dependent information on the energy-loss of the hot electrons. Figure 3.17 shows the probability of K-shell ionization for electron distributions with temperatures of 100 keV and 35 keV, respectively. These temperatures are identified with irradiation using the fundamental wavelength and the frequency-doubled pulse. Due to the refluxing of electrons, the thin foils show a higher concentration of K-holes than the thick ones. Further, the depth-dependency is negli-

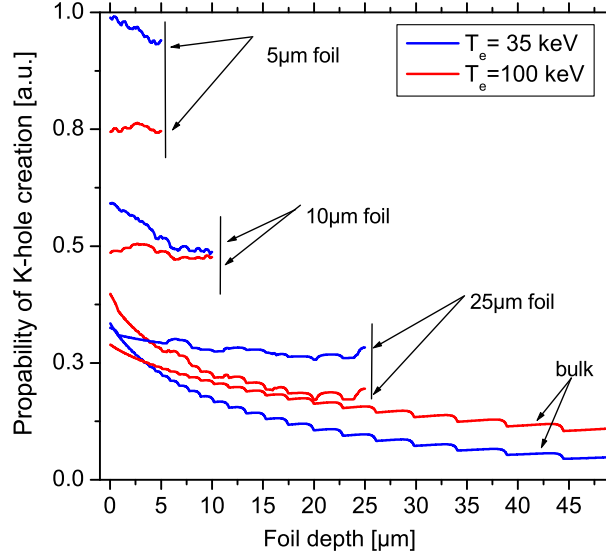


Figure 3.17: Results from Monte-Carlo Simulations of the depth-dependent K-shell ionization probability for two hot electron temperatures and the different Ti foil thicknesses discussed in this work. Refluxing of electrons is treated for all foils, and no refluxing is assumed for the bulk target.

ble for foil thicknesses up to 10 μm , and only the 25 μm foil and the bulk target (without refluxing) show a drop of the K-hole concentration. Anyhow, the concentration at 20 μm target depth, which is the attenuation length, is not more than $\sim 60\%$, compared to the irradiated surface. Further, the slower electrons from the 35 keV-distribution deposit more energy in the first 5 μm of each foil, while the faster electrons with $T_e^{\text{bulk}} = 100$ keV lead to a more homogeneous deposition of energy.

Brilliance limitations

Laser-driven x-ray sources are suitable to probe the dynamics of solid-density plasma [97]. Prominent examples are time-resolved x-ray diffraction or x-ray Thomson scattering. While maximum yield and short duration of the x-ray emission are crucial in both cases, the latter case further needs a narrow bandwidth of $\Delta E/E = 0.01$ for non-collective scattering [98] and $\Delta E/E = 0.002$ for collective scattering [99], respectively. Straightforward from our findings the plasma emits the ‘cold’ line-shape suitable for collective scattering only if its temperature does not significantly exceed 20 eV. Beyond this value, the emission is broadened and blue-shifted, which affects also the application of x-ray optics such as monochromatic imaging [73]. The use of thicker foils on the other hand results in a longer x-ray pulse duration [15].

The peak brilliance

$$B = \frac{\text{Number of } K_\alpha \text{ - photons}}{s \times 0.1\% \text{bw mm}^2 \text{ mrad}^2}$$

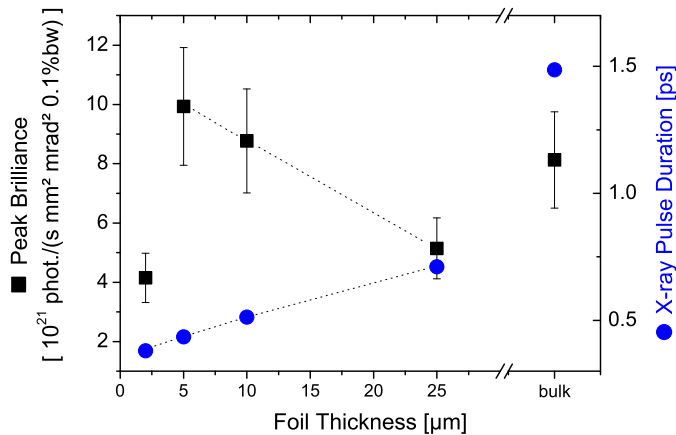


Figure 3.18: Peak brilliance (squares) and estimated x-ray pulse duration (circles) as a function of foil thickness for irradiation at the laser fundamental. A foil thickness of 5 – 10 μm fulfills both high brilliance and sub-picosecond pulse duration.

is defined as the flux (photons per second in a limited bandwidth) per emission area and solid angle. Gathering our results and applying the x-ray pulse duration inferred from our Monte-Carlo simulations, we plot the peak brilliance in Fig. 3.18 as a function of foil thickness d . Note that the pulse duration is possibly prolonged by the refluxing electrons. As illustrated in Fig. 3.14, the laser ASE prepulse evaporates $\sim 50\%$ of the 2 μm -foil, which results in a decreased emitted photon number. A foil thickness of 5 – 10 μm fulfills both high brilliance and sub-picosecond pulse duration, while the bulk target emits a ~ 1.5 ps pulse.

3.8 Summary

Although femtosecond lasers are able to deliver several Joules of energy into a μm^3 volume, the creation of a *defined* state of warm dense matter is challenging. First, the irradiated spot is only a few micrometers in diameter, resulting in strong gradients. Second, the heating of a solid is indirect by relativistic electrons, since optical light itself cannot penetrate electron densities exceeding 10^{21} cm^{-3} . Third, the creation of these electrons by the laser is an extremely non-linear process. Therefore, the investigation of these processes with high spectral and spatial resolution is of primary importance. The advantage of such a plasma is a sub-picosecond x-ray spectral line emitted from a small spot, suitable for backlighting. Further, the generation of electrons that heat high-density matter is a mayor issue in fast ignition. These facts are motivated in chapter 3.

The key technology in this field is x-ray spectroscopy with highest resolution. The electrons traversing the target create vacancies in the inner shells. Recombination of the K-shell leads to the emission of characteristic x-rays. These are reliable carriers of information, since their line-shape is influenced by the plasma parameters, and they

penetrate solid density. In chapter 3.5, we derive the physical and technological boundaries to design and apply a toroidally bent, 1D-focusing spectrometer for the titanium $K\alpha$ doublet. The efficiency of the spectrometer and the employed x-ray film detector are known, so that we can measure absolute photon numbers.

Laser-matter interaction experiments were conducted at the 100TW laser facility at LULI (chapter 3.6). We focus a few μm diameter spot onto thin titanium foils, reaching intensities of several 10^{19} W/cm^2 both at the fundamental and the frequency-doublet beam. By using Abel-inversion, we gain radially resolved spectra of the $K\alpha$ emission. The line-profile is compared to temperature-dependent calculations, yielding radially resolved bulk electron temperature maps.

In the experiments, the generated plasma shows a rather homogeneously heated core up to an order of magnitude larger than the laser focal spot, with a strong similarity between radial distributions of the bulk-electron temperature and the $K\alpha$ -yield. The influence of a thin coating on the $5\mu\text{m}$ -foil results in both a decreased spot size and $K\alpha$ -yield. When the laser frequency is doubled and the intensity contrast is increased to 10^{-10} , the inferred distributions become about twice narrower and show a clear dependence on the foil thickness: the generated plasma from thin foils is hotter and the yield is lower.

The line-shape at the emission center changes drastically compared to the 'cold' $K\alpha$ -doublet observed at large radii: we observe a single broad line with a FWHM of 20 eV. Further the central photon energy is blue-shifted to 4514 eV. The radiation is emitted by plasma with temperatures up to 42 eV.

We further measured the global $K\alpha$ -yield as a function of target thickness d and observe a maximum yield for foil thicknesses of $10-25\mu\text{m}$. These results are explained by means of an electron refluxing model. Since the laser-generated electrons have energies ranging over several orders of magnitude, we model the K-shell ionization cross-section with an empirical relativistic model. Monte Carlo simulations based on this cross-section can explain our observations if refluxing of electrons with $E < 100\text{ keV}$ is assumed. Hence, parameters are derived that allow optimization of the brilliance of such x-ray sources.

These results are of primary importance for basic understanding of laser-matter interaction, benchmarking computer simulations, and various applications, such as fast ignition for laser fusion and laser-driven backlighters. Future research in this field will concentrate on how the plasma temperature depends on the target thickness and depth. Further, time-resolved measurement of the x-ray emission by means of streak-cameras, and the contribution of refluxing electrons are in our focus.

4 Intense soft x-ray matter interaction

4.1 Introduction

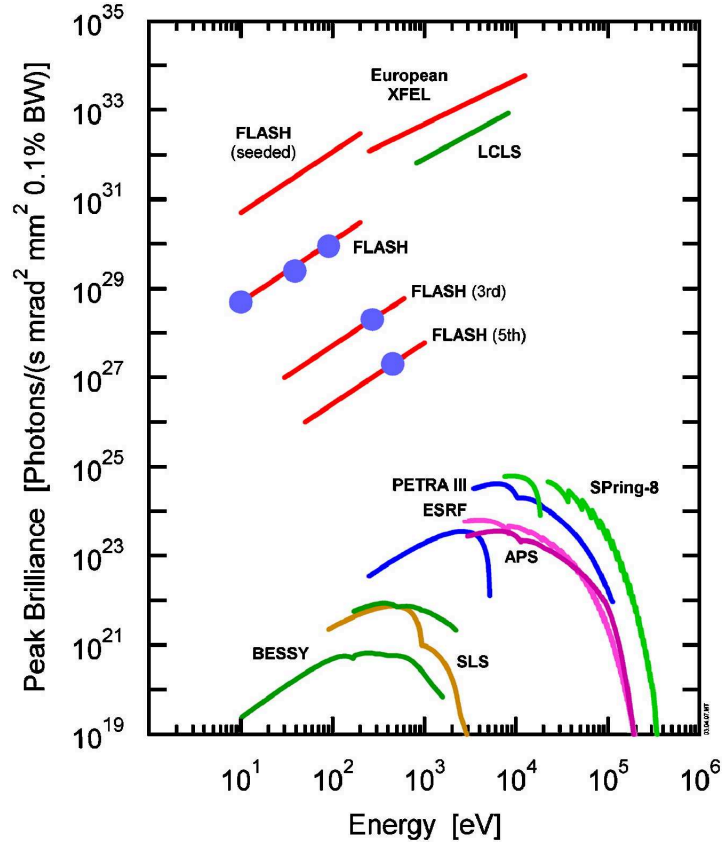
Intense XUV pulses reaching up to several giga-watts of peak power with a pulse-width in the femtosecond range have been sought for by many experiments where the controlled deposition of energy in solid-density matter is necessary. A great step forward was achieved when free electron lasers based on the **S**elf **A**mplified **S**pontaneous **E**mission (SASE) [101] principle became available.

A **F**ree **E**lectron **L**aser (FEL) produces coherent electromagnetic radiation like a classical laser, but uses entirely different principles to form the lasing medium. The lasing medium is a relativistic electron beam, which corresponds to the bound atomic or molecular states for conventional lasers. In a FEL, a relativistic electron beam passes through a periodic transverse magnetic field of an undulator, where it is forced to perform a wiggling path. The acceleration of the electrons along this path results in the release of photons. Mirrors capture the released photons to generate resonant gain through the combined interaction of the electron beam with both, the undulator field and the radiation field stored in the optical resonator formed by the mirrors. At wavelengths where no good mirrors exist, a so-called high gain FEL can reach a resonant gain and saturate in a single passage along the undulator. The wavelength of the photons can be tuned using the electron beam energy and the magnetic field strength of the undulator. Compared to conventional lasers, this gives more flexibility to the FELs in the wavelength range coverage and tunability. Operational FEL facilities currently are ranging from microwaves to x-rays¹.

Since XUV FELs were not available until 2004, the physics of both the absorption process and the creation of plasma states using this new source had to be experimentally developed. Currently this field is experiencing a new stimulus. The FEL sources produce extremely intense, polarized and coherent radiation with gigawatt peak power. Their

¹The first lasing at 2 keV photon energy and few mJ pulse energy at LCLS in Stanford was reported in September 2009.

Figure 4.1: Peak brilliance of free electron laser sources in comparison with third generation synchrotron radiation facilities, taken from [100]. Obviously, the third generation synchrotron radiation sources with their typical undulator-based spectral range lie several orders of magnitude below the fourth generation light sources. The dots associated with FLASH are actual measurements, while the lines represent theoretical predictions.



peak brilliance exceeds that of modern third generation synchrotron radiation sources by orders of magnitude over a wide range of photon energies, see Fig. 4.1. In particular, at a photon energy of 100 eV, which was used in our experiments, the FEL peak brilliance is more than seven orders of magnitude brighter than any currently available synchrotron source. It was a challenge to conduct these experiments at the first facility of its kind and infer exciting results.

4.1.1 The FLASH-facility

The **F**ree **E**lectron **L**ASer in **H**amburg (FLASH) [102, 103], the successor of TTF1², at DESY is an FEL based on SASE principle and presently delivers very intense light in the wavelength range 50 nm to 6.5 nm in the first harmonic.

The layout of the FLASH linear accelerator (linac) is shown in Fig. 4.2. Briefly, electron bunches of ~ 1 nC charge are generated by a laser driven photocathode. These are subsequently accelerated by six linear accelerator modules, each with eight 1m-long

²Tesla Test Facility 1, it demonstrated saturation of the SASE amplification process in the wavelength range 80 – 120 nm.

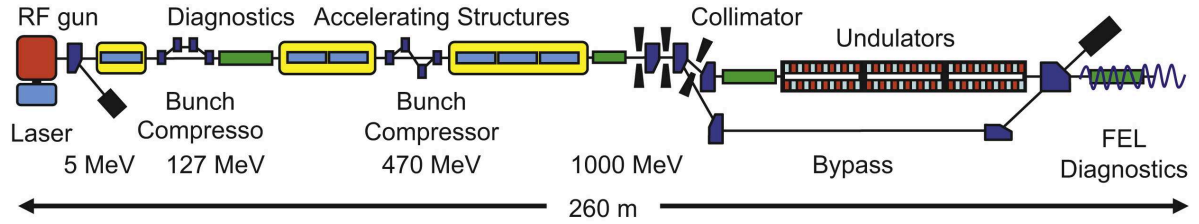


Figure 4.2: Schematic of the FLASH facility. Electrons are generated by the RF gun located on the left, then accelerated by the acceleration structures, and brought to lasing in the undulators. The emitted XUV pulses are guided towards the experimental hall located on the right.

superconducting 9-cell cavities. This acceleration provides energies between 450 MeV up to 1 GeV. Two magnetic chicanes, called bunch compressors, accomplish the main longitudinal compression of the electron bunches. Then, six undulators compose the FEL for FLASH, each 4.5 m long and with a magnetic period of 2.73 cm. Macro-pulses of electrons can consist of up to 30 sub-bunches. The repetition rates of the macro-pulses at FLASH is 5 Hz. The FEL has been used routinely in a wavelength range between 6.5 and 50 nm with typical pulse energies of 10 – 100 μJ and pulse durations of 10 – 15 fs. Extraordinary performance has been achieved at 13.5 nm wavelength with strong higher harmonics reaching into the water window [100]. In particular, a single photon-pulse energy of up to 100 μJ with pulse-width of 10 fs at a photon wavelength of 13.4 nm has been obtained during our user beamtimes.

The pulse duration was first inferred from the spectrum of the pulse. At 13.5 nm, it is expected to be in the order of 10 – 15 fs [103]. Recent developments in instrumentation included the availability of an XUV-autocorrelator, and a first direct measurement of the pulse duration of (29 ± 5) fs at a wavelength of 23.9 nm [104] was successful. Further, a single-shot terahertz-field-driven x-ray streak camera was set up, yielding a pulse duration of (35 ± 7) fs at 13.5 nm wavelength [105]. However, these three citations for a pulse duration represent also three different operation modes of the FEL. The pulse duration will be increased if more electrons in one bunch contribute to the lasing process. This is related to the electron phase-space, the bunch compression and coulomb forces in the bunch. The latter is influenced by the bunch charge, i.e. the number of electrons, which in turn means that a low or moderate charge produced at the photocathode produces more likely a short pulse than a large charge.

4.2 XUV photo-absorption by Aluminum

The photon energy of the XUV or soft x-ray radiation discussed in the framework of this thesis is ~ 92 eV. Unlike the low photon energy of infrared lasers (~ 1.5 eV), the

XUV radiation is comparable to the binding energy of inner-shell electrons.

In optical laser-matter interaction, dominant absorption mechanisms are multi-photon ionization, nonlinear processes, inverse bremsstrahlung, and resonance absorption [51]. When the critical free electron density of the optical laser is exceeded (10^{21} cm^{-3} at $\lambda \sim 1 \mu\text{m}$), the photons are reflected and absorption is limited to the skin depth c/ω_P , leaving behind a hot plasma with steep density and temperature gradients. Note that the properties of the surface, and therefore ω_p and other related values, change already during the pulse duration.

For XUV photons, nonlinear absorption is negligible at the considered intensity, and resonance absorption is not important since a solid-density plasma is still undercritical. Thus, “hot” electron production in the keV to MeV range is unlikely. Photo-excitation and inverse bremsstrahlung are the most probable mechanisms. Since there are no prepulses in the FEL case³, the deposition of photons starts in a cold target and the energy is distributed volumetrically and homogeneously throughout the interaction zone. However, the actual dominating absorption process is a function of intensity and target material. E.g., two-photon double ionization of He has been already studied at FLASH [104].

4.2.1 XUV photo-absorption mechanisms

At ambient temperature and pressure, solid aluminum has a filled-shell ionic core ($1s^2 2s^2 2p^6$) with the three free electrons (populating the $3s^2$ and $3p$ levels) in the valence band. As such, it has a relatively deep L-edge. Considering a photon energy of 92 eV, the L_{III} and L_{II} edges are below the photon energy, at 72.7 and 73.1 eV respectively, whereas the L_I is located at 117.8 eV. Experimental values for the absorption coefficient of cold aluminum are well known in this region [86]. The contribution due to free-free absorption (or inverse bremsstrahlung, i.e. due to the valence electrons) in this region is very small compared to the photo-ionization, and we determine values for the photo-ionization absorption coefficient and the free-free coefficient as $27 \mu\text{m}^{-1}$ and $0.2 \mu\text{m}^{-1}$ respectively for cold Al [107]. Therefore, for photons of energy 92 eV, almost all of the absorption is due to photo-ionization of L-shell electrons, see left panel in Fig. 4.3.

³If lasing of the hole electron bunch could be realized, the pulse would have a duration of about 100 fs. Thus, any undulator radiation is limited to this time window.

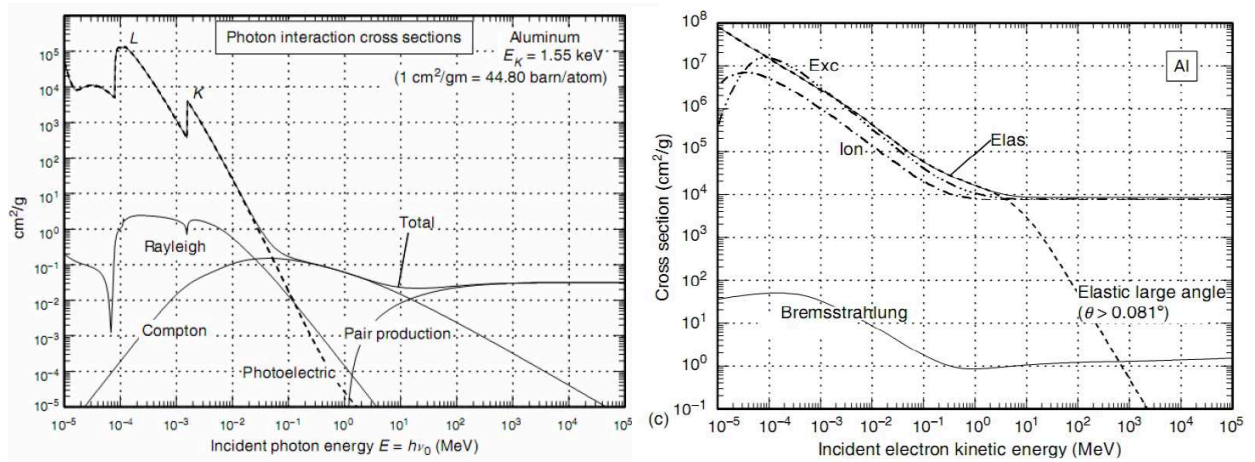


Figure 4.3: Left: Photon interaction cross-section on an isolated cold aluminum atom. Right: Electron interaction cross-section in aluminum, consisting of electron **Exc**itation, **Ion**ization, **Elastic** Scattering and Bremsstrahlung. Both plots are taken from [106].

4.2.2 Conduction band of aluminum

From Fig. 4.4, the band structure and the density of states (DOS) of bulk aluminum can be seen. The colored curves represent the individual contribution of the s , p , and d electrons, while the black curve is the sum of them. Obviously, the DOS does not significantly differ in shape from a free electron gas.

As a good approximation for the DOS, we therefore assume a transition probability $D(E) \propto \sqrt{E - E_B}$. Here, E is energy at the bottom of the conduction band. Then we multiply it by the Fermi function $f(E, T_e) = [1 + \exp(-(E_F - E)/k_B T_e)]^{-1}$ which defines an electron temperature T_e . Aluminum in particular has an L_{III} -edge of 72.7 eV and $E_F = 11.2$ eV, hence the bottom of the valence band is located at $E_B = 61.5$ eV. The total function is $I(E, T_e) = f(E, T_e) \cdot D(E) \cdot E^3$, which was multiplied by E^3 to convert it into a radiative emission flux. The results are shown in the right panel of Fig. 4.4 for different electron temperatures.

4.2.3 Electron equilibration dynamics

After irradiation by 92 eV photons, electrons with an excess energy of $(92 - 72.7)$ eV = 19.3 eV above the Fermi Energy are created.

Subsequently, L-shell holes will be filled with valence band electrons⁴. The dominant

⁴Since the L-shell hole is a 2p-state, no electron from another p-state could recombine to it due to selection rule. Anyhow, the electrons in the conduction band of a metal are strongly correlated, and

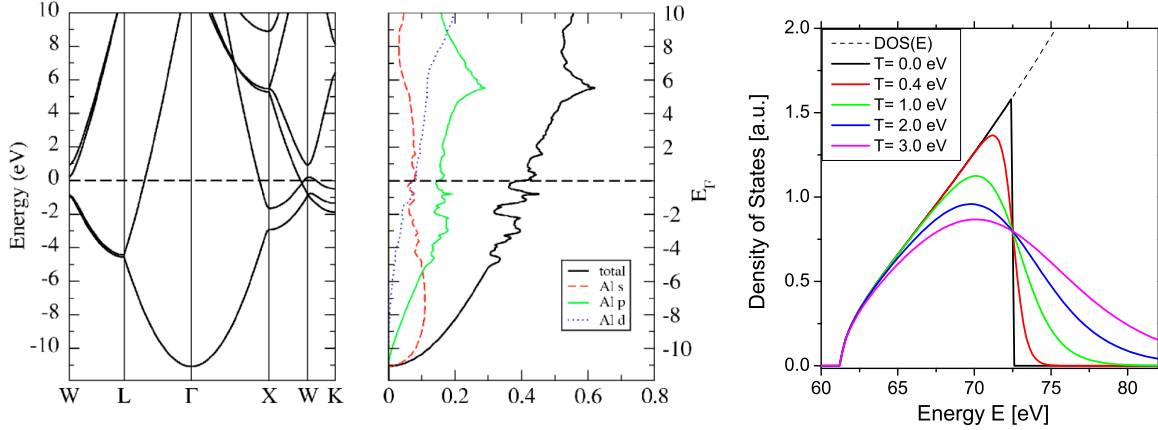


Figure 4.4: Band structure (left) and density-of-states (middle) plots for aluminum from [108]. Free electron gas at different temperatures (right).

mechanism here will be Auger recombination (the radiative yield is only 0.2% [109]), which will heat the valence band electrons, as each Auger-electron will receive about 72 eV of energy. Bremsstrahlung can also be fairly neglected as an energy-loss mechanism as shown in the right panel of Fig. 4.3.

Measured inelastic scattering lengths for electrons 20 eV above E_F in aluminum are between 5 – 10 Å [110], corresponding to time-scales of order 0.85 to 1.7 fs, in good agreement with calculations based on electron gas dielectric theory [111]. Thus the photo-excited electrons rapidly lose their energy and thermalize with the initial cold valence electrons on a time-scale considerably shorter than the FLASH pulse.

4.2.4 Monte-Carlo simulations

In order to understand the electron dynamics of XUV-irradiated bulk aluminum better, the electronic distribution was calculated by means of Monte Carlo simulations in collaboration with N. Medvedev, University of Kaiserslautern [112]. The irradiation by a 10 fs long pulse with photon energy of 92 eV, with a fluence of 0.6 J/cm², was assumed according to experiments presented later in chapter 4.5. The cross-sections for the photo-ionization and electron-interaction are taken from Fig. 4.3, and reference [86].

A time when only 10% of holes in L-shell, created by the initial photo-ionization, remain, is found to be $\tau_c = 60$ fs. This lifetime was considered as a cut-off time for L-shell recombination, since the creation of secondary L-shell holes is negligible.

selection rules may be broken in the presence of strong fields. Further, selection rules are not valid for Auger decays.

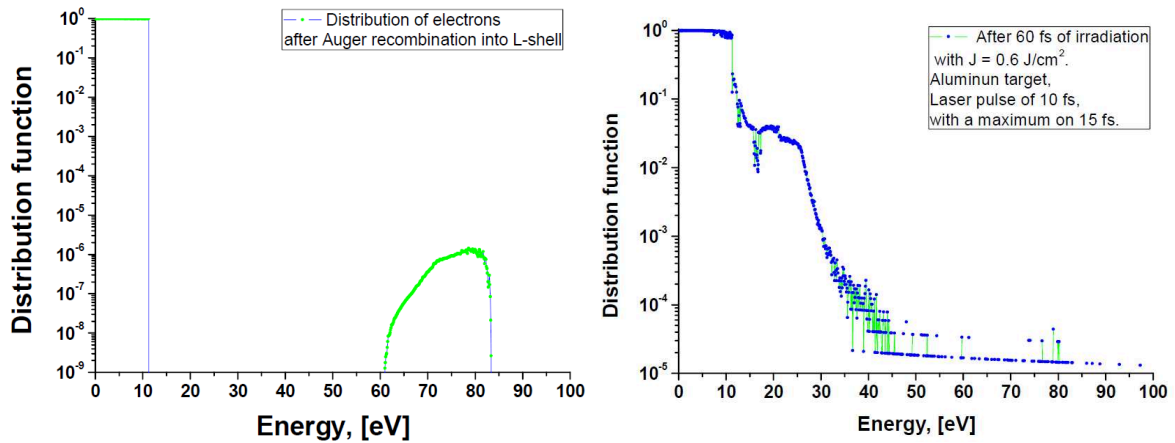


Figure 4.5: Left: Distribution of Auger electrons just after their creation, before their distribution. Right: Distribution of the heated conduction band electrons 45 fs after the peak of a 10 fs FEL pulse [112].

During the Auger process, each recombination will give the binding energy to another conduction band electron. This generates a separate electron distribution, shown in the left panel of Fig. 4.5. It resembles the shape of the 11.2 eV wide conduction band, shifted by the binding energy of 72.5 eV.

Subsequently, the Auger electrons thermalize with the conduction band and change the shape of the initially sharp Fermi surface, as shown in the right panel in Fig. 4.5 in logarithmic scale. The dominant fraction of the electrons is close to E_F , but still not exactly thermalized. Fitting with a Fermi function yields a temperature of 0.8 eV, if we would like to compare it with the corresponding temperature. There is also a long non-thermalized tail, which is formed by Auger-created electrons and their secondary products.

From the simulations, find that the two groups of electrons (Fermi-like distributed and non-thermalized) are responsible for different quasi-temperatures observable by different methods: The L-shell radiative decay is a gated process which excludes later stages of the plasma evolution, such as complete thermalization, ionization, recombination and hydrodynamic expansion. Hence, we observe the lower electron temperature of the Fermi-like distribution. Other spectroscopic methods such as Bremsstrahlung and ratio of ionic lines (presented in chapter 4.4), integrate the plasma emission over long timescales.

4.3 Principles of XUV spectrometers

4.3.1 Challenges using XUV radiation

The application of XUV radiation (1 nm - 50 nm) in combination with intense XUV sources strengthens the need for efficient plasma spectroscopy, but this wavelength regime poses several technical challenges.

Vacuum requirements

Unlike in the visible or x-ray regime, any application of XUV radiation requires high vacuum conditions, i.e. $p < 10^{-5}$ mbar. Firstly, XUV photons are strongly absorbed by thin films or even residual atmosphere. Secondly, the photons carry sufficient energy to trigger chemical reactions with residual gases (such as hydrocarbons) which lead to a degeneration of irradiated surfaces of mirrors, gratings, filters and detectors.

Diffraction elements

The design of diffractive elements is in general restricted to the use of gratings. Prisms, most commonly used in the optical regime, show strong absorption along with weak dispersion. Crystals as Bragg-diffraction elements, which cover the whole x-ray range with excellent resolution, are only applicable at $\lambda < 6$ nm, since $\lambda < 2d$ has to be fulfilled according to Bragg's law. Here d is the lattice spacing, which is the largest for organic crystals (mostly phthalates⁵ or OHM⁶ [113]). These crystals show a high degree of imperfection and fragility. RAP for instance is hygroscopic and tends to degenerate within days when exposed to air.

Transmission gratings have to be free-standing, i.e. not supported by a stabilizing foil. In general, the sub-micron grating bars are supported by a larger underlying grid instead, which can result in distortion of the spectral image and is discussed in chapter 4.3.2. Spectra from reflection grating do not suffer from these distortions.

XUV optics

Reflection of broadband XUV radiation for both collection mirrors and reflection gratings can only be achieved when grazing incidence (i.e. small angle to the surface) at super-polished surfaces is maintained. This is easily understood when recalling from Snell's

⁵potassium acid phthalate (KAP), rubidium acid phthalate (RAP).

⁶octadecyl hydrogen maleate.

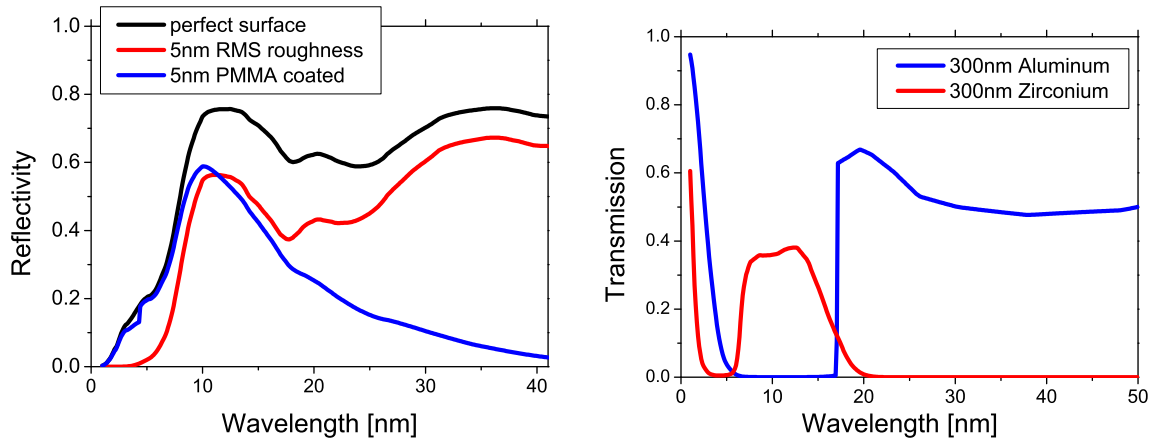


Figure 4.6: LEFT: Reflectivity of a grazing incidence platinum-coated mirror (7.5° to the surface). Three conditions are shown: First, a perfect surface, second, a surface with 5 nm RMS roughness, and third a perfect surface, but covered with 5 nm hydrocarbons (PMMA). RIGHT: Transmission of 300 nm-thin filter foils made of aluminum and zirconium, respectively [86].

law that the critical angle for total external reflection (to the surface) is given by $\Theta_c = 90^\circ - \arcsin \tilde{n}$, with \tilde{n} the complex refractive index:

$$\tilde{n} \equiv n + ik = 1 - \delta + i\beta \quad , \quad \text{with} \quad 1 - \delta \leq 1.$$

Here, β represents the imaginary part which leads to absorption. In the XUV range, angles $< 10^\circ$ to the surface can practically be used, but reflectivity will be already reduced at short wavelengths around 5 nm. This in turn limits the collection solid angle. Due to the grazing incidence, both surface contamination and surface roughness immediately decrease the optics throughput, see Fig. 4.6. Therefore the coating of these optics is done with durable inert elements such as nickel, silver, gold or platinum. In ultra-high vacuum, i.e. inside an accelerator facility, also carbon-coated mirrors are used.

Filters

Material for filters to distinguish between XUV photons and visible light are a few 100 nm-thin free-standing foils from materials with absorption edges at lower wavelengths than the ones of interest. Further, metal foils are more suitable because they are light-tight⁷, compared to membranes made from boron, silicon nitride or PMMA⁸.

⁷the LEBOW company provides light-tight filters that consist of two 200 nm thin metal foils stucked to each other, in order to avoid arbitrary micro-pinholes.

⁸PMMA contains only the light elements carbon and hydrogen.

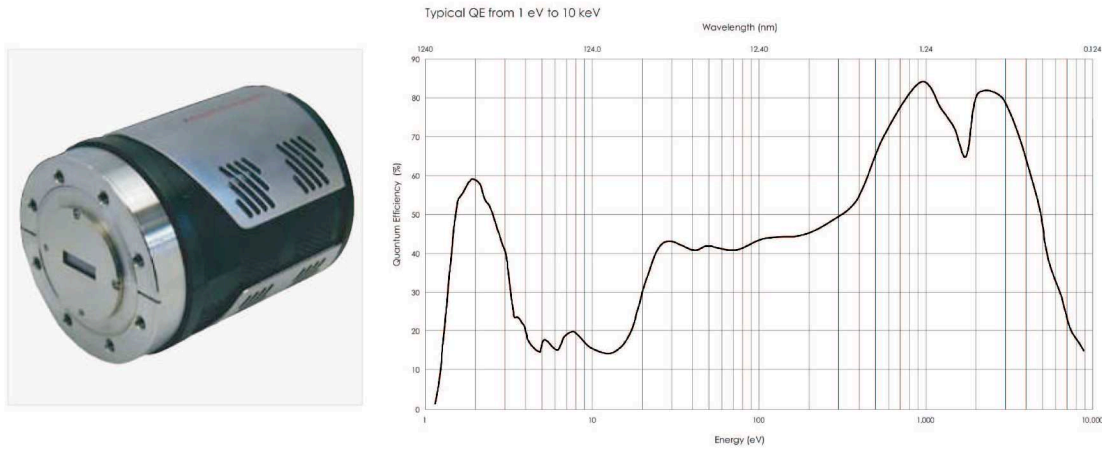


Figure 4.7: Photograph and quantum efficiency of the PIXIS CCD (Princeton Instruments) used by the author, having a 1024×512 $13.5 \mu\text{m}$ -pixel array. Information supplied by the vendor.

Materials which are fragile and oxidize easily, such as magnesium, should be avoided. Aluminum and zirconium foils are widely used. Their transmission is shown in Fig. 4.6.

Detectors

As detectors, back-thinned and back-illuminated CCDs are available with XUV quantum efficiencies around 50% and pixel sizes down to $13.5 \mu\text{m}$. An example is the device shown in Fig. 4.7 which was used by the author. In this plot, the quantum efficiency (QE), which is defined as the percentage of photons hitting the CCD chip that will produce an electron-hole pair, is shown for a large spectral range. Note that the QE for photon energies of $30 - 300 \text{ eV}$ ($4 - 40 \text{ nm}$ wavelength) investigated in this thesis is $40 - 50 \%$ and rather flat. The silicon chip is directly exposed to the vacuum without a protection layer. It applies an air-cooled Peltier-element to decrease the chip temperature down to -60°C , reducing thermal noise. High vacuum has to be maintained to prevent freezing of residual gases onto the CCD chip, because it leads to strong absorption. Cleaning of the chip is not straightforward due to the absent protection layer. Alternatives to the use of CCD cameras are XUV-sensitive films or image plates, while the latter have a rather bad spatial resolution. Both have to be protected against visible light, and the vacuum has to be broken each time the detector is read out. Therefore and because of the time-consuming read-out process, the use of CCDs is a clear advantage. The use of MCPs or phosphor screens is beyond the scope of this overview.

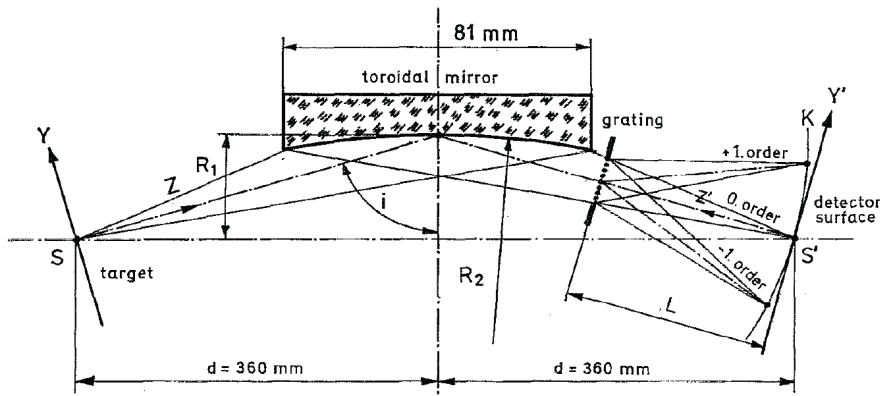


Figure 4.8: Schematic of the transmission grating spectrograph with the toroidal mirror [114].

4.3.2 Focusing transmission-grating spectrograph after Jasny et al.

At the beginning of user experiments at the FLASH facility in 2006, a spectrometer designed by a group conducted by J. Jasny⁹ [114] in 1994 was at the authors disposal. The instrument was developed earlier for spectroscopy of laser-produced plasmas. The experiment described in chapter 4.4 was performed using this device, and the experiences with it lead to the design of an improved spectrometer (see chapter 4.3.3).

Specifications

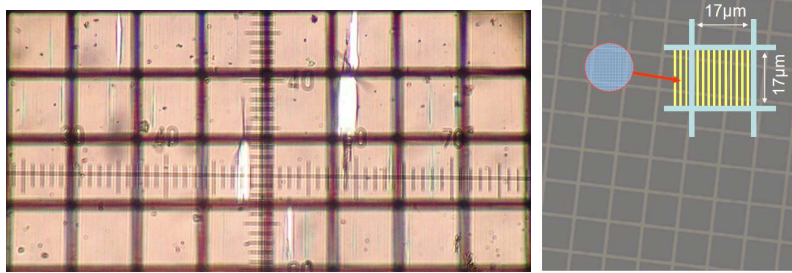
A complete schematic of the spectrograph is shown in Fig. 4.8. The XUV emission from a laser-produced plasma, which has a typical spot size of the order of $20 \mu\text{m}$, is collected by a toroidal mirror and 1:1-imaged through the grating onto the flat detector surface. Due to the small size of the object (i.e., the plasma), no entrance slit or pinhole is necessary. Hence, ideal imaging may be performed with the equatorial zone of a rotary ellipsoid. A very good approximation of such an equatorial zone is a long stretched toroidal surface that can be fabricated much more easily. The toroidal mirror images the point S into S' . The radii of the mirror are $R_1 = 24 \text{ mm}$ and $R_2 = 5375 \text{ mm}$. The physical size of the mirror is $20 \times 100 \text{ mm}$ but only 81 mm of the total length is optically used. The mirror is coated with Nickel which has a refractive index smaller than 0.9977 for wavelengths larger than 1.8 nm . For this value of the refractive index, the angle of total external reflection (to the surface normal) is 86.14° .

A transmission grating with 1000 or 2000 lines/mm consists of free-standing gold bars¹⁰ as shown in Fig. 4.9. The bars are intersected by a square support grid of $17 \mu\text{m}$ period. The frame of the transmission grating acts as a rectangular aperture with an opening of $\sim 5 \times 10 \text{ mm}$. The full solid angle of acceptance is $\Omega = 5.9 \times 10^{-4} \text{ sr}$. The

⁹Max-Planck Institute for biophysical Chemistry, Göttingen, Germany.

¹⁰supplied by X-Opt, Gainesville/ Florida, USA.

Figure 4.9: Microscopic image of the 2000 lines/mm transmission grating with a square support grid of $17\ \mu\text{m}$ period and the grating bars within. Due to frequent venting and pumping of the attached vacuum chamber, the grating suffered by means of destroyed grating bars.



distance $L = 266\ \text{mm}$ between the grating and the detector is chosen to get the desired spectral range up to $19\ \text{nm}$ in the $+l^{\text{st}}$ and $-l^{\text{st}}$ order. The zeroth order is imaged in the middle of the detector, this is point S' in Fig. 4.8. It can be blocked by an adjustable beam stop in front of the detector to prevent saturation. The rays transmitting the grating are convergent resulting in the spectral image K being slightly curved. The sagitta of the curved image is $2.2\ \text{mm}$ leading to an additional defocussing on the flat detector.

The mirror, grating, and detector are rigidly fixed to each other in a common housing, which is mounted by means of a ball joint and vacuum bellows to a CF 160 vacuum flange. A special mechanical mounting with three micrometer screws allows the spectrometer to be adjusted in the x , y , and z directions. The coarse alignment of the spectrograph was performed with a pointer, and the fine adjustment was optimized for the best sharpness of the image of the unblocked zeroth order and of all spectral lines.

Performance

The spectrometer was tested and spectrally calibrated using characteristic soft x-rays. Therefore, metal samples were exposed to an electron beam with beam current up to $10\ \text{mA}$ in a vacuum chamber. The electron gun consists of the tungsten filament from a halogen light bulb, where the glass had been removed. It is surrounded by a focusing cylinder at small negative potential, while the tungsten filament itself is held at zero potential. The emitted electrons are accelerated towards the aluminum or magnesium anode, which is at $\leq 4\ \text{kV}$ positive potential. Due to electron impact, holes are created in the sample, which recombine either by Auger or radiative decay. The position of emission lines from the latter process is found with suitable accuracy in the literature [86, 115]. To define a small source point for the toroidal mirror, a $25\ \mu\text{m}$ wide slit was used, and an aluminum filter suppressed all visible light. As a demonstration, Fig. 4.10 shows

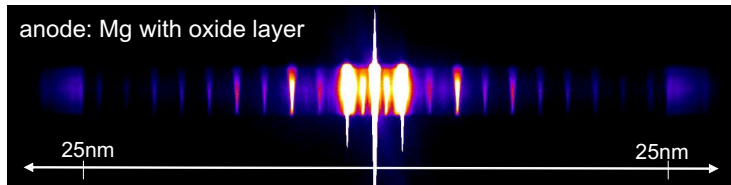


Figure 4.10: XUV spectrum of a Mg anode exposed to 4 keV electrons. The grating diffracts mainly O-K $_{\alpha}$, including higher orders, and Mg L-shell fluorescence at $\lambda > 25$ nm.

an emission spectrum of magnesium with an oxide layer¹¹. Dominantly, we observe the broad fluorescence radiation from magnesium at $\lambda > 25$ nm, as well as odd orders of the oxygen K $_{\alpha}$ line (2.36 nm). The even diffraction orders are visible, but highly suppressed. During the experiments, a resolution of 0.1 nm at the aluminum absorption L-edge located at 17 nm was achieved.

Drawbacks

The results obtained with the Jasny-spectrometer (see chapter 4.4) were encouraging, but nevertheless we notified several drawbacks.

First, the transmission grating is fragile and suffers from any pumping and venting process, as illustrated by the microscope image in Fig. 4.9. The bars are supported by a larger underlying support grid. While the period of the grating bars is $d_b = 1 \mu\text{m}$, the period of the support grid is $d_g = 17 \mu\text{m}$. Following the grating equation,

$$d \times \sin \Theta_m = m\lambda$$

where Θ_m is the diffraction angle and $m = 0, 1, 3, 5, \dots$ ¹² is the diffraction order, the support grid diffracts also XUV light, but with less dispersion.

The grating consists of two structures with different lattice spacing, and acts like the multiplication of two amplitude structures to a monochromatic planar wave. Since the distance between grating and detector z is large compared to d^2/λ , the electric field amplitudes in the detector plane resemble the Fourier transform of the amplitude transmission grating, the point-wise multiplication of two grating structures equals the convolution of both on the detector. The intensity measured by the detector is proportional to the square of these amplitudes. If a monochromatic source is imaged using such a transmission grating, each order of the fine grating shows fast oscillations in its pedestal which is the convoluted diffraction pattern from the support grid. While for broad spectral distribution this might be adequate, spectroscopy of fine emission lines or even observation of scattered coherent, monochromatic radiation will result in 'ghost'

¹¹Magnesium tends to oxidize rapidly at the sample surface when exposed to air.

¹²In case of equal dimension of grating bars and slits, even diffraction orders are suppressed.

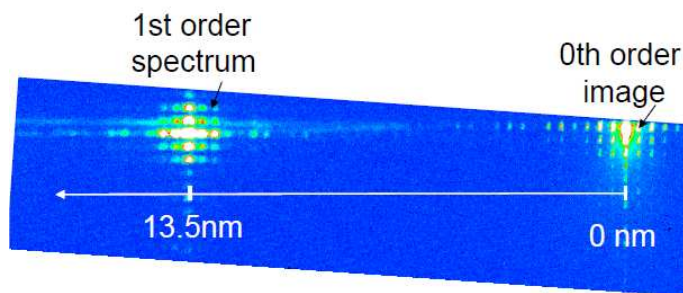


Figure 4.11: Scattering of 13.5 nm FEL pulses from the tip of a steel needle, observed through a transmission grating with 1D grating bars and 2D support grid.

peaks surrounding the original signal as shown in Fig. 4.11.

Second, the spectrum is spread symmetrically to both $\pm 1^{\text{st}}$ orders with 10% efficiency, compared to the incoming ray. The spectral range can only be increased when the detector is not placed symmetrically to the beam-path. Further, this spectrum is only focused for one wavelength simultaneously. Practically, one has to optimize the focal distance of the spectrometer for a certain wavelength region. Other spectral ranges will lose spectral resolution.

4.3.3 HiTRaX - a focusing reflection-grating spectrometer

To further improve XUV plasma spectroscopy and avoid the disadvantages described above, we aimed to construct a most versatile instrument by making it compact, allowing all adjustments to be made in vacuum (e.g. filter change, grating rotation) and thus easy to operate. Any currently commercial XUV spectrometer would not fit to our experimental needs because of their high weight and inflexible design. Great help came from our design engineer and the workshop for fine mechanics at our institute. In this chapter I present the successful technical realization of our design goals as well as the calibration of the **H**igh **T**hroughput, **H**igh **R**esolution Spectrograph for soft **X**-ray light (HiTRaX) which has been applied in various experiments [14, 116].

Design

HiTRaX utilizes customized optics from Horiba ScientificTM. The platinum coated optics consist of a toroidal mirror and a variable line space (VLS) holographic grating with an average line density of 800 lines/mm. Both optics have an active optical surface area of $50 \times 20 \text{ mm}^2$. The mirror images the source onto a Princeton Instruments PIXIS-XO: 2KBTM back thinned CCD with a magnification of 1. The grating in between CCD and mirror disperses the image spectrally using VLS to focus further along the dispersion direction improving spectral resolution and producing a flat focal plane. To obtain high

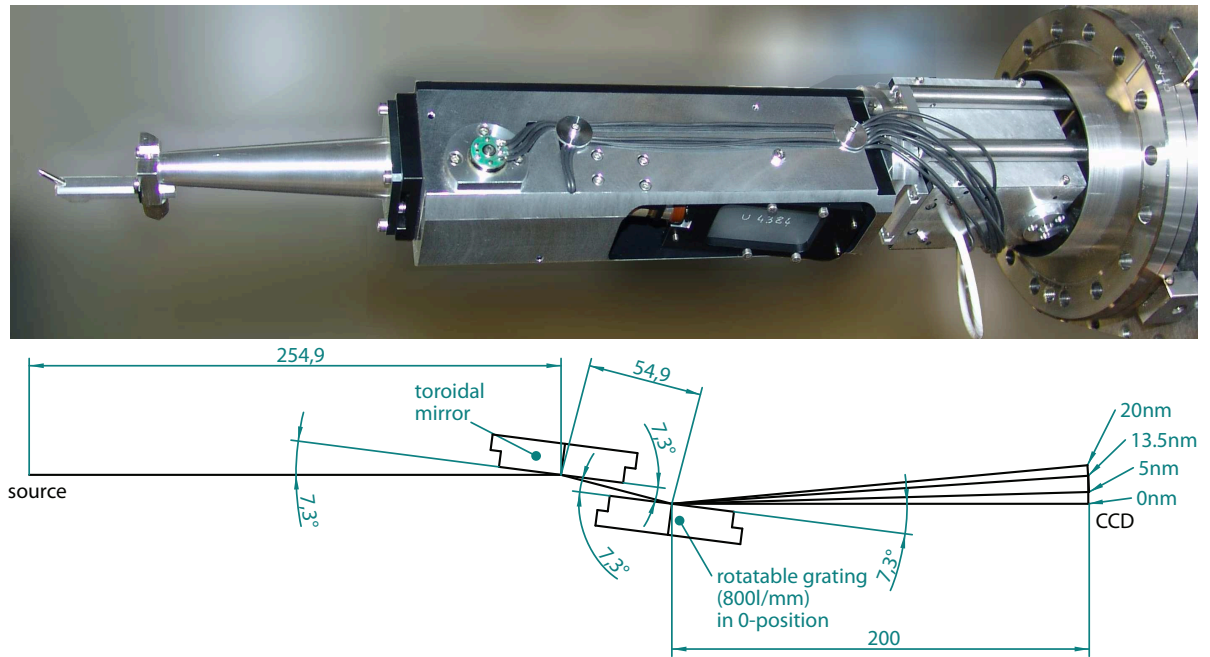


Figure 4.12: Photograph and Geometry of the optics utilized in HiTRaX. Measurements are in mm or degrees.

reflectivity even with soft X-ray light the optics are placed at grazing incidence geometry (78% at 7.3 degree for the mirror [86]). The distance between mirror and source is 255 mm resulting in a solid collection angle of 1.9×10^{-3} sr. Beside a photograph, Fig. 4.12 shows the distances and angles of the optical components in the setup.

In addition, HiTRaX features a motorized shutter to protect the optics from debris when not in use, motorized grating rotation with ± 3 degree range of motion and a motorized filter wheel containing up to five filters (Fig. 4.13). The filters help to suppress visible light to which the CCD is also sensitive, as well as certain ranges in the soft x-ray spectrum depending on the filter material. The most used filters are 200 nm thick zirconium and aluminum (details in Fig. 4.6). The dimensions of the filters (28 mm \times 6 mm) and the position of their frame in the beam path are chosen such that they do not obstruct soft x-rays from the source but absorb most visible and stray light. The filter wheel is located between the grating and the CCD, away from the source, to protect fragile filter foils from debris that is common in laser plasma experiments. The filter wheel is surrounded by sufficient open space to minimize the pressure on the foils by air streams during evacuation and venting of the apparatus. The components facing the optical path have been anodized and dyed black to minimize stray light. Three apertures shaped and adjusted to the optics outer dimensions also reduce stray light. The optics

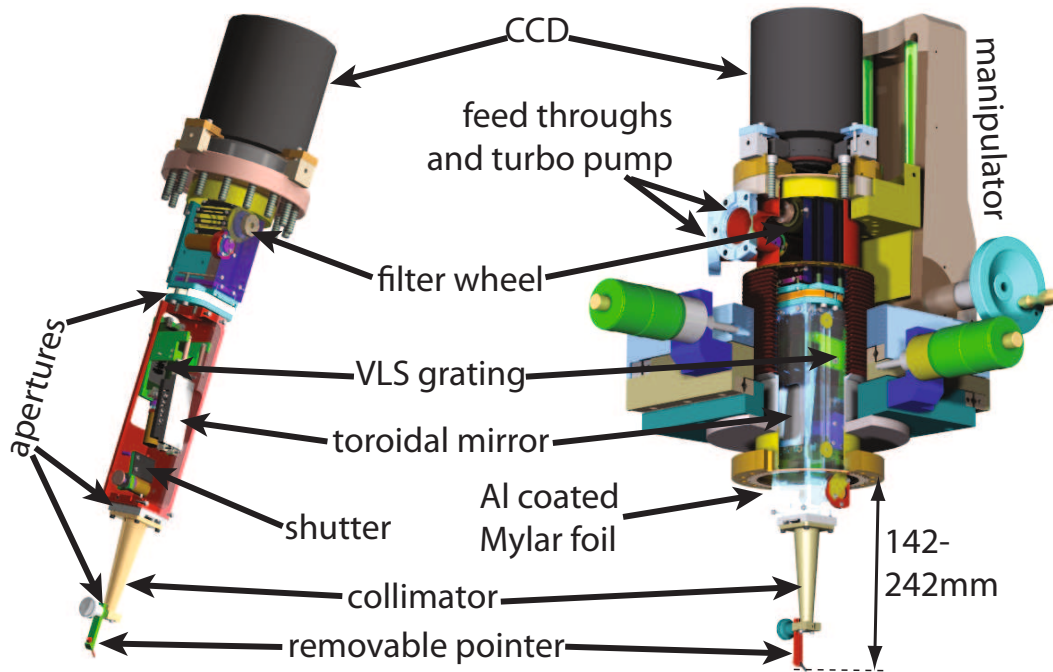


Figure 4.13: Overview of HiTRaX components.

housing is built from aluminum to reduce weight to a minimum.

The whole spectrograph was built compactly enough to be completely embedded in a DN 100 CF ultra high vacuum XYZ-manipulator with dimensions $43 \times 46 \times 47 \text{ cm}^3$. With that, the instrument can be aligned within $\pm 5 \text{ mm}$ parallel and $\pm 50 \text{ mm}$ perpendicular to the DN 100 CF base flange. These degrees of freedom as well as a removable tip pointing to the source location reduce alignment time to the source significantly. They allow the spectrograph to adapt to possibly changing source locations without having to break vacuum. A flexible $20 \mu\text{m}$ thin Mylar foil coated on both sides with 250 nm of Al bridges the gap between the spectrometer and the opening of the DN 100 CF manipulator to prevent stray light from reaching the CCD while maintaining the full range of motion (Fig. 4.13). The foil further separates the plasma vacuum chamber from the spectrograph interior, which is differentially pumped by means of a small turbo pump. Thus, the interior reaches an estimated pressure of 10^{-6} mbar . This prevents the CCD chip, cooled to -60°C , from residual gas freeze-out. The CCD itself is held in place using clamps allowing it to be rotated and shifted parallel to the flat flange surface while the instrument is not evacuated, thereby aligning it to the dispersion direction. This way, also the filter wheel can be accessed quickly without removing the device from the vacuum chamber, hence not losing both time and alignment.

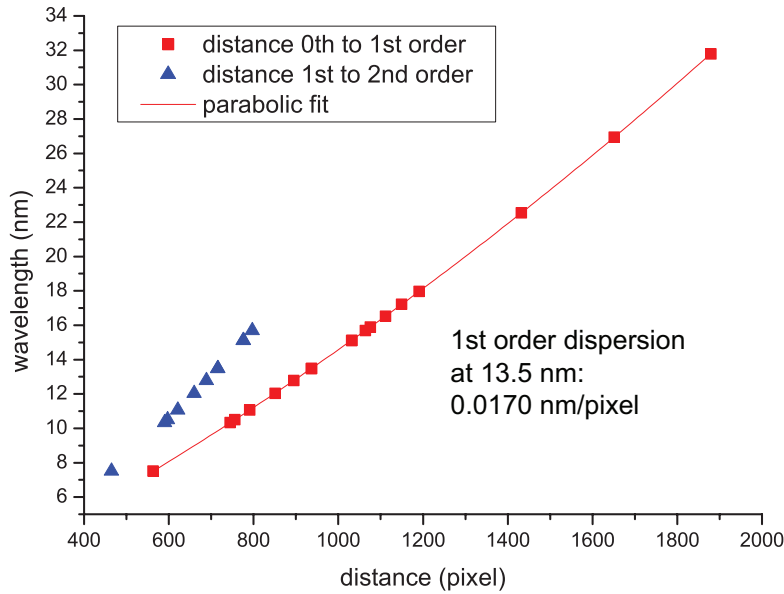


Figure 4.14: Calibration of the dispersion at the synchrotron DORIS beam line BW3.

Dispersion

The dispersion was calibrated using radiation from the DORIS (DESY) synchrotron beam line BW3 [117, 118, 119]. The monochromator of this beam line delivers radiation with a typical resolution of $\lambda/\Delta\lambda \cong 10^4$ and 10^{12} photons per second. The radiation is cropped by a pinhole of $5 \mu\text{m}$ diameter at the source location of the spectrometer to reduce intensity and produce a small image on the CCD. The spectrograph is evacuated to 10^{-6} mbar. Figure 4.14 shows the measured pixel distance from 0th to 1st and 1st to 2nd order on the CCD for different wavelength settings of the beam line monochromator.

Due to the geometry of the setup the dispersion curve can be fitted and interpolated with a parabola. Thus, radiation in the 1st order and at a distance x in pixels from the 0th order corresponds to a wavelength λ with

$$\frac{\lambda}{\text{nm}} = 2.60 \times 10^{-6} \left(\frac{x}{\text{pixel}} \right)^2 + 1.211 \times 10^{-2} \frac{x}{\text{pixel}} - 0.137.$$

This corresponds to a dispersion of 0.0170 nm/pixel at $\lambda = 13.5$ nm. The dispersion varies about 2% depending on source position and grating angle. The above measurement was conducted with the CCD located in the center of the flange and the 0th order light focusing onto the 125th pixel counted from the edge of the CCD.

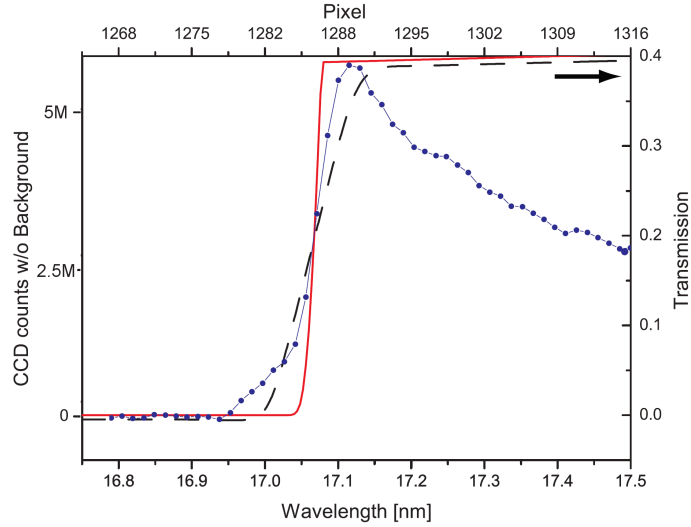


Figure 4.15: The upper graph shows the recorded aluminum L-edge transmission spectrum (dotted blue line) compared to the literature values for transmission (red line) [86] and the convolution of 0^{th} order with the literature L-edge (black dashed).

Resolution

A resolution test was conducted utilizing a soft X-ray tube setup already mentioned in chapter 4.3.2. As a source point emitting diverging radiation, a $25\ \mu\text{m}$ pinhole was placed $\sim 10\ \text{mm}$ from the emitting anode.

In order to determine the resolution of the spectrograph, the Al absorption L-edge at $17.05\ \text{nm}$ [86] was used to superimpose a spectrally sharp feature onto a bremsstrahlung dominated source spectrum. For that, a $0.6\ \mu\text{m}$ Al-foil has been introduced into the beam path between the $25\ \mu\text{m}$ pinhole and the spectrograph. A $0.2\ \mu\text{m}$ Zr-filter inside the spectrograph has been used to block visible light. The spectra have been divided by its transmission function [86]. Furthermore, a background image, i.e. another exposure with equal duration but without acceleration voltage, has been subtracted from the measurements. Figure 4.15 depicts the resulting spectrum for a 30 min exposure with an electron acceleration voltage of $U_{acc} = 4\ \text{kV}$ and a current of $I_{acc} = 5\ \text{mA}$, as well as the Al transmission function.

The edge is recorded half width from its peak down to the middle between noise and peak (HWHM) contains 3.2 pixel which correspond to $0.047\ \text{nm}$ or a FWHM of $0.094\ \text{nm}$. In addition, the L-edge naturally has a finite HWHM of $0.023\ \text{nm}$ at room temperature [86]. Therefore, the FWHM of a monochromatic source would be $0.071\ \text{nm}$ at $17.05\ \text{nm}$. Consequently, the resolution is 240 at $17.05\ \text{nm}$. Assuming no change in the imaging quality of the optics one obtains a resolution of 190 at $13.5\ \text{nm}$. The main error in this measurement arises from vibrations of the pinhole during the 30 min exposure and can be estimated to be $\pm 0.02\ \text{nm}$ in the FWHM which corresponds to a vibration

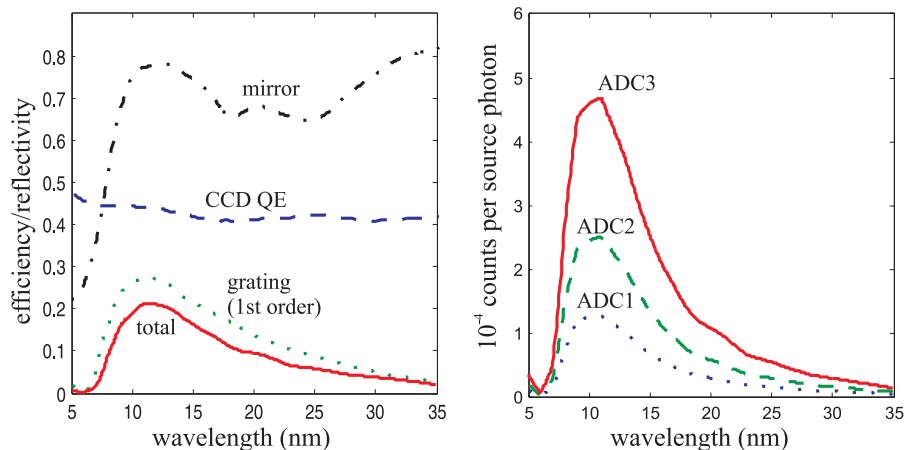


Figure 4.16: The efficiency of the HiTRaX components and their product (left), and the ratio of counts to isotropically emitted source photons (right).

amplitude of $1.4 \mu\text{m}$. In fact, the optics are specified to resolve 0.05 nm at 13.5 nm .

It is also noteworthy that the convolution of the 0^{th} order with the transmission function of the Al foil (Fig. 4.15) shows a FWHM of 0.12 nm - broader than the resolution seen in the 1^{st} order. This can be accounted to the ability of the VLS grating to focus along the dispersion direction and for orders other than the 0^{th} .

Efficiency

The wavelength-dependent efficiency of the HiTRaX components is shown in Fig. 4.16 according to their specifications. By multiplying with the wavelength and detector specific photon-to-count conversion $c(\lambda)$, we obtain the ratio of counts on the detector to isotropically emitted photons. For a typical silicon CCD detector with band gap $\varepsilon = 3.65 \text{ eV}$

$$c(\lambda) = \frac{hc}{\varepsilon\lambda} \times QE(\lambda) \times ADC(\lambda)$$

with the quantum efficiency $QE(\lambda)$, and the electron-hole-pair to count conversion $ADC(\lambda)$. The quantum efficiency and the resulting count-to-source photon ratio for different analog to digital converter ADC settings of the employed Princeton Instruments PIXIS-XO: 2KBTM are also depicted in Fig. 4.16. ADC1, ADC2 and ADC3 correspond to ADC amplifications at the 2 MHz low noise output where on average 3.56, 1.84, and one electron(s) respectively produce(s) one count. With that the expected signal in terms of counts on the CCD can be calculated from a given number of source photons. A minimum amount of photons from the source is necessary to detect a signal. This detection threshold is determined by the signal-to-noise ratio (S/N) of counts on the CCD. The rms noise on the CCD without illumination is 4.5 counts measured in a

Spectrograph	Acceptance Solid Angle (sr)	Throughput
Pinhole ($100\ \mu\text{m}$) camera with 1500 lines/mm grating [120], image distance 20 cm, and no magnification	2.0×10^{-7}	1.6×10^{-9}
Imaging toroidal mirror and transmission grating [114]	4.1×10^{-4}	2.6×10^{-6}
Non-imaging 1200 lines/mm VLS reflection grating [121, 122]	1.2×10^{-3}	9.6×10^{-6}
HiTRaX (imaging toroidal mirror and VLS reflection grating)	1.9×10^{-3}	1.6×10^{-5}

Table 4.1: Comparing different spectrographs for acceptance solid angle and throughput at 13.5 nm wavelength.

box of 50×200 pixel in the center of the CCD cooled to 200 K and along its major axis. Thus, the detection threshold for a $S/N = 5$ is overcome with 2.5×10^5 photons emitted isotropically from a source smaller than pixel size of the detector ($13.5 \times 13.5\ \mu\text{m}^2$). For larger source sizes and non-imaging spectrographs the number of pixels over which the photons are spread needs to be taken into account. After the experiment, Fig. 4.16 can be applied to determine the number of photons emitted from the source into 4π solid angle and at a specific wavelength range. For example, this can be used to determine the free electron density in a plasma via the intensity of bremsstrahlung emission, as described in [13] and chapter 4.4.

4.3.4 Comparing different spectrometer designs

When looking for a spectrograph or similar instrument that produces the highest possible signal for the same measured event then a reasonable figure of merit is composed of the acceptance angle and the efficiency of the components. Here, we use the throughput $t(\lambda)$, defined by the wavelength-dependent ratio of photons, delivered to the detector, to isotropically emitted source photons. Table 4.1 compares this value for various types of spectrographs at $\lambda = 13.5$ nm.

As discussed before, the most obvious advantage of using a reflection grating instead of a transmission grating is the absence of 'ghost'-peaks (Fig. 4.11). Further, a reflection grating diffracts only a single first-order onto the detector, which contains twice as

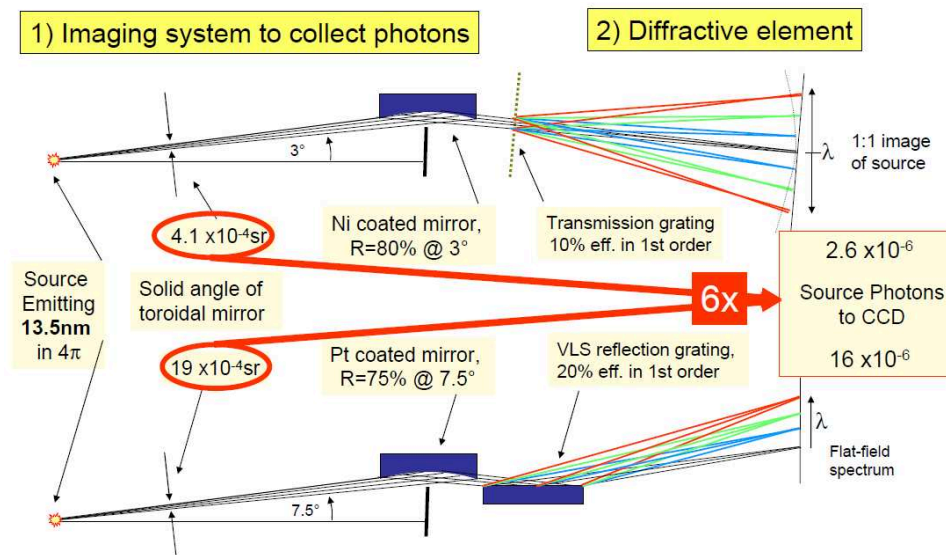


Figure 4.17: The principles of focusing XUV spectrometers. (TOP) schematic of the transmission grating spectrometer after Jasny *et al.* (BOTTOM) schematic of the reflection grating spectrometer HiTRaX.

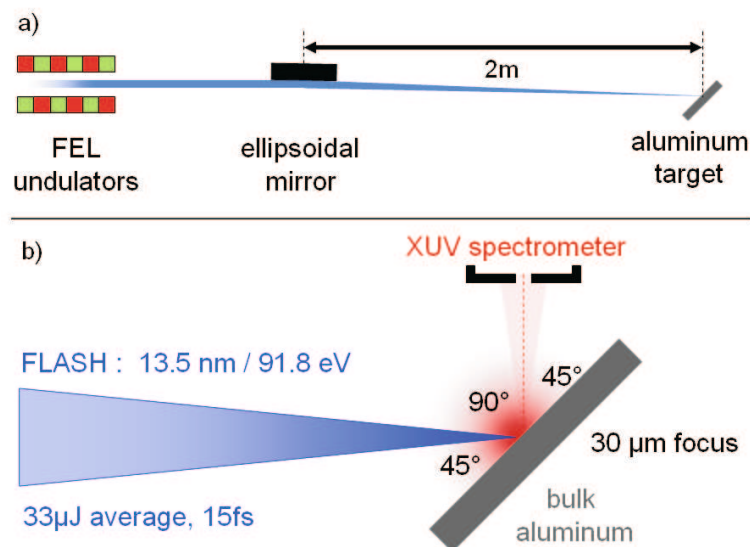
much photons compared to the symmetrical spectra generated by a transmission grating. Hence, the efficiency is little less than twice the efficiency of the transmission grating (10%) due to the reflectivity of the grating surface (Fig. 4.12). Thus, in certain spectral ranges the S/N can be improved by nearly a factor of two when a reflection grating is chosen.

Using a variable-line-spacing (VLS) reflection grating, the lines and curvature of such grating are adapted in order to focus all wavelengths onto the detector plane. This is called *flat-field* and allows sharp recording of spectra over the full spectral range of the spectrometer with constant resolution $\Delta\lambda$.

The grazing angle of the toroidal Ni-coated mirror in the *Jasny*-spectrometer is 3° (to the surface), which results in $R = 80\%$ reflectivity at 13.5 nm [86] and a solid angle of $\Omega = 4.1 \times 10^{-4}$ sr (Fig. 4.17). When the grazing angle is increased to 7.5° and Pt is chosen for the coating, the reflectivity drops to 75%, but the solid angle increases by a factor of 4.6. Together with the reflectivity of the mirror and the efficiency of a reflection grating, such a system gains a factor of $6\times$, as illustrated in Fig. 4.12.

The *Jasny*-spectrometer was uncomfortable regarding changing of filters. For coarse alignment, easiest is using the spectrometer without any filter and focus the source to the CCD detector by illuminating it with a laser pointer or similar. Then, a filter must be introduced to prevent optical light reaching the CCD. Thus, a motorized filter wheel which allows the use of several filters and a beam block without breaking the vacuum are of great help.

Figure 4.18: Experimental setup. a) The XUV pulses from the FEL undulators are focused by an elliptical beamline mirror on the bulk aluminum target, creating a $30\ \mu\text{m}$ focus. b) The target is hit under 45° and plasma is created. A high-resolution XUV spectrometer observes the plasma emission under 45° to the surface normal [13].



Finally, the mechanical adjustment by means of micrometer screws was realized as a rotation with respect to the ball joint of the *Jasny*-spectrometer, rather than sliding along the three spatial axes independently. Therefore, after changes on x and y , an adjustment of the z coordinate was necessary. The new *HiTRaX*-spectrometer is housed in a custom vacuum manipulator with membrane bellows and three independent linear axes of movement.

4.4 Bremsstrahlung and line spectroscopy

In this chapter, an experiment is described where we demonstrate that XUV FELs open a new and promising possibility to heat matter volumetrically and homogeneously. In detail, we show that XUV bremsstrahlung and line spectroscopy allow the determination of the plasma temperature and free electron density. This work was published in *Physical Review E* in December 2008 [13].

4.4.1 Experimental setup

Free-electron laser characteristics

In this experiment, we used FLASH facility (see 4.1.1), delivering pulses of $91.8\ \text{eV}$ photon energy (wavelength $\lambda = 13.5\ \text{nm}$) and $(15 \pm 5)\ \text{fs}$ duration. These were focused to a $30\ \mu\text{m}$ spot by a carbon-coated ellipsoidal mirror at beamline BL2, with a grating

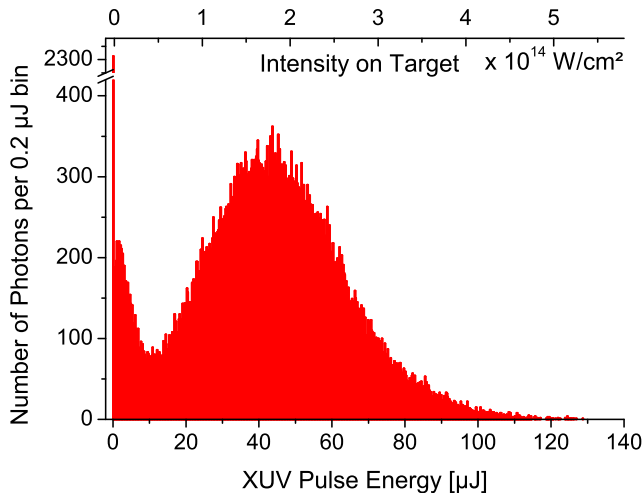


Figure 4.19: Histogram of the energy spread of 13.5 nm XUV pulses generated by Self-Amplified Spontaneous Emission (SASE). Only pulses contributing to the measured spectrum of the performed experiment are shown. The top abscissa shows the corresponding irradiation intensities on target [13].

incidence angle of 3° and 2 m focal length, as shown in Fig 4.18.

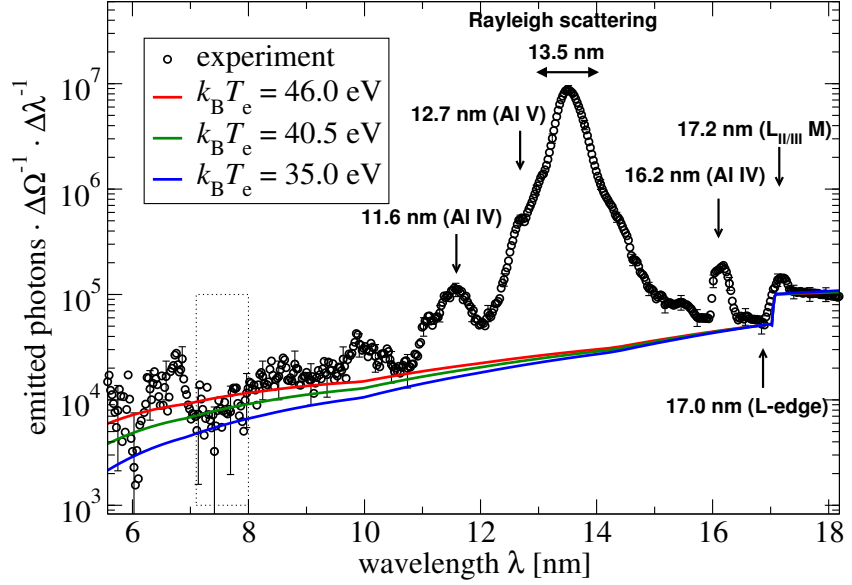
Since the FEL process starts from spontaneous radiation, it shows an intrinsic shot-to-shot pulse energy spread. The relevant distribution of pulse energies for this experiment is shown in Fig. 4.19. The total number of pulses in our measurement was 81,000, including 3% of zero-energy events and a significant fraction of high-energy pulses up to $130 \mu\text{J}$. The mean value is $48 \mu\text{J}$, measured at the end of the undulators. Since the beamline transmission is known to be $T = 0.68$, the average pulse energy at the experiment is $33 \mu\text{J}$.

XUV Plasma Spectroscopy

Each pulse irradiates a bulk aluminum target under 45° incident angle, resulting in an average intensity of $2 \times 10^{14} \text{ W/cm}^2$, see Fig. 4.18. The polarization is linear in the horizontal plane (s-polarized). At the chosen wavelength, the critical density for penetration into the bulk $n_{\text{crit}} = (2\pi c)^2 \epsilon_0 m_e / e^2 \lambda^2 = 6.1 \times 10^{24} \text{ cm}^{-3}$ is about 40 times higher than the valence electron density in cold solid aluminum, $n_e = 1.6 \times 10^{23} \text{ cm}^{-3}$. Therefore the initial absorption length is 40 nm [86]. The pulse energy is deposited in a target volume of $\pi \times (15 \mu\text{m})^2 \times 40 \text{ nm}$, generating WDM. The number of 10^{12} atoms in this volume is in the same order of magnitude as the incident photon number.

At fixed target position, the emission spectrum of about 10^4 exposures was recorded before moving to a fresh site. Since the very first FEL pulse ablates a few-nanometer thin surface layer, further surface cleaning technique was not necessary. The target was at ambient temperature, and vacuum was kept constant at 10^{-7} mbar.

Figure 4.20: Experimental XUV photon spectrum per solid angle $\Delta\Omega=4 \times 10^{-4}\text{sr}$ and wavelength interval $\Delta\lambda=0.025\text{ nm}$ (symbols with error bars) and bremsstrahlung calculations for different electron temperatures. The spectrum is corrected for the spectrometer throughput and the detection efficiency [13].



The FEL was operated in multibunch operation mode at 5 Hz repetition rate, with 20 bunches per train giving 100 FEL pulses per second. Five separate measurements of different durations adding up to a total interaction time of 13.5 min were performed. Since the individual spectra look identical we assume that plasma formation and emission processes vary very slowly during the measurement.

XUV emission spectra in the region of 6 – 18 nm were measured with the transmission grating spectrometer described in chapter 4.3.2. However, the spectral resolution was limited to 0.2 nm due to a slightly fluctuating plasma position. A back-thinned XUV CCD camera with $13 \times 13 \mu\text{m}^2$ pixel size and a quantum efficiency of $\eta = 0.45$ served as detector. From the measured spectra, absolute photon numbers per wavelength interval and solid angle are calculated using the tabulated efficiency of all components.

4.4.2 Data analysis

Figure 4.20 shows the sum of all spectra in logarithmic scale after correction for the spectrometer throughput and detection efficiency. The error-bars arise essentially from statistical signal-to-noise ratios beside uncertainties of the spectrometer components. The main peak at 13.5 nm stems from Rayleigh scattering of FEL photons by bound aluminum electrons. It is broadened symmetrically by $\pm 0.4\text{ nm}$ due to artifacts originating from the support grid of the transmission grating. Spectral lines from Al IV and Al V are identified using the NIST tables [115] as listed in Tab. 4.21. The continuum emission is formed by free-free transitions (bremsstrahlung) and free-bound recomb-

Experimental data [nm]	Reference data [nm]	Relative intensity (NIST)	Oscillator strength f (NIST)	Transition
11.6 ± 0.2	11.646	250	0.332	Al IV: $2s^2 2p^6$ $-2s^2 2p^5 ({}^2p_{1/2}^0) 4d$
12.7 ± 0.2	12.607	800	–	Al V: $2s^2 2p^5$ $-2s^2 2p^4 ({}^1D) 3s$
16.2 ± 0.2	16.169	700	0.247	Al IV: $2s^2 2p^6$ $-2s^2 2p^5 ({}^2p_{1/2}^0) 3s$
17.2 ± 0.2	17.14	-	–	$L_{II/III}M$

Figure 4.21: List of the spectral lines emitted from the plasma, identified with the NIST database [115], and [124].

nation processes. Since the target is heated volumetrically, the continuum emission is partly reabsorbed and we observe a step-like feature at 17.0 nm that is consistent with the absorption $L_{II/III}$ -edge [86]. This indicates deep deposition of energy into the target, as expected for XUV photon-matter interaction. The corresponding absorption L-edge at a similar excitation flux was also analyzed in laser excited silicon [123]. Finally, the Al $L_{II/III}M$ -fluorescence line [124] is observed at 17.2 nm.

Bremsstrahlung

The experimental spectra allow the determination of the plasma parameters using fundamental relations [87]. The electron temperature and density are inferred from the continuum background radiation due to bremsstrahlung. We compare the experimental data to Kramers' law [125]

$$j_{\text{ff}}(\lambda) = \left(\frac{e^2}{4\pi\epsilon_0} \right)^3 n_e^2 \frac{16\pi Z e^{-2\pi\hbar c/\lambda k_B T_e}}{3m_e c^2 \lambda^2 \sqrt{6\pi k_B T_e m_e}} g_T(\lambda) \quad (4.1)$$

for the free-free emissivity $j_{\text{ff}}(\lambda)$. Here, m_e is the electron mass and $g_T(\lambda)$ is the wavelength dependent Gaunt factor [126], accounting for medium and quantum effects. It is calculated in Sommerfeld approximation [127]. We assume an average ion charge of $Z = 4$, which is supported by calculations of the relative ion abundances using the code COMPTRA04 [128], see below. In the wavelength range from 7.1 nm to 8.0 nm (marked by the dotted box in Fig. 4.20), we expect no essential contributions from bound-bound and bound-free transitions. Statistical analysis of the data in this range yields 40.5 eV for the temperature with an rms error of ± 5.5 eV. Bremsstrahlung spectra for 35 eV,

40.5 eV, and 46 eV are shown in Fig. 4.20. Reabsorption was considered using tabulated opacity data [86], in this way the L-edge at 17.0 nm is reproduced. The height of the L-edge corresponds to a transmission through 40 nm of cold aluminum.

Kramers' law (Eqn. 4.1) depends on the square of free electron density n_e . From the absolute photon number at $\lambda = 17.0$ nm, $N_{\text{photon}} = 51424\Delta\Omega^{-1}\Delta\lambda^{-1}$, we calculate the free electron density using Eq. 4.1 as $n_e = 4.0 \times 10^{22} \text{ cm}^{-3}$, taking the inferred plasma temperature of 40.5 eV. This value is consistent with radiation hydrodynamics simulations, see below.

Transition Line Ratio

Independently, the electron temperature can be obtained from the ratio of integrated line intensities I_ν for the identified transition lines from the Boltzmann distribution [129] as follows

$$\frac{I_1}{I_2} = \frac{\omega_1^3 f_1}{\omega_2^3 f_2} e^{-\hbar(\omega_1 - \omega_2)/k_B T_e}, \quad (4.2)$$

with the corresponding photon frequencies ω_ν and oscillator strengths f_ν , having in mind that the plasma is optically thin. Here, the Al IV lines (doublets) at $\lambda_1 = 16.169$ nm and $\lambda_2 = 11.646$ nm, with oscillator strengths given in Tab. 4.21, are used. Integration was performed from 15.9 nm to 16.3 nm and from 10.8 nm to 11.9 nm after subtraction of the bremsstrahlung continuum, respectively. The resulting temperature is (34 ± 6) eV. Within the error bounds, this is consistent with the temperature inferred by analysis of the bremsstrahlung continuum, so that we can state the plasma temperature with about 38 eV.

A full compliance of line and continuum temperature cannot be expected, since the plasma dynamics affects both emission processes in different ways. At early times after the laser-target interaction, the system is still very dense and the excited levels of the transitions under consideration are possibly dissolved into the continuum. Only after expansion, the excited levels are well defined and radiative transitions take place. Bremsstrahlung, on the other hand, is most relevant at early times due to the n_e^2 -dependence of its emissivity, see Eq. 4.1. Thus, in the bremsstrahlung emission we expect a higher temperature than in the line spectrum.

Relative Ion Abundance

The relative abundance of aluminum ions was calculated with the code COMPTRA04 [128]. Results for electron temperatures from 10 eV to 50 eV are shown in Fig. 4.22,

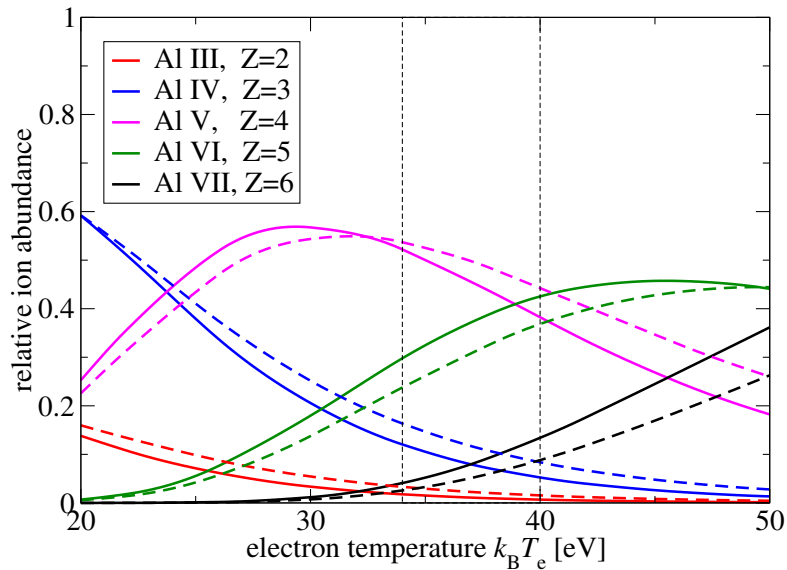


Figure 4.22: Calculation of the relative Al ion species abundance from COMPTRA04 as a function of the electron temperature. Solid line is for Al density $\rho_{\text{sol}} = 2.7 \text{ g/cm}^3$, dashed line $0.5 \rho_{\text{sol}} = 1.35 \text{ g/cm}^3$ [13].

assuming solid density $\rho_{\text{sol}} = 2.7 \text{ g/cm}^3$ and $0.5 \rho_{\text{sol}}$, i.e. slightly expanded. The concentration of ion species for the relevant temperatures between 34 and 40 eV complies with the observed line emission spectrum. At an averaged temperature of 38 eV, the ion fractions of Al IV, Al V, and Al VI take the values of about 7%, 45%, and 46%, respectively. Amounts of Al I-III as well as Al VII and higher are negligible.

All expected spectral lines from Al IV in the observed spectral range are either observed (at 16.2 nm) or covered by the strong FEL signal (at 12.9 nm). For transition details see Tab. 4.21. Weak lines from Al V between 11.9–13.2 nm overlap with the Rayleigh peak and only the 12.607 nm line can be identified. Transition lines from Al VI, which are located between 8.6–10.9 nm, are not significantly present compared to the detector noise. This indicates, that the corresponding high-lying excited levels are dissolved and do not contribute.

Emission lines from Al VII (and higher) are expected to play a significant role only at temperatures exceeding 40 eV, as shown in Fig. 4.22. These lines have also not been found, but have previously been observed in optical laser-matter interaction experiments [130]. This contrast is well understood by scrutinizing the different mechanisms of absorption and ionization in the case of optical light as opposed to the case of XUV photons.

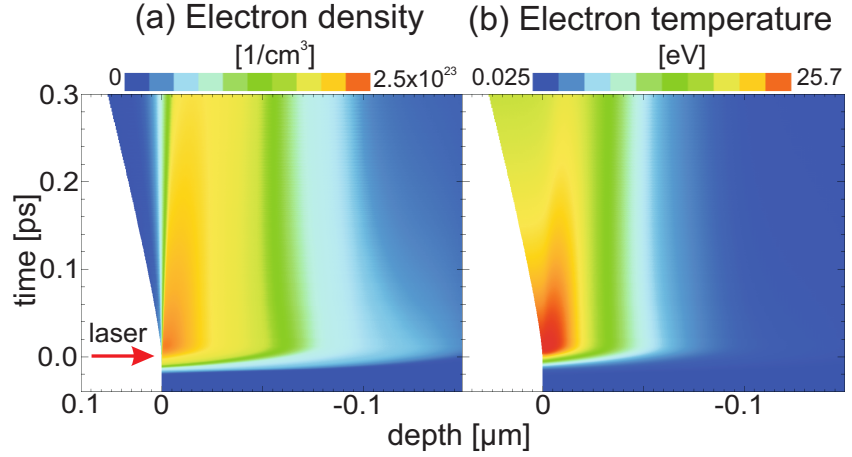


Figure 4.23: HELIOS simulation results for the electron density (left) and electron temperature (right) as a function of time and radius [13].

Hydrodynamics Simulation

To illustrate the hydrodynamic processes and to estimate the electron temperature, 1D radiation hydrodynamics simulations using HELIOS [89] have been performed¹³. Per atom, 2.6 conduction band electrons were assumed to contribute to the laser absorption [131]. The results are shown in Fig. 4.23. On the timescale of the FEL pulse, both electron density and temperature rise up to values of $n_e \simeq 10^{23} \text{ cm}^{-3}$ and $k_B T_e \simeq 26 \text{ eV}$, respectively, without any steep gradient. These values are in good qualitative agreement with the results for n_e and T_e obtained by the spectral analysis.

This hydrodynamics simulation uses the average pulse energy of $33 \mu\text{J}$ on target as an input parameter. As discussed above, Fig. 4.19 illustrates that a significant fraction of pulses have much higher pulse energies up to $130 \mu\text{J}$. Since the free-free emissivity (Eqn. 4.1) depends strongly non-linear both on electron temperature and density, we expect the observed radiation to be rather dominated by the high-energy fraction of the XUV pulses than by its average value. This finally explains the slight underestimation of the electron temperature in the hydrodynamics simulation compared to the experimental results.

Additionally, the simulation shows that these WDM conditions exist for about 200 fs, at almost constant plasma density and temperature, and hydrodynamic motion is negligible [132]. Plasma expansion as well as electron diffusion to the cold matter of the bulk

¹³HELIOS features a Lagrangian reference frame, i.e., grid moves with fluid, separate ion and electron temperatures, and flux-limited Spitzer thermal conductivity. It allows the deposition of laser energy via inverse bremsstrahlung as well as bound-bound and bound-free transitions, using a SESAME-like equation of state.

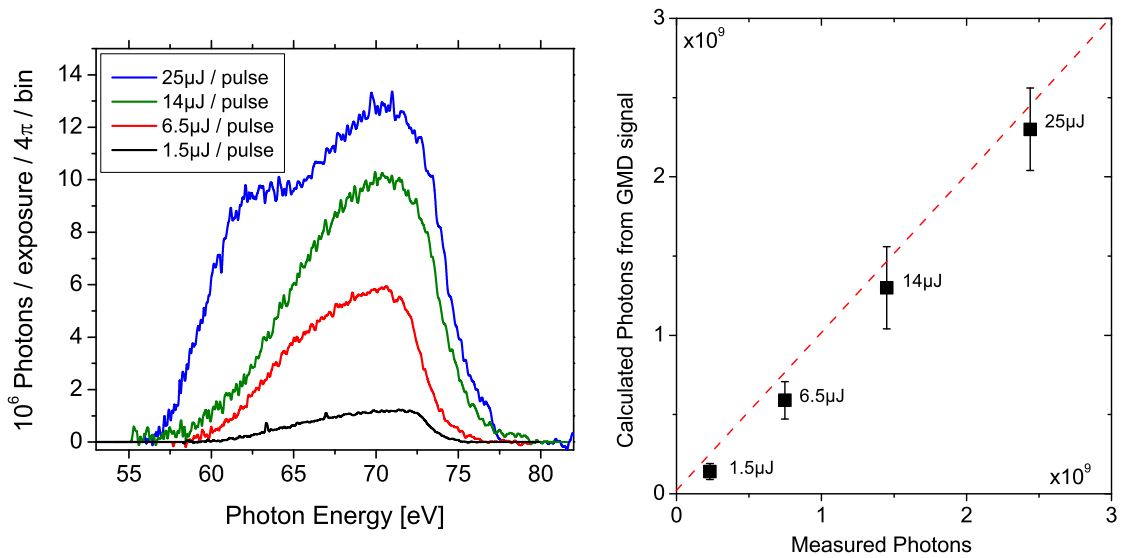


Figure 4.24: Left: Radiative decay spectra of the Al conduction band into L-vacancies at different irradiation fluencies. Right: The calculated photon yield compared to the measured signal (integration of the spectra in the left panel).

target and heat conduction become important during the first several picoseconds [133], while the density decreases by a factor of two, influencing the relative abundance of ion species only slightly, as demonstrated in Fig. 4.22.

4.5 Mapping the heated conduction band of aluminum

4.5.1 Radiative decay from the conduction band

The radiative recombination of electrons from the conduction band to the L_{III} or L_{II} levels results in emission that ranges in energy from approximately 62 eV ($\lambda \sim 20$ nm) (the energy difference between the L levels and the bottom of the valence band) to a thermally broadened region at an energy. This is corresponding to the difference between the Fermi energy and the L-shell - an energy of around the L-edge energy at 73 eV ($\lambda \sim 17$ nm). Its emission ends ~ 60 fs after irradiation, as discussed in the introductory part.

4.5.2 Experimental setup

Information about the electron distribution (and hence temperature) in the valence band on a femtosecond timescale can be inferred from soft x-ray emission spectra. We have measured such spectra in experiments corresponding to the fluence regime in the previous chapter 4.4, using a setup similar to the one described there:

At beamline BL2, a bulk pure aluminum sample was irradiated by 93.2 eV photons, focused to a 30 μm diameter focal spot. The only differences compared to the previously described spectroscopy are that we use (a) the HiTRaX-spectrometer (see ch. 4.3.3) and (b) vary the excitation fluence about an order of magnitude. First, the spectrometer is used without any filter foil. Experimental data were taken by means of integrated spectra of 300 FEL pulses, that is an integration time of one minute at 5 Hz.

4.5.3 Integrated emission yield

In order to analyze the radiative decay solely, the XUV signal of the recombining electrons at $\lambda = 17 - 20$ nm is extracted from the spectrum by subtracting any other background. We integrate the whole spectrometer signal to include all detected photons. By knowing the spectrometer efficiency and exposure time, absolute photon numbers are presented in the left panel of Fig. 4.24. Note the conversion from wavelength scale to photon energy, so that the analogy to the conduction band becomes more apparent.

The FEL pulse energy was varied from 25 to 14, 6.5, and 1.5 μJ . These are time-integrated values covering the exposure time. They are measured using the gas-monitor-detector (GMD) installed in the FEL facility [134]. The transmission of beamline BL2 is known to be 0.68, yielding fluencies of 2.4, 1.3, 0.62, and 0.14 J/cm^2 at the focal spot¹⁴.

As discussed, approximately every incident photon creates a L-shell vacancy. We multiply the incident photon number by the fluorescence yield of 2×10^{-3} and get the estimated photons emitted by the radiative decay, neglecting reabsorption. In the right panel of Fig. 4.24, the integrated photons from the spectroscopic data are compared to the calculated estimation. We find an excellent agreement, despite a systematical underestimation of the calculated photons. A possible source could be the assumption that the fluorescence yield of the plasma is the same as the one for the cold solid. Further, also the spectrometer efficiency is a source of uncertainty, since the values are calculated from the tabulated efficiency of the separate parts, and the hole spectrometer efficiency

¹⁴In intensity scale, this is 2.4, 1.3, 0.62, and $0.14 \times 10^{14} \text{ W}/\text{cm}^2$, assuming a pulse duration of 10 fs.

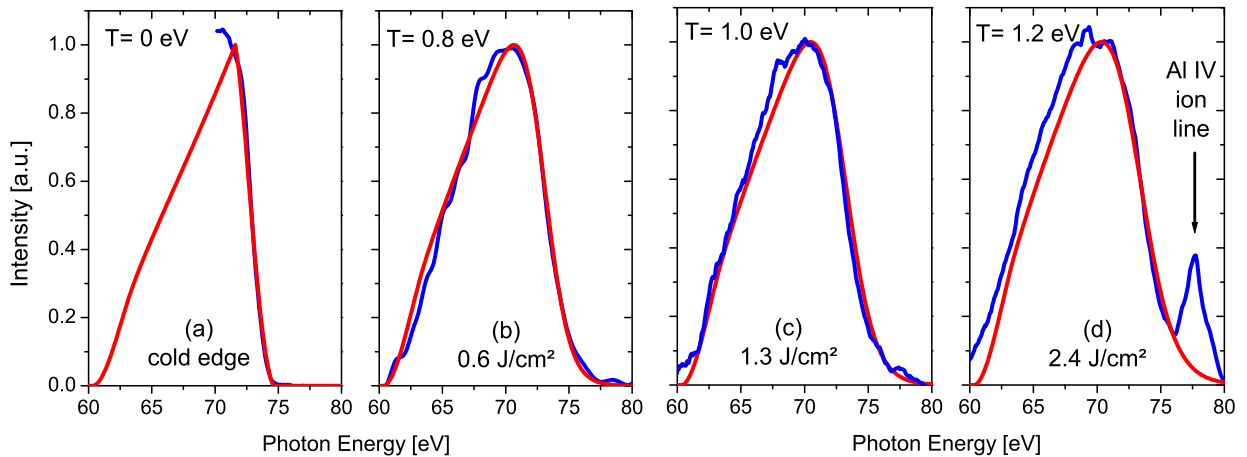


Figure 4.25: Fitting the cold L-absorption edge (a) and the radiative decay emission (b,c,d) at different irradiation fluencies.

was not experimentally calibrated.

4.5.4 Shape of the spectra

The soft x-ray emission is here seen to arise from the aluminum valence band from which we infer that the sample is still at solid density and the electrons are at a temperature that can be estimated by the slope of the spectra on the high energy edge. The spectra are compared to a free electron gas model as introduced in chapter 4.2.2. In order to maximize the spectrometer resolution, only a central profile of each spectrum was used, unlike in Fig. 4.24, where the full signal was integrated.

At ambient temperature, the thermal energy is ~ 30 meV, and the L-absorption edge is a step-like function at the photon energy of 72 eV [86]. Any increase of the conduction band temperature will lead to broadening of step-like shape. In order to compare the recorded spectra precisely to the 'cold' state, a 300 nm thin aluminum filter is introduced is a second exposure directly when the first exposure is finished. Thus, the precise position of the cold L-edge is known, independent of an absolute wavelength calibration of the spectrometer.

To fit the spectral data with the electron-gas model (see chapter 4.2.2), we need to correct for the limited spectrometer resolution. Thus, the calculated spectrum at 0 eV (or a few tens of meV) is convoluted with a instrument broadening function, such that it fits the shape of the cold Al absorption edge obtained from the exposure with Al filter.

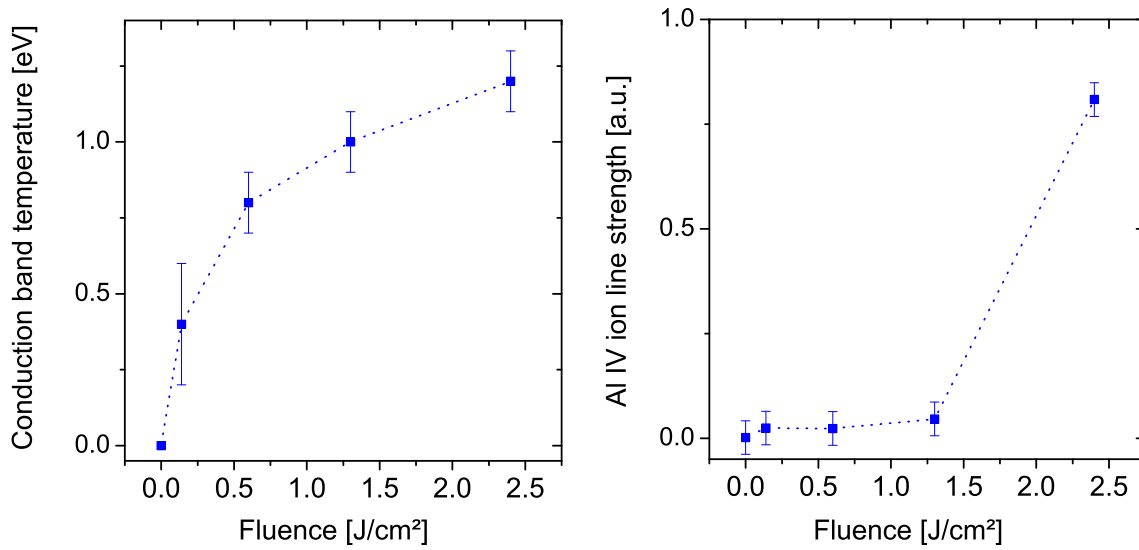


Figure 4.26: The conduction band temperature (left) and the Al-IV ion line intensity (right) as a function of irradiation fluence. Notice the onset of ionization.

4.5.5 Results - Conduction band temperature

The results are shown in Fig. 4.25. On the very left panel, the cold absorption edge is fitted by the electron-gas model, convoluted with the instrumental broadening function. For the slope of the absorption edge, a good agreement is accomplished. Hence, the right three panels show selected fits for radiative decay spectra, taken at different irradiation fluencies. While the slope close to the Fermi energy is reproduced with high accuracy, the spectrum at lower energies shows minor disagreements, which we ascribe to the free-electron gas assumption. Including the full density of states, however, does not improve the analysis, since the signal-to-noise ratio of the spectra is not high enough.

Further, notice the arise of the spectral line at $E = 77.5$ eV, which is the previously described Al IV ion line at $\lambda = 16$ nm (compare analysis in chapter 4.4). In metallic aluminum, this ion species is the first to show up. It hence indicates the onset of ionization at later times and therefore the much higher bulk temperatures of > 5 eV.

In this way, the electron temperature is inferred to be 1.2 eV, 1.0 eV, 0.8 eV, and 0.4 eV for fluencies of respectively 2.4, 1.3, 0.62, and 0.14 J/cm². The temperature dependence on the fluence is plotted in Fig. 4.26. Also, from the right panel we can state that significant ionization sets on when the irradiating fluence exceeds 1.5 J/cm².

4.6 Turning solid aluminum transparent

4.6.1 Saturable absorption

Saturable absorption, the decrease in the absorption of light with increasing intensity, is a well-known effect in the visible and near-visible region of the electromagnetic spectrum [135], and is a widely-exploited phenomenon in laser technology. Whilst there are many ways to induce this effect, in the simplest two-level system it will occur when the population of the lower, absorbing level is severely depleted, which requires light intensities sufficiently high to overcome relaxation from the upper level.

In this chapter, the production of saturable absorption of a metal in the soft x-ray regime by the creation of highly uniform warm dense conditions is reported. Further, the process by which the saturation of the absorption occurs will lead, after the XUV pulse, to the storage of about 100 eV/atom which in turn evolves to a warm dense state. This manner of creation is unique as one requires intense soft x-rays with a few ten femtoseconds duration to deposit the pulse energy well before thermalization and recombination can occur. Saturable absorption in the soft x-ray regime has not been observed yet, owing both to the lack of ultrashort, high intensity sources, and the rapid recombination times associated with such high photon energies.

This chapter presents the first measurements of the absorption coefficient of solid aluminum to sub-picosecond soft x-ray pulses with intensities up to and in excess of 10^{16} W cm⁻², two orders of magnitude higher than could previously be obtained.

In order to improve the organization and the success of experiments at FLASH, the so-called *Peak-Brightness-Collaboration* (PBC) was established, enabling the international members to share expertise, beamtime and expensive equipment. The transmission experiment reported in this chapter was performed under the leadership of Dr. Bob Nagler from University of Oxford. An explanation of the results in a sound physical picture was only possible by combining it with the XUV spectra recorded in experiments conducted by the author (chapter 4.5). The combined results were published in *Nature Physics* in 2009 [14].

4.6.2 Depletion of the L-shell

During the irradiation with an ~ 10 fs long XUV pulse, the sample absorbs predominantly via inner L-shell photo-ionization. As the pulse intensity is increased, the rate of

Figure 4.27: Schematic diagram of the experimental setup. The energy of the incoming beam is measured by the gas monitor detector (GMD). The beam is focused with an Off-Axis multilayer coated Mo/Si off axis parabola (OAP) onto the sample. The transmitted energy is measured by a silicon photodiode [14].

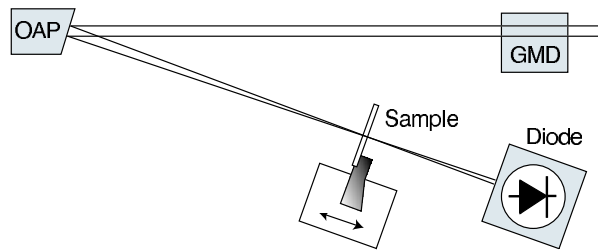


photo-ionization surpasses the recombination rate so that the inner-shell absorbers are severely depleted, leading to a saturation of the absorption, (i.e., the aluminum becomes highly transmissive).

During and after the irradiation, the photo-ionized electrons decay by two paths, radiative and Auger (radiation-less) decay. In principle the former provides spectral information on the temperature of the valence band while the latter transfers energy to the valence electrons that is effectively stored for times of order of several picoseconds (the electron-phonon coupling time). In this chapter, the first phase by measuring the transmission of the pulse over a wide range of fluencies is presented. Chapter 4.5 covers the second phase by analyzing the radiative decay at a set of lower fluencies by means of XUV spectroscopy.

4.6.3 Experimental setup

The experiment, shown in schematic form in Fig. 4.27, was performed using FLASH operating at a wavelength of 13.5 nm, i.e. a photon energy of 92 eV. The laser produced pulses of radiation containing between 10 and 50 μJ per pulse in a pulse length of order 15 fs at a repetition rate of 5 Hz.

Unlike the experiments reported in chapters 4.4 and 4.5, this time the highly-collimated beam of 5 mm diameter of beamline BL3 was focused onto solid samples using a Mo/Si multi-layer-coated off-axis parabola, provided by LLNL¹⁵. It has a focal length of 269 mm, and reflectivity of $\sim 48\%$ ¹⁶. Focal spot sizes were determined to be 1.5 μm at best focus by using Nomarski optical microscopy and atomic force microscopy to look at damage craters induced by the radiation on PMMA¹⁷ [136]. This is equivalent to record intensities of 10^{16} W/cm² at 92 eV photon energy.

The aluminum samples were placed at nine different positions from best focus, with

¹⁵Lawrence Livermore National Laboratory, California, USA.

¹⁶The reflectivity decreases constantly because of surface contamination and XUV-induced chemical degeneracy.

¹⁷PMMA: polymethyl methacrylate.

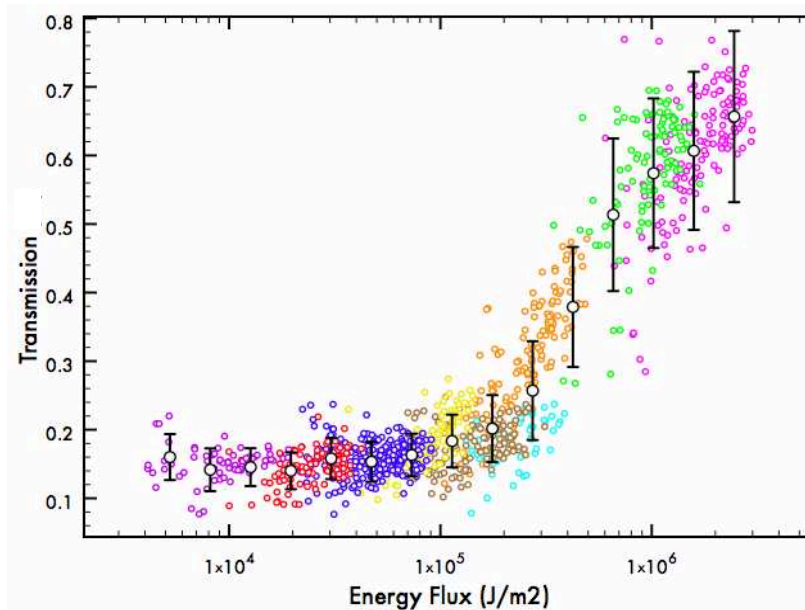


Figure 4.28: Transmission of aluminum target as a function of fluence. The colored points are individual measurements, and each color represents one fixed focal distance. This data is superimposed by the integrated data points with a 1σ error bar [14].

the FWHM diameter of the laser spot varying from $1.5\ \mu\text{m}$ at best focus, up to $45\ \mu\text{m}$. The energy within each pulse was measured with a gas-monitor detector (GMD) [134]. By variation of both the sample position and laser energies, three orders in magnitude of laser fluence were scanned. The transmission of a $53\ \text{nm}$ thin aluminum foil was recorded as a function of laser fluence using a silicon photodiode, which was calibrated with the GMD energies in the absence of a sample. The calibration shows a linear correlation of the GMD signal with respect to the photodiodes. However, this measurement shows a $\pm 10\%$ shot-to-shot error, which limits the accuracy of the measured absorption to $\pm 10\%$ on a shot-to-shot basis. Statistically larger variations between GMD and photodiode readings were found for the lowest beam energies ($\leq 10\ \mu\text{J}$), and such unusually low energy shots are excluded from the analysis.

With an unexposed region of the aluminum sample in place the transmission is measured by comparing the energies recorded by the calibrated photodiode and GMD for every shot. Transmission as a function of fluence is shown in Fig. 4.28. Saturable absorption can readily be seen in the experimental data, with an increase in transmission from 15% at the lowest fluence of $0.3\ \text{J cm}^{-2}$, to 65% at a fluence of $2 \times 10^2\ \text{J cm}^{-2}$. Given a pulse length of $15\ \text{fs}$, these limits correspond to irradiances of $2 \times 10^{13}\ \text{W cm}^{-2}$ and $1.5 \times 10^{16}\ \text{W cm}^{-2}$, respectively.

4.6.4 Transmission data analysis

At high intensities the fraction of aluminum atoms with photo-ionized L-shell electrons is high, leading to less absorption of the propagating pulse: after an electron is ejected from the L-shell of an atom, the L-edge of that particular atom will increase due to reduced screening. The energy needed to eject a second L-shell electron is calculated to be 93 eV [137], which is confirmed by measurements of Auger energies [137, 138]. Therefore, the FEL (at 92.5 eV) will not be able to create a second L-shell hole; the photo-ionization quenches and the absorption coefficient are heavily reduced to the value of the free-free absorption.

However, the total lifetime of such an L-shell vacancy (which is much shorter than the radiative lifetime) is estimated to be around 40 – 60 fs (see ref. [109] and chapter 4.2.4), i.e. long compared with the FLASH pulse length, but still short compared with any electron-phonon coupling time, or hydrodynamic motion. Thus, the loss of L-shell electrons during the initial part of the FLASH pulse results in reduced absorption during the rest of the pulse – an effect that is negligible at previously accessible soft x-ray intensities.

Thermal ionization of the L-shell does not occur on these short time-scales, as it requires a temperature above 10 eV at solid densities [139].

Photo-ionization time-scales and homogeneous heating

Immediately after the passage of the FLASH pulse, where the high transmission indicates that almost every atom has an L-shell hole, we expect the aluminum ions to be close to their original lattice positions: the expected electron-phonon coupling time is over a picosecond [140] and even after receiving energy from the electrons, an aluminum ion with a temperature of a few eV takes more than 50 fs to traverse a lattice spacing. Thus, at the instant the pulse has passed, we can infer that the aluminum is in a highly-ionized, yet crystalline state, of which the physical properties are largely unknown.

Saturating an absorption edge allows for a very uniform heating of a sample: while the front part of the pulse is absorbed and heats the front of the sample, the back of the pulse will pass through this bleached region, heating the back of the sample to nearly the same temperature. For example, at 100 J cm^{-2} , 50% of the FEL pulse will be absorbed (see Fig. 4.28), but the temperature difference between the front and the back of the sample is calculated to be only 5%. This compares favorably with experiments where thin samples are heated with high intensity optical lasers. While such experiments have

yielded excellent results and increased our understanding of WDM significantly (see chapter 3), the sample thickness that can be uniformly heated in this way is ultimately limited by the electron ballistic depth of the hot electrons that the laser generates.

4.7 Summary

The FLASH facility at DESY in Hamburg is world-wide the first soft x-ray laser with femtosecond pulse duration. Using appropriate focusing optics, record soft-x-ray intensities of $> 10^{16} \text{ W/cm}^2$ are achieved - intensities which are comparable to those of femtosecond optical lasers. Due to the short wavelength, the physics of laser-matter interaction is totally different compared to the optical regime, since direct photo-ionization of bound electrons is dominating.

In this work, pioneering experiments to create plasma at warm dense matter conditions are reported. Theoretical descriptions, computational calculations, experimental techniques and devices, as well as several spectroscopic methods were developed and demonstrated for the first time.

First, the process of photo-absorption of soft x-rays by inner-shell electrons is analyzed in chapter 4.2. The process is found to be highly linear and controlled. In particular, we studied aluminum irradiated by $\sim 90 \text{ eV}$ photons. We discuss the creation of L-shell vacancies, secondary Auger electrons, and radiative decay. The evolution of the plasma is studied by means of Monte-Carlo simulations on a femtosecond-timescale.

Second, the principles of broadband XUV plasma spectroscopy with focus on high efficiency and resolution are investigated in chapter 4.3. Principles of grazing incidence reflection mirrors, gratings, suitable filters and efficient detectors are presented. The analysis and employment of an available transmission-grating spectrometer lead to the design of an improved flat-field reflection-grating spectrometer. This spectrometer, called HiTRaX, increases both spectral range and resolution by a factor of two, while the efficiency gains at least a factor of 6, compared to the former transmission-grating device.

In Chapter 4.4, an experiment is presented that demonstrates the capability of XUV FEL radiation to create WDM by interaction with a solid aluminum target for the first time. Soft x-ray intensities in the order of 10^{14} W/cm^2 are focused onto bulk aluminum. The analysis of the XUV line and continuum emission spectra yields an electron temperature of $(34 \pm 6) \text{ eV}$ and $(40.5 \pm 5.5) \text{ eV}$, respectively. The observed line spectrum is compatible with predicted ion abundances. Together with radiation hydrodynamics modeling, we get a sound picture of complex XUV laser-plasma interaction dynamics. The simulations confirm the volumetric heating of the target without strong gradients.

Our results provide new complementary information to results that were reported for optical laser-matter interaction.

Subsequently, using the new-built HiTRaX-spectrometer, we are able to observe the FEL-induced radiative decay emission from the heated conduction band into the L-vacancies (chapter 4.5). This emission stems from the first 60 fs after irradiation, since Auger recombination will fill the holes rapidly. From the analysis, we find low temperatures of ~ 1 eV for a set of irradiances around 10^{14} W/cm². We conclude that the high-energy Auger electrons do not significantly contribute to the heating of the conduction band within the first tens of femtoseconds.

Finally, in chapter 4.6, a multilayered parabola is employed to focus the soft x-rays to record intensities of $\leq 10^{16}$ W/cm². The results show the first demonstration of saturable absorption in the x-ray regime. The observations are consistent with the ejection of an L-electron from almost all atoms in the sample on femtosecond time-scales. By bleaching the L absorption-edge within 15 fs, a much shorter timescale than the picoseconds calculated to be necessary for electron-ion equilibration, we infer that we have created a very transient exotic state of highly ionized crystalline matter. Further, the transparent state leads to an even more homogeneous deposition of the photon energy, since the absorption length is strongly increased.

5 General Summary and Outlook

This thesis presents the application of innovative methods to create and investigate warm dense matter using XUV and x-ray radiation. This non-equilibrium-state, located between condensed matter and hot plasmas, is generated in high-energy-density experiments, and its properties have been studied with high precision.

The creation of a *defined* state of warm dense matter using optical lasers at intensities of several 10^{19} W/cm² is challenging. Hot electrons from a tiny, hot plasma at the target surface heat the cold matter via impact ionization. High spectral and spatial resolutions are required to avoid integration of differing plasma states. The author applied sophisticated x-ray spectroscopy of emitted characteristic x-rays, together with numerical data post-processing, and reveals a strong set of information, since the line shape is influenced by the plasma parameters, and they penetrate solid density. Experiments using thin titanium foils yield radial maps of the bulk-electron temperature and the $K\alpha$ -yield at solid density from single laser exposures. Unexpectedly, a homogeneously heated core extends up 10 times than the laser focus. Further, the distributions of the radial temperature and x-ray yield show a strong similarity in every single shot, indicating that the distribution of electrons creating K-holes is similar to the one heating the bulk electrons. Finally, the global $K\alpha$ yield as a function of target thickness is explained by Monte-Carlo simulations. The author developed a model with partially refluxing electrons which reproduces the measured yield and further allows an estimation of depth-dependent energy deposition. Since laser-driven sources of x-rays are of high importance as backlighters, parameters to optimize the brilliance of such x-ray sources for various proposes are derived.

Alternative ways of generating warm dense matter are currently in the focus of high-energy-density scientists. In this work, it is demonstrated for the first time that warm dense matter can be generated by photo-ionizing bound electrons, using femtosecond pulses delivered by the world's first soft x-ray laser FLASH. Within the framework of

the international *Peak-Brightness-Collaboration*, the author was in charge of pioneering studies. An aluminum sample was irradiated with 92 eV-photons at intensities of $10^{14} - 10^{16}$ W/cm². Its self-emission was surveyed by high-resolution XUV spectroscopy. For this purpose, a flat-field reflection-grating XUV spectrometer *HiTRaX* was designed to fulfill the experimental needs. The analysis of the time-integrated XUV spectra by means of ionic lines and bremsstrahlung radiation reveals a plasma at $k_B T = (30 - 40)$ eV close to solid density.

Further, it became possible to observe the heated conduction band of a warm dense plasma. Radiative-decay emission from the conduction band into L-shell vacancies is analyzed, stemming only from the first 60 fs after irradiation. At later times, radiative decay becomes impossible since Auger-recombination fills the L-holes rapidly. Low temperatures of $k_B T \sim 1$ eV for the conduction band are derived, and it is concluded that Auger-recombination does not significantly contribute to the heating of the conduction band within the first tens of femtoseconds.

Finally, the first demonstration of saturable absorption in the soft x-ray regime was realized at record intensities of $\leq 10^{16}$ W/cm². When such a pulse traverses a 50 nm thin aluminum foil, the leading wing ionizes one L-electron in nearly every atom in the beam path. The rest of the XUV-pulse is no longer photo-absorbed by the L-electrons. It loses energy mainly via the weak free-free absorption. Therefore, the foil becomes transparent for the XUV radiation. Together with the measurement of the conduction band temperature on a femtosecond timescale, it is evident that a very transient exotic state of highly ionized crystalline matter has been generated. The transparent state leads to an even more homogeneous plasma, since the absorption length is increased and a significant part of the XUV-pulse deposits its energy in deeper layers of the sample.

In conclusion, this thesis is aimed at the exploration of a defined state of warm dense matter. The knowledge is highly important for the realization of laser-fusion research, a variety of astrophysically relevant plasma research, and for backlighting high-density states.

Outlook. - Using optical lasers, we pointed out that micrometer-scale spatial variations of the plasma parameters are likely. Thus, we increase the spatial and spectral resolution of the x-ray diagnostics in such a way that the expected changes can be well resolved. A further logical step is to implement picosecond time resolution by means of single-shot x-ray streak cameras. As we show, the creation of a defined plasma state also depends on preplasma conditions. Hence, a high-quality laser pulse with short duration and high

energy content is required. The development of alternative concepts such as all-diode-pumped CPA or OPCPA¹-based systems is currently evolving, and these systems will be opened to the community within the next years. Finally, the design of targets also influences the process of fast-electron heating. As we show, refluxing of electrons due to strong electric fields changes the plasma parameters. The process changes both the plasma temperature and the x-ray yield as a function of target foil thickness. By changing the target geometry in the future, e.g. using a wire or an isolated dot, even more homogeneous plasma creation due to increased refluxing can be expected.

In a second approach, we employed the first accelerator-based soft x-ray laser FLASH to generate WDM. Using x-rays, the target heating is direct via photo-ionization. The plasma is undercritical at all stages, and non-linear effects can be avoided. In September 2009, the x-ray FEL *Linac Coherent Light Source* (LCLS) in Stanford (California) reported first lasing at 2 keV photon energy. In the near future, facilities such as the European XFEL in Hamburg (Germany) will become operational at even shorter wavelengths below 1 Å. These open new opportunities, either to excite even stronger bound K-shell electrons, or to probe dense plasma with femtosecond time resolution. For this purpose, the MEC² endstation at LCLS is under construction, strongly supported and designed by the plasma physicists to meet their needs.

¹optical parametric chirped-pulse amplifier

²Matter in Exotic Conditions

6 Zusammenfassung

Die vorliegende Arbeit zeigt innovative Methoden der Erzeugung und Charakterisierung warmer dichter Materie auf. Dieser Nicht-Gleichgewichts-Zustand zwischen kaltem Festkörper und idealem Plasma wird durch Experimente mit hoher Energiedichte erzeugt. Seine Eigenschaften wurden mit hoher Präzision studiert.

Die Erzeugung eines definierten Zustandes warmer dichter Materie mit Hilfe optischer Kurzpluslaser und Intensitäten von mehreren 10^{19} W/cm^2 ist herausfordernd. Energiereiche Elektronen aus einem kleinen, heißen Plasma auf der Targetvorderseite heizen die kalte Materie durch Stoßionisation auf. Hohe spektrale sowie räumliche Auflösungen sind nötig, um nicht über verschiedene Plasmazustände zu mitteln. Der Autor wendet hoch entwickelte Röntgenspektroskopie charakteristischer Emissionslinien, gefolgt von numerischer Datenverarbeitung, an. Das Ergebnis enthält viele Informationen, da die Linienform durch die Plasmaparameter beeinflusst wird und die Röntgenstrahlen zudem transparent für Festkörperdichte sind. Experimente an dünnen Titanfolien ergeben radiale Karten der Plasmatemperaturverteilung und der $K\alpha$ -Ausbeute bei Festkörperdichte von einzelnen Laser-Experimenten. Unerwarteterweise zeigt sich ein homogen geheizter Zentralbereich, dessen Ausdehnung bis zu zehnmal so groß wie der Laserfokus ist. Weiterhin sind die radialen Verteilungen von Temperatur und Ausbeute von jedem einzelnen Experiment stark korreliert, was zeigt, dass die Elektronenverteilung, die K-Schalen-Löcher hervorruft, ähnlich der Verteilung ist, die die Titan-Atome heizt. Schließlich wird die globale $K\alpha$ -Ausbeute aus Funktion der Foliendicke durch Monte-Carlo-Simulationen erklärt. Das zugrundeliegende Modell mit teilweise rückströmenden Elektronen ist in der Lage, die gemessene Röntgenausbeute zu reproduzieren und gibt weiterhin Einblick in die tiefenabhängige Energiedeposition. Da Laser-Plasma-Röntgenquellen eine große Bedeutung als Backlighter besitzen, werden Parameter abgeleitet, um deren Brillianz für viele Anwendungen zu optimieren.

Alternative Wege zur Erzeugung warmer dichter Materie sind momentan im Fokus der Hohe-Energiedichte-Forschung. In der vorliegenden Arbeit wird erstmals die Erzeugung

warmer dichter Materie durch direkte Photoionisation gebundener Elektronen mit den Femtosekundenpulsen des weltweit ersten weichen Röntgenlasers FLASH demonstriert. Innerhalb der durch die internationale *Peak-Brightness-Collaboration* geschaffenen Rahmenbedingungen war der Autor verantwortlich für Pionierarbeiten.

Eine Aluminiumprobe wird mit 92 eV-Photonen und Intensitäten von 10^{14} – 10^{16} W/cm² bestrahlt und die Plasmaemission mit hochauflösender XUV-Spektroskopie erfasst. Um die experimentellen Voraussetzungen zu erfüllen, wurde ein Flatfield-Reflexionsgitter XUV-Spektrometer *HiTRaX* entwickelt. Die Analyse der zeitintegrierten XUV-Spektren unter Berücksichtigung von Ionenlinien und Bremsstrahlung ergibt ein Plasma mit $k_B T = (30 - 40)$ eV nahe Festkörperdichte.

Weiterhin wurde es möglich, das geheizte Leitungsband warmer dichter Plasmen zu studieren. Rekombinationsstrahlung aus dem Leitungsband in L-Schalen-Löcher, das nur aus den ersten 60 fs nach der Anregung stammt, wird analysiert. Zu späteren Zeiten tritt keine strahlende Rekombination mehr auf, da Auger-Rekombination die L-Löcher schnell füllt. Niedrige Temperaturen von $k_B T \sim 1$ eV werden für das Leitungsband abgeleitet. Folgerichtig tragen die schnellen Augerelektronen innerhalb der ersten 60 Femtosekunden noch nicht signifikant zur Erwärmung des Leitungsbandes bei.

Schließlich gelang die erste Demonstration sättigbarer Absorption im weichen Röntgenbereich bei Rekord-Intensitäten von $\leq 10^{16}$ W/cm². Wenn ein hochintensiver Puls eine 50 nm dünne Aluminiumfolie durchquert, ionisiert die führende Flanke ein L-Elektron in nahezu jedem Atom im Strahlweg. Der verbleibende Teil des Pulses kann nun nicht mehr durch L-Elektronen absorbiert werden, sondern verliert hauptsächlich Energie durch die viel schwächere Frei-frei-Absorption. Daher wird die Folie praktisch transparent für die verwendete XUV-Strahlung. Zusammen mit der Messung der Leitungsbandtemperatur auf Femtosekunden-Zeitskalen wird klar, dass ein sehr transients exotischer Zustand hochionisierter kristalliner Materie erzeugt wird. Der transparente Zustand führt zu noch homogener geheiztem Plasma, da die Absorptionslänge sich erhöht und ein signifikanter Teil des XUV-Pulses seine Energie in tiefen Schichten der Probe deponiert.

Zusammenfassend widmet sich die vorliegende Arbeit der Erforschung definierter Zustände warmer dichter Materie. Dieses Wissen ist von herausragender Bedeutung für die Laser-Fusions-Forschung, die Erforschung von Materiezuständen mit hoher Dichte, sowie eine Vielzahl astrophysikalisch-relevanter Fragestellungen der Plasmaforschung.

Bibliography

- [1] R. W. Lee et al. Plasma-based studies with intense x-ray and particle beam sources. Laser Part. Beams, 20:527, 2002.
- [2] A. Saemann et al. Isochoric heating of solid aluminum by ultrashort laser pulses focused on a tamped target. Phys. Rev. Lett., 82(24):4843–4846, 1999.
- [3] Y. Ping et al. Broadband dielectric function of nonequilibrium warm dense gold. Phys. Rev. Lett., 96:255003, 2006.
- [4] T. Ao et al. Optical properties in nonequilibrium phase transitions. Phys. Rev. Lett., 96:055001, 2006.
- [5] K. Widmann et al. Single state measurement of electrical conductivity of warm dense gold. Phys. Rev. Lett., 92:125002, 2004.
- [6] G. W. Collins et al. Temperature measurement of shock compressed liquid deuterium up to 230 gpa. Phys. Rev. Lett., 87:165504, 2001.
- [7] L. B. Da Silva et al. Absolution equation of state measurements on shocked liquid deuterium up to 200 gpa (2mbar). Phys. Rev. Lett., 78:483, 1997.
- [8] R. Sigel et al. X-ray generation in a cavity heated by 1.3- or 0.44- μ m laser light. Phys. Rev. A, 38(11):5756–5785, 1988.
- [9] T. S. Perry et al. Absorption experiments on x-ray-heated mid-z constrained samples. Phys. Rev. E, 54:5617, 1996.
- [10] J. J. MacFarlane et al. X-ray absorption spectroscopy measurements of foil heating by z-pinch radiation. Phys. Rev. E, 66:046416, 2002.
- [11] DHH. Hoffmann et al. Present and future perspectives for high energy density physics with intense heavy ion and laser beams. Laser and Particle Beams, 23:47–53, jan 2005.
- [12] P.K. Patel et al. Isochoric heating of solid-density matter with an ultrafast proton beam. Phys. Rev. Lett., 91:125004, 2003.
- [13] U. Zastra, C. Fortmann, et al. Bremsstrahlung and Line Spectroscopy of warm dense Aluminum heated by XUV Free Electron Laser. Phys. Rev. E, 78:066406, 2008.

- [14] B. Nagler, U. Zastra, et al. Turning solid Aluminum Transparent by intense soft x-ray photoionization. Nature Physics, 5:693–696, 2009.
- [15] C. Reich et al. Yield Optimization and Time Structure of Femtosecond Laser Plasma $K\alpha$ Sources. Phys. Rev. Lett., 84:4846–4849, 2000.
- [16] O. L. Landen, D. R. Farley, et al. X-ray backlighting for the National Ignition Facility (invited). Rev. Sci. Instr., 72:627–634, jan 2001.
- [17] H.-S. Park, N. Izumi, et al. Characteristics of high energy $K\alpha$ and Bremsstrahlung sources generated by short pulse petawatt lasers. Rev. Sci. Instr., 75:4048–4050, oct 2004.
- [18] A. Pukhov and J. Meyer ter Vehn. Relativistic magnetic self-channeling of light in near-critical plasma: Three-dimensional particle-in-cell simulation. Phys. Rev. Lett., 76(21):3975–3978, 1996.
- [19] W.P. Leemans et al. GeV electron beams from a centimetre-scale accelerator. Nature Physics, 2:696–699, 2006.
- [20] H. Schworer et al. Laser plasma acceleration of quasi-monoenergetic protons from microstructured targets. Nature, 439:445–448, 2006.
- [21] U. Rochester. Matter at high-energy densities. Laboratory for Laser Energetics, 1:10, 2004.
- [22] JD. Lindl et al. The physics basis for ignition using indirect-drive targets in the National Ignition Facility. Phys. Plasmas, 11:339–491, 2004.
- [23] T. R. Dittrich et al. Review of indirect-drive ignition design options for the nation ignition facility. Phys. Plasmas, 6:2164, 1999.
- [24] M. Tabak, J. Hammer, et al. Ignition and high gain with ultrapowerful lasers. Phys. Plasmas, 1:1626–1634, may 1994.
- [25] J.A. King, K.U. Akli, et al. Studies on the transport of high intensity laser-generated hot electrons in cone coupled wire targets. Physics of Plasmas, 16(2):020701, 2009.
- [26] M.H. Key. Status of and prospects for the fast ignition inertial fusion concept. Physics of Plasmas, 14(5):055502, 2007.
- [27] Ch. Reich et al. Spatial characteristics of $k\alpha$ x-ray emission from relativistic femtosecond laser plasmas. Phys. Rev. E, 68(5):056408, 2003.
- [28] E.E. Fill. Relativistic electron beams in conducting solids and dense plasmas: Approximate analytical theory. Physics of Plasmas, 8(4):1441–1444, 2001.

- [29] M. Silies et al. Table-top kHz hard X-ray source with ultrashort pulse duration for time-resolved X-ray diffraction. Applied Physics A: Materials Science & Processing, 96:59–67, jul 2009.
- [30] I. Uschmann et al. Investigation of fast processes in condensed matter by time-resolved x-ray diffraction. Applied Physics A: Materials Science & Processing, 96:91–98, jul 2009.
- [31] S. H. Glenzer et al. Demonstration of spectrally resolved x-ray scattering in dense plasmas. Phys. Rev. Lett., 90(17):175002, 2003.
- [32] H.J. Lee, P. Neumayer, et al. X-ray thomson-scattering measurements of density and temperature in shock-compressed beryllium. Physical Review Letters, 102(11):115001, 2009.
- [33] R.R. Faeustlin et al. Thomson scattering at cryogenic hydrogen using flash. Phys. Rev. Lett., -:submitted, 2010.
- [34] D. Saumon et al. Modelling pressure-ionization of hydrogen in the context of astrophysics. High Pressure Res., 16:331, 2000.
- [35] N. Nettelmann et al. Ab initio equation of state data for hydrogen, helium, and water and the internal structure of jupiter. Astrophys. J., 683:1217, 2008.
- [36] C. Ziener, I. Uschmann, et al. Optimization of $K\alpha$ bursts for photon energies between 1.7 and 7 keV produced by femtosecond-laser-produced plasmas of different scale length. Phys. Rev. E, 65(6):066411–+, 2002.
- [37] DW. Forslund, JM. Kindel, et al. Theory and simulation of resonant absorption in a hot plasma. Phys. Rev. A, 11(2):679–683, 1975.
- [38] F. Brunel. Not-so-resonant, resonant absorption. Phys. Rev. Lett., 59(1):52–55, 1987.
- [39] P. Gibbon and AR. Bell. Collisionless absorption in sharp-edged plasmas. Phys. Rev. Lett., 68(10):1535–1538, Mar 1992.
- [40] TY. Brian Yang, L. Kruer, et al. Mechanisms for collisionless absorption of light waves obliquely incident on overdense plasmas with steep density gradients. Phys. Plasmas, 3(7):2702–2709, 1996.
- [41] LM. Chen, J. Zhang, QL. Dong, et al. Hot electron generation via vacuum heating process in femtosecond laser–solid interactions. Physics of Plasmas, 8(6):2925–2929, 2001.
- [42] J. Denavit. Absorption of high-intensity subpicosecond lasers on solid density targets. Phys. Rev. Lett., 69(21):3052–3055, Nov 1992.

- [43] SC. Wilks, WL. Kruer, et al. Absorption of ultra-intense laser pulses. Phys. Rev. Lett., 69:1383–1386, aug 1992.
- [44] S.H. Glenzer and R. Redmer. X-ray Thomson Scattering in High Energy Density Plasmas. Rev. Mod. Phys., accepted, 2008.
- [45] J.P. Gordon. Radiation Forces and Momenta in Dielectric Media. Phys. Rev. A, 8:14–21, 1973.
- [46] G. Malka and JL. Miquel. Experimental confirmation of ponderomotive-force electrons produced by an ultrarelativistic laser pulse on a solid target. Phys. Rev. Lett., 77(1):75–78, 1996.
- [47] F.N. Beg, A.R. Bell, et al. A study of picosecond laser–solid interactions up to 10¹⁹ w cm⁻². Phys. Plasmas, 4(2):447–457, 1997.
- [48] B. Hidding et al. Novel method for characterizing relativistic electron beams in a harsh laser-plasma environment. Rev. Sci. Instr., 78(8):083301–+, 2007.
- [49] F. Zamponi. Electron Propagation in solid matter as a result of relativistic laser plasma interactions. PhD thesis, Friedrich-Schiller University Jena, 2007.
- [50] AJ. Kemp, Y. Sentoku, V. Sotnikov, and SC. Wilks. Collisional relaxation of superthermal electrons generated by relativistic laser pulses in dense plasma. Physical Review Letters, 97(23):235001, 2006.
- [51] P. Gibbon et al. Short-pulse laser-plasma interactions. Plasma Phys. Control. Fusion, 38:769–793, 1996.
- [52] L. Spitzer. Physics of fully ionized gases. B. Marshak, New York, 1956.
- [53] T. Feurer, W. Theobald, et al. Onset of diffuse reflectivity and fast electron flux inhibition in 528-nm-laser–solid interactions at ultrahigh intensity. Phys. Rev. E, 56(4):4608–4614, 1997.
- [54] J.D. Huba. NRL plasma formulary. Office of naval research, Washington DC 20375, 2009.
- [55] A.R. Bell et al. Fast-electron transport in high-intensity short-pulse laser - solid experiments. Plasma Physics and Controlled Fusion, 39:653–659, 1997.
- [56] R.G. Evans. Modelling short pulse, high intensity laser plasma interactions. HEDP, 1:35–47, 2006.
- [57] A.P.L. Robinson and M. Sherlock. Magnetic collimation of fast electrons produced by ultraintense laser irradiation by structuring the target composition. Phys. Plasmas, 14(8):083105–+, aug 2007.

- [58] G. Malka, M.M. Aleonard, et al. Relativistic electron generation in interactions of a 30 tw laser pulse with a thin foil target. Phys. Rev. E, 66(6):066402, 2002.
- [59] G. Malka, Ph. Nicolai, et al. Fast electron transport and induced heating in solid targets from rear-side interferometry imaging. Phys. Rev. E, 77(2):026408, 2008.
- [60] E. Casnati, A. Tartari, and C. Baraldi. An empirical approach to K-shell ionisation cross section by electrons. J. Phys. B Atom. Mol. Phys., 15:155–167, 1982.
- [61] CA. Quarles. Semiempirical analysis of electron-induced K-shell ionization. Phys. Rev. A, 13:1278–1280, 1976.
- [62] JP. Santos, F. Parente, and YK. Kim. Cross sections for K-shell ionization of atoms by electron impact. J. Phys. B Atom. Molec. Phys., 36:4211–4224, 2003.
- [63] G. Zschornack. Atomdaten für die Röntgenspektral-Analyse. Springer Berlin, 1989.
- [64] P.H. Mokler and F. Folkmann. X-ray production in heavy ion-atoms collisions in: Structure and collisions of ions and atoms, volume 5. Springer Berlin, New York, 1978.
- [65] D. Jung et al. Experimental characterization of picosecond laser interaction with solid targets. Phys. Rev. E, 77(5):056403–+, 2008.
- [66] E. Stambulchik, V. Bernshtam, et al. Progress in line-shape modeling of K-shell transitions in warm dense titanium plasmas. J. Phys. A: Math. Gen., 42, 2009. Accepted for publication.
- [67] A. Sengebusch, H. Reinholz, et al. K-line emission profiles with focus on the self-consistent calculation of plasma polarization. J. Phys. A: Math. Gen., 42, 2009. Submitted.
- [68] M.F. Gu. The flexible atomic code. Can. J. Phys., 86:675–689, 2008.
- [69] DC. Eder, G. Pretzler, et al. Spatial characteristics of $K\alpha$ radiation from weakly relativistic laser plasmas. Applied Physics B: Lasers and Optics, 70:211–217, 2000.
- [70] S.B. Hansen et al. Temperature determination using $K\alpha$ spectra from M -shell Ti ions. Phys. Rev. E, 72(3):036408–+, 2005.
- [71] S.N. Chen et al. Creation of hot dense matter in short-pulse laser-plasma interaction with tamped titanium foils. Phys. Plasmas, 14(10):102701–+, 2007.
- [72] P. Audebert, R. Shepherd, et al. Heating of thin foils with a relativistic-intensity short-pulse laser. Phys. Rev. Lett., 89(26):265001, 2002.
- [73] T. Missalla et al. Monochromatic focusing of subpicosecond x-ray pulses in the kev range. Rev. Sci. Instr., 70(2):1288–1299, 1999.

- [74] H.H. Johann. Die erzeugung lichtstarker roentgenspectren mit konkaven kristallen. Zeitschrift fuer Physik, 69:185–206, may 1931.
- [75] I. Uschmann, E. Förster, et al. X-ray reflection properties of elastically bent perfect crystals in Bragg geometry. Journal of Applied Crystallography, 26(3):405–412, jun 1993.
- [76] M. Dirksmöller, O. Rancu, et al. Time resolved X-ray monochromatic imaging of a laser-produced plasma at 0.6635 nm wavelength. Optics Communications, 118:379–387, 1995.
- [77] M. Dirksmöller. Einzel- und Doppelkristallanordnungen zur hochauflösenden röntgenoptischen Anordnung. PhD thesis, Jena University, Jena, 1996. Dissertation.
- [78] I. Uschmann et al. X-ray emission produced by hot electrons from fs-laser produced plasma- diagnostic and application. Laser Part. Beams, 17:671–679, 1999.
- [79] Physikalisch-Technische Bundesanstalt. Calibration certificate, 2006.
- [80] J.P. Zou et al. The LULI 100-TW Ti:sapphire/Nd:glass laser: a first step towards a high performance petawatt facility. ICF SPIE, 1998.
- [81] B. Wattellier et al. Repetition rate increase and diffraction-limited focal spots for a nonthermal-equilibrium 100-tw nd:glass laser chain by use of adaptive optics. Opt. Lett., 29:2494–2496, 2004.
- [82] B. Wattellier et al. Generation of a single hot spot by use of a deformable mirror and study of its propagation in an underdense plasma. J. Opt. Soc. Am. B, 20:1632–1642, 2003.
- [83] D. Strickland and G. Mourou. Compression of amplified chirped optical pulses. Optics Communications, 56:219–221, 1985.
- [84] S. D. Baton, M. Koenig, et al. Inhibition of fast electron energy deposition due to preplasma filling of cone-attached targets. Phys. Plasmas, 15(4):042706–+, apr 2008.
- [85] S.N. Chen et al. X-ray spectroscopy of buried layer foils irradiated at laser intensities in excess of 10^{20} w/cm². Phys. Plasmas, 16(6):062701–8, jun 2009.
- [86] B.L. Henke et al. X-ray interactions: photoabsorption, scattering, transmission, and reflection at $e=50-30000$ ev, $z=1-92$. Atomic Data and Nuclear Data Tables, 54:181, 1993.
- [87] H. R. Griem. Principles of Plasma Spectroscopy. Cambridge University Press, 1997.

- [88] C.J. Dasch. One-dimensional tomography - A comparison of Abel, onion-peeling, and filtered backprojection methods. *Apl. Optics*, 31:1146–1152, mar 1992.
- [89] J.J. MacFarlane et al. Helios-cr – a 1-d radiation-magnetohydrodynamics code with inline atomic kinetics modeling. *J. Quant. Spectrosc. Radiat. Transfer*, 99(1-3):381, 2006.
- [90] S. Bastiani, A. Rousse, et al. Experimental study of the interaction of subpicosecond laser pulses with solid targets of varying initial scale lengths. *Phys. Rev. E*, 56(6):7179–7185, 1997.
- [91] RA. Snavely, MH. Key, et al. Intense high-energy proton beams from petawatt-laser irradiation of solids. *Phys. Rev. Lett.*, 85(14):2945–2948, Oct 2000.
- [92] S. H. Glenzer et al. Observations of plasmons in warm dense matter. *Phys. Rev. Lett.*, 98:065002, 2007.
- [93] W. Theobald, K. Akli, et al. Hot surface ionic line emission and cold K-inner shell emission from petawatt-laser-irradiated Cu foil targets. *Phys. Plasmas*, 13(4):043102–+, apr 2006.
- [94] F.Y. Khattak, A-M McEvoy, et al. Effects of plastic coating on $k\alpha$ yield from ultra-short pulse laser irradiated ti foils. *J. Phys. D*, 36(19):2372–2376, 2003.
- [95] F. Ewald, H. Schwoerer, and R. Sauerbrey. K_α -radiation from relativistic laser-produced plasmas. *Europhys. Lett.*, 60:710–716, 2002.
- [96] R.G. Evans et al. Rapid heating of solid density material by a petawatt laser. *Appl. Phys. Lett.*, 86:191505, 2005.
- [97] C. Rischel, A. Rousse, I. Uschmann, et al. Femtosecond time-resolved x-ray diffraction from laser-heated organic films. *Nature*, 390:490–492, 1997.
- [98] O. L. Landen et al. Dense matter characterization by x-ray thomson scattering. *J. Quant. Spectrosc. Radiat. Transfer*, 71:465, 2001.
- [99] MK. Urry, G. Gregori, et al. X-ray probe development for collective scattering measurements in dense plasmas. *Journal of Quantitative Spectroscopy and Radiative Transfer*, 99:636–648, may 2006.
- [100] C. Bostedt et al. Experiments at flash. *Nucl. Inst. Meth. Phys. Res. A*, 601(1-2):108 – 122, 2009.
- [101] S.V. Milton et al. Exponential gain and saturation of a self-amplified spontaneous emission free-electron laser. *Science*, 292:2037–2041, 2001.
- [102] V. Ayvazyan et al. Generation of gw radiation pulses from a vuv free-electron laser operating in the femtosecond regime. *Phys. Rev. Lett.*, 88(10):104802, 2002.

- [103] W. Ackermann et al. Operation of a free-electron laser from the extreme ultraviolet to the water window. Nature Photonics, 1:336, 2007.
- [104] R. Mitzner et al. Direct autocorrelation of soft-x-ray free-electron-laser pulses by time-resolved two-photon double ionization of he. Phys. Rev. A, 80(2):025402, 2009.
- [105] U. Fruehling et al. Single-shot terahertz-field-driven x-ray streak camera. Nature Photonics, 3:523–528, sep 2009.
- [106] N.J. Carron. An Introduction to the Passage of Energetic Particles through Matter. Taylor and Francis Group, New York - London, 2007.
- [107] SM. Vinko, G. Gregori, et al. Free-free opacity in warm dense aluminum. High Energy Density Phys., 2009.
- [108] F. Ladstaedter et al. First-principles calculation of hot-electron scattering in metals. Phys. Rev. B, 70:235125, 2004.
- [109] C. Almladh, A. Morales, and G. Grossmann. Theory of auger core-valence-valence processes in simple metals. i. total yields and core-level widths. Phys. Rev. B, 39:3489–3502, 1989.
- [110] MP. Seah and WA. Dench. Quantitative electron spectroscopy of surfaces: A standard database for electron inelastic mean free paths in solids. Surface and Interface Analysis, 1:2–11, 1979.
- [111] JC. Ashley, CJ. Tung, and RH. Ritchie. Electron inelastic mean free paths and energy losses in solids: I. aluminum metal. Surface Science, 81:409–426, 1979.
- [112] N. Medvedev, private communication.
- [113] P. Beiersdorfer, G.V. Brown, et al. High-Resolution Crystal Spectrometer for the 10-60 Angstrom Extreme Ultraviolet Region. Review of Scientific Instruments, 75:3720–3722, oct 2004.
- [114] J. Jasny et al. A single-shot spectrograph for the soft x-ray region. Rev. Sci. Instrum., 65(5):1631–1635, 1994.
- [115] V. Kaufman and W.C. Martin. Wavelengths and energy level classifications for the spectra of aluminum. J. Phys. Chem. Ref. Data, 20(5):775–858, 1991.
- [116] S. Toleikis, R. R. Fäustlin, L. Cao, T. Döppner, S. Düsterer, E. Förster, C. Fortmann, S.H. Glenzer, S. Göde, G. Gregori, R. Irsig, T. Laarmann, H.J. Lee, B. Li, K.-H. Meiwes-Broer, A. Przystawik, P. Radcliffe, R. Redmer, F. Tavella, R. Thiele, J. Tiggesbäumker, N.X. Truong, I. Uschmann, U. Zastra, and Th. Tschentscher. Soft x-ray scattering using fel radiation for probing near-solid density plasmas at few electron volt temperatures. High Energy Density Phys., 2009.

- [117] A. R. B. de Castro and R. Reininger. Optimization of undulators for a sx-700 instrument: Finite element coupled to ray tracing. Rev. Sci. Instrum., 63 (1):1317–1320, 1992.
- [118] C.U.S. Larsson, A. Beutler, O. Björneholm, F. Federmann, U. Hahn, A. Rieck, S. Verbin, and T. Möller. First results from the high resolution xuv undulator beamline bw3 at hasylab. Nucl. Instrum. Methods, A337:603–608, 1994.
- [119] R. Reininger and V. Saile. A soft x-ray grating monochromator for undulator radiation. Nucl. Instrum. Methods, A288:343–348, 1989.
- [120] H. W. Schnopper, L. P. Van Speybroeck, J. P. Delvaille, A. Epstein, E. Källne, R. Z. Bachrach, J. Dijkstra, and L. Lantward. Diffraction grating transmission efficiencies for xuv and soft x rays. Appl. Opt., 16(4):1088–1091, 1977.
- [121] T. Kita, T. Harada, N. Nakano, and H. Kuoda. Mechanically ruled aberration-corrected concave gratings for a flat-field grazing-incidence spectrograph. Appl. Opt., 22:512–513, 1983.
- [122] N. Nakano, H. Kuroda, T. Kita, and T. Harada. Development of a flat-field grazing-incidence xuv spectrometer and its application in picosecond xuv spectroscopy. Appl. Opt., 23:2386–2392, 1984.
- [123] K. Oguri et al. Transient observation of extended x-ray absorption fine structure in laser-melted si by using femtosecond laser-produced-plasma soft x ray. Appl. Phys. Lett., 87:011563, 2005.
- [124] J. A. Bearden. x-ray transitions. Rev. Mod. Phys., 39(1):78–124, 1967.
- [125] H. A. Kramers. On the theory of x-ray absorption and the continuous x-ray spectrum. Philos. Mag., 46:836, 1923.
- [126] J. A. Gaunt. Continuous absorption. Proc. R. Soc. A, 126:654, 1930.
- [127] C. Fortmann et al. Bremsstrahlung vs. thomson scattering in vuv-fel plasma experiments. High Energy Density Physics, 2:57, 2006.
- [128] S. Kuhlbrodt et al. Comptra04: a program package to calculate composition and transport coefficient in dense plasmas. Contrib. Plasma Phys., 45:73, 2005.
- [129] W. Lochte-Holtgreven. Plasma diagnostics. In Plasma Diagnostics, page 135. AIP Press, New York, 1995.
- [130] U. Teubner et al. Soft x-ray spectra produced by subpicosecond laser-pulses. Appl. Phys. Lett., 59:2672, 1991.
- [131] R. LaVilla et al. Optical constants of aluminum in vacuum ultraviolet. Phys. Rev. Lett., 9(4):149–150, 1962.

- [132] M. M. Murnane et al. Ultrafast x-ray pulses from laser-produced plasmas. Science, 251(4993):531–536, 1991.
- [133] A. Krenz et al. Vuv-heating of plasma layers and their use as ultrafast switches. Eur. Phys. J. D, 36:199–202, 2005.
- [134] K. Tiedtke, J. Feldhaus, et al. Gas detectors for x-ray lasers. Journal of Applied Physics, 103:094511, 2008.
- [135] GN. Lewis, D. Lipkin, and TT. Magel. Reversible photochemical processes in rigid media. a study of the phosphorescent state. J. Am. Chem. Soc., 63:3005–3018, 1941.
- [136] J. Chalupský, L. Juha, et al. Characteristics of focused soft x-ray free-electron laser beam determined by ablation of organic molecular solids. Opt. Express, 15:6036–6043, 2007.
- [137] G. Dufour, J. Mariot, et al. K-LL Auger spectrum of aluminium. Physica Scripta, 13:370–372, 1976.
- [138] PH. Hannah and P. Weightman. The spectrum of Al $KL_{2,3}-L_{2,3}^2V$ satellite auger transitions. J. Phys. C: Solid State Phys., 18:L239–L243, 1985.
- [139] D. Kim and I. Kim. Calculation of ionization balance and electrical conductivity in nonideal aluminum plasma. Phys. Rev. E, 68:056410, 2003.
- [140] B. Siwick et al. An atomic-level view of melting using femtosecond electron diffraction. Science, 302:1382–1385, 2003.

Ehrenwörtliche Erklärung

Ich erkläre hiermit ehrenwörtlich, dass ich die vorliegende Arbeit selbstständig ohne Hilfe Dritter und ohne Benutzung anderer als der angegebenen Hilfsmittel und Literatur angefertigt habe. Die aus anderen Quellen direkt oder indirekt übernommenen Daten und Konzepte sind unter Angabe der Quelle gekennzeichnet.

Weitere Personen waren nicht an der inhaltlich-materiellen Erstellung der vorliegenden Arbeit beteiligt. Insbesondere habe ich hierfür nicht die entgeltliche Hilfe von Vermittlungs- bzw. Beratungsdiensten (Promotionsberater oder andere Personen) in Anspruch genommen. Niemand hat von mir unmittelbar oder mittelbar geldwerte Leistungen für die Arbeiten erhalten, die im Zusammenhang mit dem Inhalt der vorgelegten Dissertation stehen.

Die Arbeit wurde bisher weder im In- noch im Ausland in gleicher oder ähnlicher Form einer anderen Prüfungsbehörde vorgelegt.

Die geltende Prüfungsordnung der Physikalisch-Astronomischen Fakultät ist mir bekannt.

Ich versichere ehrenwörtlich, dass ich nach bestem Wissen die reine Wahrheit gesagt und nichts verschwiegen habe.

Jena, den 2. Dezember 2009

.....
Ulf Zastrau

Acknowledgments

I would like to thank all the people who helped making this work possible.

First of all, I thank Prof. Eckhart Förster for the interesting topics. By allowing me to participate in state-of-the-art experiments in world-wide collaborations, I was able to get outstanding results in a reasonable short time. Further, I thank Dr. Ingo Uschmann for the support, positive atmosphere and continuous advice.

Most of the data presented here were taken in few-week experimental campaigns in Palaiseau (France) and Hamburg (Germany). This includes night-shifts, week-end work and a lot of traveling from a large group of scientists, bringing equipment from their labs to one place and make it work together. Without their efforts, our experiments would have never succeeded. Also, this work would not have been possible without extensive discussions with a number of international physicists.

The people of the X-ray Optics Group, especially the other PhD students in my office, provided a good atmosphere. Thanks is also due to the laser crew in Palaiseau and the FLASH operators in Hamburg. I should thank Dr. Klaus Sokolowski-Tinten, who infected me with the 'virus' FLASH in 2005, when I did an experiment with him even before my diploma work started.

Finally, the work of DESY PhD student Roland Fäustlin, Jena design engineer Hartmut Lärz and the Jena workshop M1, lead by Bernhard Klumbies, was very important. They made the HiTRaX spectrometer come real. Dr. Ortrud Wehrhan and Heike Marschner fabricated and tested the crystal spectrometer, and thanks to them for the paramount quality.

For proof-reading the thesis and constructive discussion I would like to thank Malte Kaluza, Olli Kley, Christian Vitense, and Viola Weiss.

Last, I would like to thank my family and friends. Their belief in my skills supported me strongly. Also, they allow me to exclude physical problems from my brain at least for a few hours, which I think is one, if not the most important reason, that I still feel very happy with my profession as a physicist.

Curriculum vitae

PERSONAL DATA

name: Ulf Zastra

citizenship: german

date of birth: september 17th, 1980

place of birth: Essen (Germany)



POSITION

- | | |
|-------------------|---|
| 01/2007 - current | Scientific Assistant,
<i>German Israeli Foundation (GIF) and Bundesministerium für Bildung und Forschung (BMBF)</i>
via Department of Physics, University Jena, Germany. |
| 01/2007 - 12/2007 | Member of the German Helmholtz Association " <i>Virtual Institute 104: Plasma Physics Research Using Free Electron Lasers</i> " via Department of Physics, University Jena, Germany. |
| 01/2006 - current | Member of the Peak-Brightness Collaboration at FLASH (Hamburg) |

SCIENTIFIC EDUCATION

- | | |
|-----------|---|
| 2007-2009 | Ph.D.,
X-ray Optics Group, IOQ, FSU Jena |
| 2003-2006 | Physics Diploma,
X-ray Optics Group, IOQ, FSU Jena (<i>very good</i>)
Title: <i>The laser-induced semiconductor-metal phase transition in samarium sulphide</i>
Supervisor: <i>Prof. Dr. E. Förster</i> |

2001-2003	Physics Prediploma, Friedrich-Schiller University Jena (<i>good</i>)
2000	Abiturium, städt. Gymnasium Herten, Germany (<i>very good</i>)

STAYS ABROAD

1/2008	one month at LULI in Palaiseau, France.
2006-2009	several visits to ESRF, Grenoble, France.
7/2009	two weeks at UCLA, LCLS and LBNL in California, USA.

TEACHING EXPERIENCE

2005-current	Advisor for lab works for undergraduate students.
--------------	---

AWARDS

6/2009	HEPTAGON Sven Bühling Forschungs- förderungs-Preis <i>The award was granted due to outstanding results in pho- ton science during the Ph.D.</i>
--------	---

LANGUAGES

german	very good (<i>mother tongue</i>)
english	very good
french	fairly good